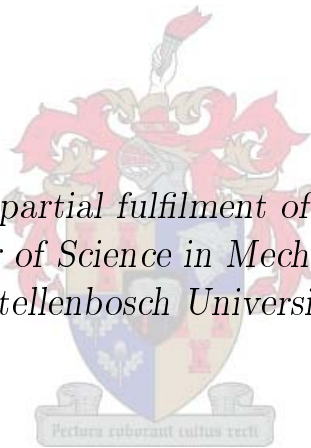


# High Accuracy Numerical Model of the SALT Mirror Support Truss

by

Billy de Lange

*Thesis presented in partial fulfilment of the requirements for  
the degree of Master of Science in Mechanical Engineering at  
Stellenbosch University*



Department of Mechanical and Mechatronical Engineering,  
University of Stellenbosch,  
Private Bag X1, Matieland 7602, South Africa

Supervisor: Prof. G. Venter

December 2011

# Declaration

By submitting this thesis electronically, I declare that the entirety of the work contained therein is my own, original work, that I am the owner of the copyright thereof (unless to the extent explicitly otherwise stated) and that I have not previously in its entirety or in part submitted it for obtaining any qualification.

Signature: .....  
B. De Lange

Date: ..... 15 November 2011

Copyright © 2011 Stellenbosch University  
All rights reserved.

# Abstract

## High Accuracy Numerical Model of the SALT Mirror Support Truss

B. De Lange

*Department of Mechanical and Mechatronics Engineering,  
University of Stellenbosch,  
Private Bag X1, Matieland 7602, South Africa*

Thesis: MScEng (Mech)

December 2011

Although a numerical model of the mirror support truss of the Southern African Large Telescope (SALT) has already been developed during the design thereof, this thesis focuses on the development of the methods and techniques that would result in a more accurate numerical model of the actual structure that could be used as a basis for a numerical control system. This control system will compensate for deflections in the structure by adjusting the positioning of the individual mirror segments of the primary mirror.

The two main components from which the support truss is constructed are the steel nodes, and the struts that connect to them. For this project a smaller, simpler laboratory model was designed and built to have geometrical properties similar to that of the support truss. The methods and techniques that were investigated were carried out on this model.

By using numerical design optimisation techniques, improved numerical models of the different strut types were obtained. This was done by performing tests on the struts so that the actual responses of the struts could be obtained. Numerical models of the struts were then created and set up so that they could be optimised using structural optimisation software. Once accurate strut models had been obtained, these strut models were used to construct a numerical model of the assembled structure. No additional optimisation was performed on the assembled structure and tests were done on the physical structure to obtain its responses. These served as validation criteria for the numerical models of the struts.

Because of unforeseen deformations of the structure, not all of the measured structural responses could be used. The remaining results showed, however,

that the predictive accuracy of the top node displacement of the assembled structure improved to below 1.5%, from over 60%. From these results it was concluded that the accuracy of the entire structure's numerical model could be significantly improved by optimising the individual strut types.

# Uittreksel

## Numeriese Modelling van die SALT Spieëlondersteuningsraamwerk met Hoë Akkuraatheid

*(“High Accuracy Numerical Model of the SALT Mirror Support Truss”)*

B. De Lange

*Departement Meganiese en Megatroniese Ingenieurswese,  
Universiteit van Stellenbosch,  
Privaatsak X1, Matieland 7602, Suid Afrika*

Tesis: MScIng (Meg)

Desember 2011

Alhoewel daar reeds ’n numeriese model van die spieëlondersteuningsraamwerk van SALT ontwikkel is gedurende die ontwerp daarvan, fokus hierdie tesis op die ontwikkeling van metodes en tegnieke om ’n numeriese model van steeds hoër gehalte van hierdie spesifieke struktuur te verkry wat kan gebruik word as ’n basis vir ’n numeriese beheerstelsel. Hierdie beheerstelsel sal kan kompenseer vir die ondersteuningsraamwerk se vervormings deur om die individuele spieëlsegmente van die primêre spieël se posisionering te verstel.

Hierdie stuktuur bestaan uit hoofsaaklik twee komponente, naamlik staalnodusse en die stutte wat aan hulle koppel. Vir hierdie projek is ’n kleiner, eenvoudiger laboratorium-model ontwerp en gebou om geometriese eienskappe soortgelyk aan die van die ondersteuningstruktuur te hê. Die metodes en tegnieke wat ondersoek is, is op hierdie model uitgevoer.

Verbeterde numeriese modelle van die verskillende stut-tipes is ontwikkel deur middel van numerieseoptimeringstegnieke. Dit is gedoen deur toetse op die stutte uit te voer sodat hul werklike gedrag bepaal kon word. Numeriese modelle van die stutte is toe geskep en opgestel sodat hulle geoptimeer kon word om dieselfde gedrag as wat gemeet is, te toon. Hierdie geoptimeerde modelle is toe gebruik om numeriese modelle van die toets-struktuur te skep. Geen verdere optimering is op die numeriese model uitgevoer nie en toetse is op die struktuur gedoen om sy werklike gedrag te meet. Data wat deur die toetse verkry is het as validasie kriteria gedien om die akkuraatheid van die numeriese modelle van die stut-tipes te bepaal.

Weens die struktuur se onvoorsiene vervorming kon alle gemete struktuur-data nie gebruik word nie. Die oorblywende data het egter getoon dat die akkuraatheid van die finale numeriese modelle van die struktuur verbeter het en dat dit die translasië van die top-node met 'n speling van 1.5% akkuraatheid kon voorspel, teenoor die oorspronlike speling van meer as 60%. Daar is bevind dat die akkuraatheid van die numeriese model van die hele struktuur noemenswaardig verbeter kan word deur die numeriese modelle van die stut-tipes te optimeer.

# Acknowledgements

First and foremost I wish to thank the SALT Foundation for allowing me to work on a project that is related to such a highly regarded engineering marvel, as well as for providing me with the financial support to do so.

Thank you to Prof. Gerhard Venter, for his seemingly endless patience and well-considered guidance, whilst still allowing me to make this thesis my own.

My most sincere gratitude goes to my parents and my girlfriend, without whose tremendous support and motivation I would not have had the capacity to complete this thesis.

Thank you to the staff of the Department of Mechanical and Mechatronical Engineering, for providing a clean, maintained, well-administrated and friendly working environment.

# Contents

<b>Declaration</b>	<b>i</b>
<b>Abstract</b>	<b>ii</b>
<b>Uittreksel</b>	<b>iv</b>
<b>Acknowledgements</b>	<b>vi</b>
<b>Contents</b>	<b>vii</b>
<b>List of Figures</b>	<b>ix</b>
<b>List of Tables</b>	<b>xi</b>
<b>1 Introduction</b>	<b>1</b>
1.1 Background to SALT . . . . .	1
1.2 Motivation . . . . .	2
1.3 Objectives . . . . .	3
<b>2 Literature Survey</b>	<b>5</b>
2.1 Finite Element Model Updating . . . . .	5
2.2 Numerical Design Optimisation . . . . .	10
<b>3 Materials and Methods</b>	<b>14</b>
3.1 Laboratory Model Design . . . . .	14
3.2 Methodology . . . . .	18
<b>4 Individual Strut Testing</b>	<b>22</b>
4.1 Selection of Load Cases . . . . .	22
4.2 Axial Load Case Tests . . . . .	24
4.3 Bending Load Case Tests . . . . .	33
4.4 Dynamic Load Case Tests . . . . .	37
<b>5 Numerical Modelling of Individual Struts</b>	<b>40</b>
5.1 General Modelling Details . . . . .	40
5.2 Coarse Updating . . . . .	42



5.3	Automatic Updating . . . . .	46
5.4	Data-matching Results for the Remaining Strut Types . . . . .	58
<b>6</b>	<b>Testing and Modelling of the Assembled Structure</b>	<b>61</b>
6.1	Structure Testing . . . . .	61
6.2	Structure Modelling . . . . .	68
6.3	Comparison of Results . . . . .	69
6.4	Validation Conclusion . . . . .	75
<b>7</b>	<b>Conclusion</b>	<b>77</b>
7.1	Overview . . . . .	77
7.2	Future Work . . . . .	79
	<b>Appendices</b>	<b>80</b>
<b>A</b>	<b>Modelling Data of Individual Struts</b>	<b>81</b>
A.1	Response Data of the A-Strut . . . . .	81
A.2	Responses of All Final Strut Models . . . . .	83
<b>B</b>	<b>Test Data of Final Structure</b>	<b>85</b>
B.1	Data of Four-node Structure . . . . .	85
B.2	Data of Five-node Structure . . . . .	90
<b>C</b>	<b>Rigid Body Mode Compensation Formulation</b>	<b>96</b>
C.1	Global Coordinate System Translations . . . . .	96
C.2	Local Coordinate System Translations . . . . .	98
	<b>List of References</b>	<b>100</b>

# List of Figures

1.1	Cross-sectional illustration of SALT . . . . .	3
2.1	Parameter subspace schematics . . . . .	7
	(a) Poor parameter selection . . . . .	7
	(b) Poor objective definition . . . . .	7
	(c) Correct parameter and objective function definitions . . . . .	7
2.2	Example of Pareto curve . . . . .	9
2.3	Two-variable design optimisation representation . . . . .	11
2.4	Domain method for shape change . . . . .	12
3.1	The primary mirror support truss . . . . .	15
3.2	CAD representation of laboratory model . . . . .	15
3.3	SALT mirror support truss: Close-up of struts and nodes . . . . .	16
3.4	Strut assembly . . . . .	17
3.5	Example of one of the solid steel nodes of the laboratory model . . . . .	18
3.6	Structure component labels . . . . .	19
3.7	Flowchart of proposed methodology . . . . .	21
4.1	Boundary conditions for selected load cases . . . . .	24
4.2	Axial test load frame . . . . .	25
4.3	Bottom components of first axial test setup . . . . .	26
4.4	Typical results of first axial test setup . . . . .	27
4.5	Typical results of second axial test setup . . . . .	28
4.6	Difference in datum between setups . . . . .	29
4.7	Final axial test setup . . . . .	31
	(a) Complete setup . . . . .	31
	(b) Top components . . . . .	31
4.8	Typical results of the final axial test setup . . . . .	32
4.9	Final results for the central bar compliances . . . . .	34
4.10	Bending load case setup . . . . .	35
4.11	Result of bending over rods test . . . . .	36
4.12	Normalised bending results . . . . .	38
4.13	Test setup for obtaining the frequency response functions . . . . .	39
5.1	Boundary condition application points . . . . .	41

5.2	First strut model effective cross-sections . . . . .	42
5.3	Effective cross-sections of the second strut model . . . . .	44
5.4	Effective cross-sections of the third strut model . . . . .	45
5.5	Effective contact area of the M12 nut . . . . .	45
5.6	Shape change domains and perturbations . . . . .	50
5.7	Adding parallel elements to the end caps . . . . .	52
5.8	Change in hollow bar properties . . . . .	54
5.9	Errors for different strut models . . . . .	56
5.10	Design variable changes for different strut models . . . . .	57
5.11	Objective errors for all final strut models . . . . .	60
6.1	Final test setup of the assembled structure . . . . .	62
6.2	Failed physical boundary conditions . . . . .	63
	(a) Fixed boundary condition . . . . .	63
	(b) Simply supported boundary condition with carriages . . . . .	63
6.3	Final supporting boundary condition setup . . . . .	64
	(a) Close-up photo . . . . .	64
	(b) Bottom view schematic . . . . .	64
6.4	Detail of loading boundary condition . . . . .	66
	(a) Loading setup . . . . .	66
	(b) Rounded tip of low-profile jack . . . . .	66
6.5	Method of calibrating the LVDT on a foot node . . . . .	67
6.6	Modelling of the complete structure . . . . .	69
	(a) Simplified FE model of structure . . . . .	69
	(b) Modelling detail of foot nodes . . . . .	69
6.7	FE models of deformed five-node structure . . . . .	72
	(a) Current model . . . . .	72
	(b) Representation of rotation on foot nodes . . . . .	72
6.8	FE representation of unsymmetrical deformation . . . . .	73
6.9	Rigid body mode compensation schematic . . . . .	74
C.1	Geometry for calculation of rotational effects . . . . .	97
C.2	Geometry for transformation to direction of measurement of the LVDT . . . . .	99

# List of Tables

4.1	Results of third axial test setup . . . . .	29
4.2	Final compliances for different struts . . . . .	35
4.3	Numerical bending normalisation factors . . . . .	37
4.4	Measured displacements for bending load cases . . . . .	37
4.5	Measured natural frequencies . . . . .	39
5.1	Summary of the results of the first strut model . . . . .	43
5.2	Summary of the results of the second strut model . . . . .	44
5.3	Summary of the results of the third strut model . . . . .	46
5.4	Summary of the results of the fourth strut model . . . . .	49
5.5	Summary of the results of the fifth strut model . . . . .	50
5.6	Summary of the results of the sixth strut model . . . . .	52
5.7	Summary of the results of the seventh strut model . . . . .	53
6.1	Modelling and testing results and errors . . . . .	70
6.2	Rigid body movement parameters . . . . .	75
A.1	Summary of the responses of the various models of the A-strut . . .	82
A.2	Summary of the all the responses from all the strut types . . . . .	84

# Chapter 1

## Introduction

It is claimed that the study of celestial objects, astronomy, is one of the oldest natural sciences. Artifacts left behind by prehistoric cultures as old as the Maya and Babylonians suggest that methodical observations of the night sky were recorded (Forbes, 2008). However, it was only with the development of the optical telescope that these observations could constitute the beginnings of what was to become a modern science. This science is applied to provide clarity on issues such as evolution and the development of the universe, and has provided insights for other fields, such as physics and even chemistry. Astronomy has since developed into two branches, namely observational and theoretical astronomy. While theoretical astronomy focuses on the development of models that predict the behaviour of astronomical objects, observational astronomy focuses on acquiring data about these objects. The development of the technology to acquire the data is being pushed constantly as more accurate information on more distant objects is required. This driving force, amongst others, is what led to the development of the Southern African Large Telescope, or as it is commonly known, SALT.

### 1.1 Background to SALT

SALT is the largest reflecting telescope in the southern hemisphere and is the result of collaboration between partners from seven countries. Construction of this single optical telescope commenced in January 2000 and was completed in late 2005. It is situated near the Karoo town of Sutherland, which is notorious for its cold winters, often getting snow. This remote, seismologically stable location is well suited due to its limited air and light pollution, since both airborne particles and other light sources have a negative effect on the quality of the observations performed using an optical telescope.

The design of SALT is based on that of the Hobby-Eberly Telescope (HET) in Texas, but its optical system was redesigned to make better use of the mirror array that forms its primary mirror. SALT's primary mirror consists of

91 hexagonal mirrors and is 11 metres across. The individual mirror segments are supported by what is known as the mirror support truss, a spatial structure consisting of 1 747 struts connected to 383 nodes.

During operation, incoming light is reflected off the primary mirror and into the optical payload, as shown in Figure 1.1. Instead of rotating the entire telescope — including the optical payload and the primary mirror — in both elevation and azimuth, the primary mirror remains at a fixed elevation angle and can only rotate around its azimuth. To obtain a wider field of view, the optical payload is moved by the tracker system to focus on different points on the primary mirror. It is this design feature that makes SALT a low-cost telescope relative to its large size (Buckley *et al.*, 2005).

Because of the fixed elevation angle, the primary mirror must have a spherical shape as opposed to a hyperbolic shape. The mirror support truss provides this shape. Each mirror segment is fixed to the support truss structure using a system that allows for automatic tip, tilt and piston movements of each individual mirror. These movements are necessary for the calibration of the primary mirror, which is done automatically if the calibration command is given. If calibration is necessary, the mirror is rotated to face a device called the centre of curvature sensor, which is mounted in the tower outside the dome, as seen in Figure 1.1. The centre of curvature sensor provides the calibration control system with the necessary information to correctly orientate each mirror segment so that the shape, and therefore the focus, of the whole mirror is corrected. This calibration process can take up to 45 minutes and should ideally only have to happen once per night.

## 1.2 Motivation

Although the SALT project has been successful in almost all regards, there are still some underlying engineering problems that need attention in order to improve the performance of the system. One of these problems is that observers find that their images become out of focus during observation sessions. Although the mirror can be calibrated, this process takes a large portion of the usable viewing time available during a night and therefore becomes a frustrating hindrance. An investigation into the cause of this problem found that the mirror support truss was not behaving as it was designed. Capacitive gap-size sensors already installed between the mirror segments indicated that the support truss is exhibiting unsymmetrical deflection. This results in the primary mirror losing its spherical shape, and the images therefore become distorted. A current solution to this problem is to make use of the tip, tilt and piston capabilities of the mirror segments by implementing a control system to automatically compensate for the distortion. This control system will provide for the corrections based on a computer model that accurately reflects the be-

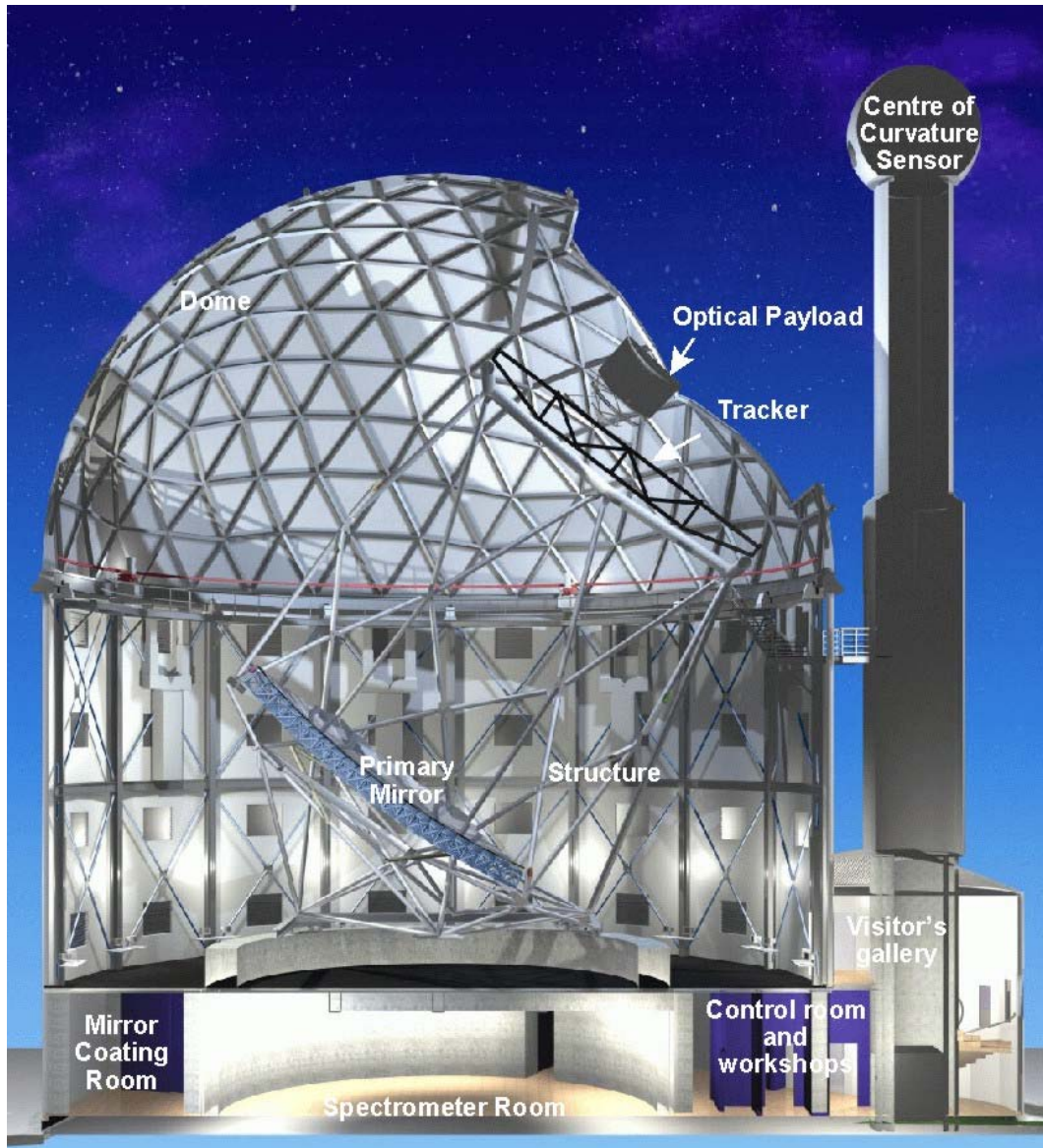


Figure 1.1: Cross-sectional illustration of SALT (Rutgers, 2011)

haviour of the support truss. It is this necessity to obtain such an accurate model of this specific structure that forms the motivation for this project.

### 1.3 Objectives

During the original development of the support truss structure, a finite element (FE) model was created on which the design criteria were tested. This model was to serve as a starting point for the current project, but because of the complexity of the actual support truss, it was decided to first study the

techniques and methods required to improve an FE model of such a structure by going through the process on a smaller, simpler laboratory model.

With due consideration of these aspects, the following project objectives were set:

1. Design and build a simpler physical model suited for laboratory testing. The construction of the structure should reflect that of the mirror support truss in terms of:
  - materials used,
  - geometry of the structure and
  - method of assembling the structure.
2. Obtain measurable responses of the laboratory model that can be used as validation criteria or numerical model objectives, or both.
3. Use the measured responses to investigate the accuracy of the modelling techniques used in the existing FE model.
4. Investigate additional linear modelling techniques with the aim of improving the existing model.
5. Investigate the implementation of numerical design optimisation to further improve the modelling techniques and parameters by using measured responses as objectives for numerical model responses.
6. Validate the new models and techniques using measured data.
7. Provide suggestions for improving the accuracy of the numerical models for the structure based on the findings of this study.



# Chapter 2

## Literature Survey

The process of refining a numerical model to match the measured responses of an existing structure is known as model updating. When using an FE model, the process is referred to as FE model updating (FEMU). Throughout the literature it is apparent that this is a difficult task, which has consequently led to the development of many techniques and methods (Kanev *et al.*, 2007). The process of updating a numerical model and the corresponding numerical design optimisation techniques that will be used are reviewed in this section.

### 2.1 Finite Element Model Updating

Structural analysis usually only requires the response of a transformation given a set of parameters. Let  $\mathcal{S}$  be the source space of all possible parameters that can describe a system. If  $\Omega$  is a subspace of parameters that describes a variant of the system and  $\Upsilon$  is the residual of the source space, i.e.  $\Omega + \Upsilon = \mathcal{S}$ , then

$$\mathcal{F}(\Omega, \Upsilon) = \mathbf{R}$$

where  $\mathbf{R}$  is the response space after some transformation  $\mathcal{F}$ . This is known as a direct problem since one space is transformed into another (Shan *et al.*, 1994). A typical example of this is one of the matrix equations used in FE methods where the stiffness matrix  $\mathbf{K}$  transforms the displacement vector  $\mathbf{u}$  to obtain the load vector  $\mathbf{P}$ , such as in the equation below:

$$\mathbf{K}\mathbf{u} = \mathbf{P}$$

Here the parameters of  $\mathbf{u}$  describe a single state of the system in the displacement space. By transforming these parameters using the forward operator  $\mathbf{K}$ , which is known explicitly, the unknown parameters in the load space  $\mathbf{P}$  are obtained.

In an inverse problem, the parameters in the response space  $\mathbf{R}$  are known and the subspace  $\Omega$  is sought that will yield this  $\mathbf{R}$  after a transformation  $\mathcal{F}$ .

For many model updating problems, this problem is ill-posed, which means that solving an inverse problem can give rise to multiple complications. These complications are categorised by Ziaei-Rad and Imregun (1996) to have the following possible outcomes:

- (a) *Non-convergence*: The response space does not belong to the range of the transformation. The problem has no solution.
- (b) *Non-uniqueness*: The transformation is not injective and thus the inverse does not exist. The problem will have multiple solutions.
- (c) *Instability*: The inverse of the transformation is not continuous in the response space. The solution is dependent on the condition of the transformation.
- (d) *Existence*: The transformation's inverse exists and is continuous in the response space. The solution is unique.

To relate this to model updating, even if a proper updating technique (*transformation*) is implemented, the proper parameter selection (*source subspace*) (Mottershead *et al.*, 2000) and proper objective definition (*response*) are critical for a successful outcome. Their importance is highlighted by Kim and Park (2004), using the following explanation:

- Let  $\mathbf{S}$  again be the source space for parameters and therefore in this space all the possible FE models of the system exist.
- $\mathbf{\Omega}$  is again the chosen subset of parameters and therefore this subspace describes all the FE models that can be derived by the chosen parameters.
- Finally, let  $\phi$  be the subspace of parameters that describe all the FE models that correlate well with the experimental results.

In Figure 2.1 the possible problems of poor parameter selection and poor objective definition are shown schematically. Figure 2.1a shows the case where the poor parameter selection results in the selected parameter( $\mathbf{\Omega}$ ) subspace and the experimental correlating parameter( $\phi$ ) subspace not intersecting. Thus a transformation between spaces cannot be achieved, representing the case of *non-convergence*. Figure 2.1b shows the case where, although the two parameter subspaces intersect, the objective is poorly defined and the final FE model ( $\mathbf{FEM}_{fin}$ ) is still not the optimal solution ( $\mathbf{FEM}_{opt}$ ), which could lead to a case of *non-uniqueness*.

In addition to having the correct parameter selection and objective definition, this case is shown in figure 2.1c, there is also a third factor that will determine the success of an inverse problem solution, and that is to use a suitable updating technique. This will be discussed first.

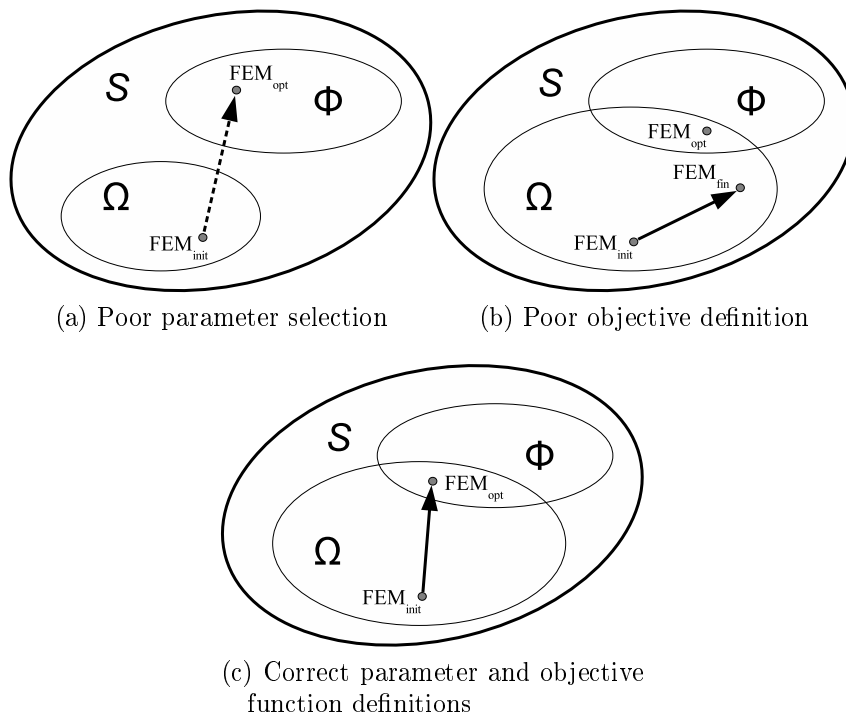


Figure 2.1: Parameter subspace schematics

### 2.1.1 Model updating techniques

There are two categories for model updating using finite element methods (Lung and Pak, 2008). The first, known as *direct methods*, is to make adjustments directly to the mass and stiffness matrices, instead of to the parameters of which they are a function. These adjustments are done in numerous ways, examples of which can be found in Lee and Eun's article on this topic (Chen and Wang, 1991), which also very conveniently tabulates a number of these methods. These methods provide for accurate models and are useful to compensate for modelling inaccuracies (Kozak *et al.*, 2009). However, in many cases the physical significance of the model and its parameters is lost (Kim and Park, 2004), and some methods result in matrices that are not positive-definite (Kanev *et al.*, 2007).

The second category, *parametric methods*, adjusts only the parameters that describe the system. These parameters typically include the topological, shape, material and geometrical properties of the system. These methods will be used in this project because the physical meaning of the parameters is retained. This allows one to better understand which areas of the structure require which type of parameter changes, and thus these changes can be adapted or scaled to other areas if needed. It is also easier to see from the scale and type of parameter changes produced where the modelling methods fail to describe the actual

structure, and therefore better-suited changes can be sought for objectively.

### 2.1.2 Parameter selection and objective definition

Parameter selection is usually based on the sensitivity of the parameters to the objective function (Mottershead *et al.*, 2000). By choosing the most sensitive parameters, smaller changes are required to have greater effect on the objective function. Of these parameters, the material properties of the structure have great effects (Kim and Park, 2004) and would make suitable selections, but they are not always justifiable. Other parameter selection techniques focus on identifying modelling errors in the numerical model. In these methods the source of the modelling error must be identified, and then parameters are chosen that could be used to compensate for modelling uncertainties.

Modelling errors can consist of idealisation errors, discretisation errors or modelling assumptions that are not accurate (Mottershead *et al.*, 2010). It should also be borne in mind that the finite element methods are not exact and therefore a complete correlation will not always be possible. Since the objectives can include the matching of measured displacements, strains, mass properties and frequency and modal data (Lung and Pak, 2008), these approximation errors must be considered when defining the data-matching convergence criteria (Mottershead *et al.*, 2010).

In data matching, the objective is to minimise the error between the numerical model output and the measured data target. When there are more than one of these objectives, say multiple displacements and frequencies to be matched, the problem is known as a multi-objective optimisation (MOO) problem. Because all the objectives need to be addressed simultaneously, different techniques and methods have been developed to combine these into a single objective function for optimisation. Marler and Arora (2004) discuss many of these methods, but only two of the methods will be considered here to illustrate how the choice of objective definition could influence the optimisation outcome.

If the objective is to minimise the error between the current response and the target response for multiple responses, minimising the maximum of the individual error values would be one method to consider. An effective way to do this is to add an extra variable to the set of design variables. The objective is then to minimise this variable, while a constraint that none of the error values may be larger than this variable is imposed. This is known as the  $\beta$ -method.

Another method is to minimise the sum of the squares of the errors. Although the  $\beta$ -method will produce a lower maximum error (Vanderplaats, 2007), the sum of the squares method could produce a lower mean error. Therefore a suitable method must be chosen based on the specific requirements of a given problem's outcome.

Even if the correct objective function definitions are used, this does not always mean that there is only a single optimum solution. For a point to be the optimum of an MOO problem, this point — known as the utopia point — would have to be the optimum of each of the individual objectives without exception. Such a point is not always obtainable, however, because many, if not most, MOO problems will have at least more than two objective functions that oppose each other. This means that an improvement in one objective results in another objective becoming worse. Therefore, MOO problems usually require some form of trade-off between objectives, depending on which of the objectives are of greater importance.

Figure 2.2 illustrates this case. Here the white dots are possible solutions, but are not optimal solutions. The black dots are all the possible optima for a problem with two objectives. These optimal points form what is known as a Pareto curve. Every point on the Pareto curve is a possible optimum solution, and from an optimisation point of view, all points on the curve are equally good. No single optimum point exists and it is the designer who needs to decide which objective is of more importance to a given problem and to what degree, and then to choose a suitable point.

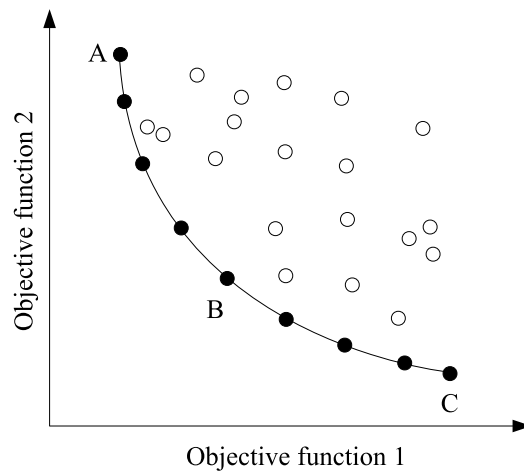


Figure 2.2: Example of Pareto curve

If information about this preferred point is available, *compromise programming* can be used to steer the optimisation process to converge to that point. This is typically the case where the designer wants the optimiser to change the design parameters in order to have the response match a certain target value. In *compromise programming*, each objective is formulated as an error between the current design response and the target response. Each respective error is then scaled by its worst value so that the errors are of a similar order of magnitude. This ensures that all objective errors have an equal contribu-

tion to the objective function. In addition to this, *compromise programming* allows for a weighting factor to be added to each objective. Such weighting factors give the designer the ability to scale the importance of each objective. Although this is very useful, it is not always possible to objectively quantify these weights, and this could lead to biased results.

## 2.2 Numerical Design Optimisation

To solve the data-matching problem of this project it was decided to use a parametric method so that the resulting modelling parameters can still be used for interpretation. Numerical design optimisation combines numerical modelling techniques with numerical optimisation techniques and provides for such a method, if applied correctly.

### 2.2.1 Fundamentals of numerical optimisation

The fundamental definition of a numerical optimisation problem is to minimise or maximise a certain objective function by changing defined system parameters (Vanderplaats, 2007), known as design variables. There are numerous methods to achieve this, depending on the problem at hand. Since parametric model updating will be used, gradient-based algorithms are a good option (Lung and Pak, 2008), and further optimisation principles will be discussed based on these methods.

It is convenient to visualise optimisation problems by using only two design variables and a continuous objective function, as shown in Figure 2.3. In this case, the objective is to find the minimum of the objective function by using gradient-based techniques.

In gradient-based techniques an iterative process is used in which the objective function's value and gradients are calculated at each iteration using the current values of the design variables. The gradient information, or sensitivities, are used to determine the new search direction and, together with a step size, the next iteration's design variable values are determined. Thus, as shown in Figure 2.3, steps are taken in a direction with a downwards slope, continuing until no further progress is made in terms of the convergence criteria.

### 2.2.2 Numerical optimisation and finite element methods

To apply numerical optimisation in the design of structures, FE methods are used to provide the information on the objective and constraint functions. The design variables are typically the parameters that control the physical properties of the structure, such as section dimensions and material properties.

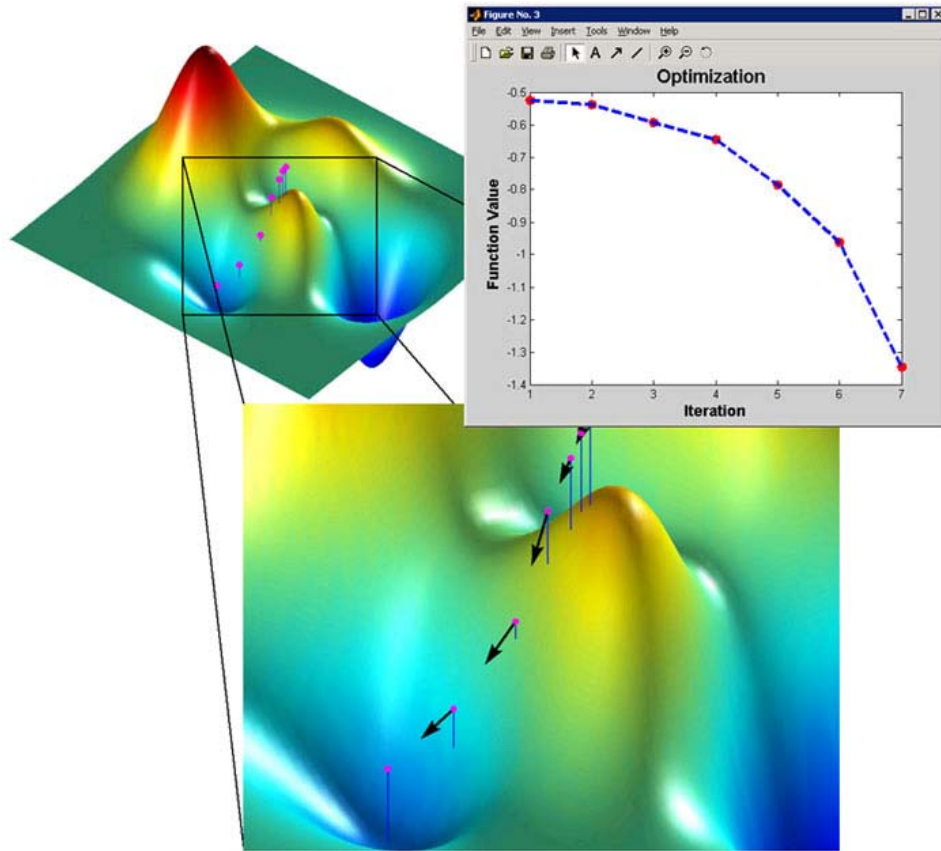


Figure 2.3: Two-variable design optimisation representation (MathWorks, 2011)

Constraints can be imposed on various parameters, including design variable limits and structural responses.

Because numerical optimisation is an iterative process requiring objective function evaluations and gradient calculations for each iteration, it can be computationally expensive if an FE analysis needs to be done for each iteration. Therefore techniques have been developed that can reduce the number of FE model evaluations required by making approximations based on the physics of the given problem. Because the physics can be described explicitly, the objective function can be approximated using first-order Taylor series expansion. These approximations can also be applied to the constraints.

Using these approximations, the objective functions and constraints are defined explicitly, allowing for more cost-effective function evaluations and gradient calculations to be made. Because the Taylor series expansion is precise for determinate structures, only one FE analysis is required for the entire optimisation process. For indeterminate structures the approximations are accurate enough that only a few FE evaluations are required (Vanderplaats,

2007).

Structural optimisation design variables are not limited to the parameters describing a structure's properties, as methods have been developed to make changes to a structure's geometry as well. Note that, although there are other structural optimisation techniques, namely topometry, topology and topography, only shape change design and sizing design methods will be discussed, since only these types are used in this project.

While sizing design allows changes to be made to the properties of an element, shape change design allows for changes to the positions of element nodes. Of the techniques available to make these changes, the domain method has the advantage of being computationally cheap and the user has complete control over where the grids will move (Leiva and Watson, 1999).

In using the domain method, one must specify regions containing the nodes that are to be moved, known as domains. Each domain is represented by a linear or quadratic FE element that does not form part of the structural analysis and can include many internal grids. Next, perturbation vectors are specified on the corners or mid-side nodes of these domain elements. Perturbation vectors describe which displacement changes can be made to these nodes. The perturbation vectors for the interior grids of the domain, those that do not have vectors already assigned to them, are created using the shape functions of the domain elements to interpolate between the specified perturbation vectors. This is illustrated in Figure 2.4 for a one-dimensional, linear domain element consisting of multiple structural elements.

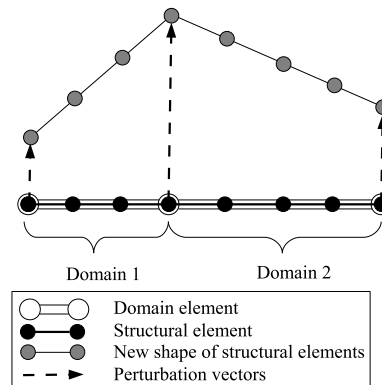


Figure 2.4: Domain method for shape change



From the literature it is apparent that, although solving an inverse problem such as model updating can be difficult in theory, there are many techniques, methods and guidelines that have been developed to aid the designer. With the help of numerical optimisation techniques, especially if combined with FE methods, the task can be attempted with more confidence if one is wary of the possible pitfalls.

# Chapter 3

## Materials and Methods

In the previous chapter, the general theory and applicable optimisation techniques were outlined. The different aspects of the project will be outlined in this chapter to provide a global overview of the project. The laboratory model used to obtain the experimental data is discussed first to provide the reasoning for the proposed methodology.

### 3.1 Laboratory Model Design

As stated by the project objective in Section 1.3, a small-scale laboratory model that represents a segment of the SALT support truss was designed and built. This laboratory model was designed to reflect the following important attributes of the support truss: geometry between nodes, strut construction and method of assembly.

#### 3.1.1 Geometry

The mirror support truss consists of simple building blocks that represent a tetrahedra shape. Each tetrahedra is connected to the neighbouring tetrahedra at their nodes, as shown in Figure 3.1.

In the mirror support truss there are many different strut lengths, and the shapes of the tetrahedra also vary. For the laboratory model it was decided to have all of the outside nodes at the same distance of 1 m apart. This is roughly the size of the middle layer of tetrahedra in the mirror support truss.

Furthermore, a central node was added to investigate further complexity. This was placed directly below the top node, at half the height of the top node as shown by the CAD model in Figure 3.2. This allowed for investigating either a four-node, six-strut structure or a five-node, ten-strut structure.

Both variants are possible without violating what is known as "Maxwell's rule", which states that a structure is considered a stiff structure, as opposed to a linkage, when the following equation is upheld:



Figure 3.1: The primary mirror support truss (Ratcliffe, 2011)

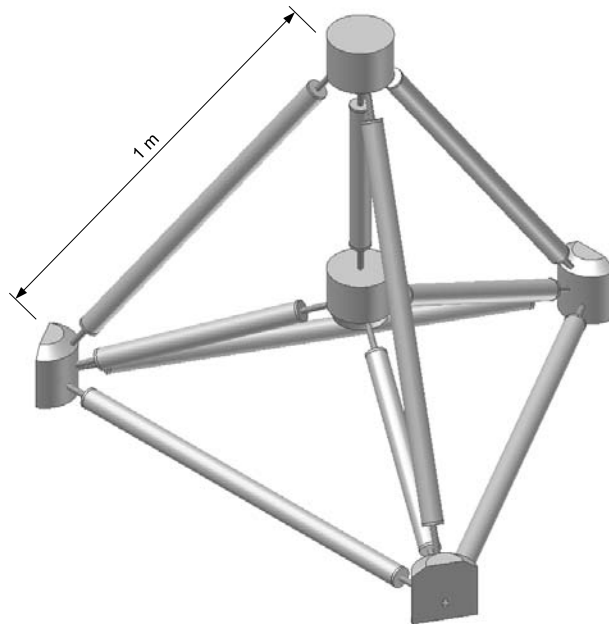


Figure 3.2: CAD representation of laboratory model

$$b \geq 3j - 6 \quad (3.1.1)$$

Here  $b$  is the number of struts and  $j$  is the number of nodes (Maxwell, 1864). Using this formula, the four-node case of the laboratory structure is statically determinate. For the five-node case, where there are more struts than required,

the structure is self-strained and therefore statically indeterminate. By first investigating the statically determinate structure, general problems and complications can be identified independently before the statically indeterminate structure, with its own possible complications, is investigated.

### 3.1.2 Components

The struts are designed so that the node-to-node length can be calibrated after installation, similar to the struts in the mirror truss. This is done by having threaded rods that have opposing thread directions screwed into the ends of the strut. These threaded rods, in turn, screw into the nodes. Therefore, when the central bar is twisted, the length between the nodes change. When the desired length is attained, nuts on the threaded rods are tightened against both the node and the central bar to fix the strut length. In Figure 3.3, examples of SALT's struts, with the central bar, threaded rod on the ends, locking nuts and nodes (bottom right), are shown.



Figure 3.3: SALT mirror support truss: Close-up of struts and nodes (SALT Foundation, 2011)

For the laboratory model the struts were built to be similar to those of SALT by inserting end caps into a hollow bar (Figure 3.4). The end caps have a flange to locate the depth of insertion, and this flange is also used to weld the end caps to the hollow bar. The end caps are machined to have a tight fit

and are press fitted into the hollow bar. They also have the opposing direction threads machined into them.

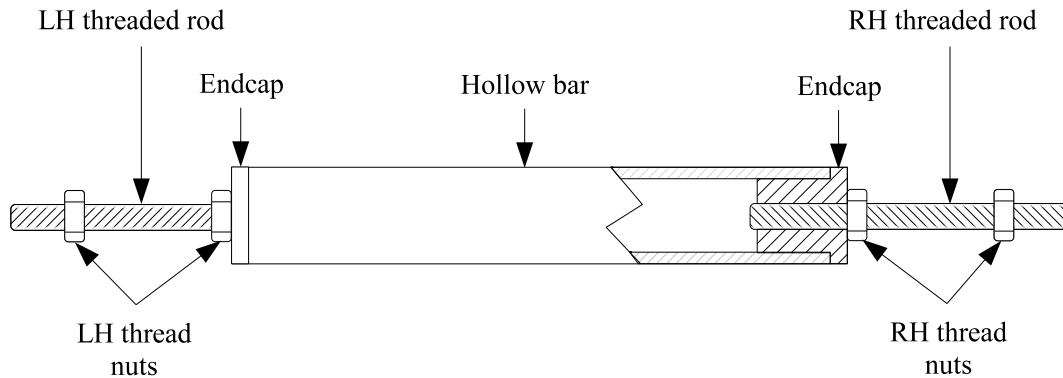


Figure 3.4: Strut assembly showing hollow bar, end caps and threaded rods with locking nuts

The dimensions of the struts are based on the dimensions of those in the mirror support truss in terms of section diameters. The relationship between hollow bar section diameter and threaded rod nominal diameters was also based on that of the support truss struts. Note that, from here onwards, the hollow bar and end cap assembly will be referred to as the central bar, to distinguish between this and the threaded rod parts of the strut. The nuts that lock against the face of the end cap will be called the strut-side nuts, and the nuts locking against the node will be called the node-side nuts.

The nodes of the mirror support truss are hollow spheres cast in iron. Two halves are cast, machined and then joined to form a node. It was not feasible to mimic the exact construction of the nodes for the laboratory model, and therefore a substitute was needed. To minimise cost, it was decided to make use of nodes manufactured from solid steel round bar for the laboratory model, an example of which is shown in figure 3.5. These solid components were then assumed to be rigid compared to the struts and could thus be modelled using rigid bar elements.

For identification purposes, the following naming conventions were established and are also shown in Figure 3.6:

**Top node (TN)** The node at the top of the structure

**Foot node (FN)** Any of the three nodes on which the structure rests

**Central node (CN)** The node at the centre of the structure below the top node

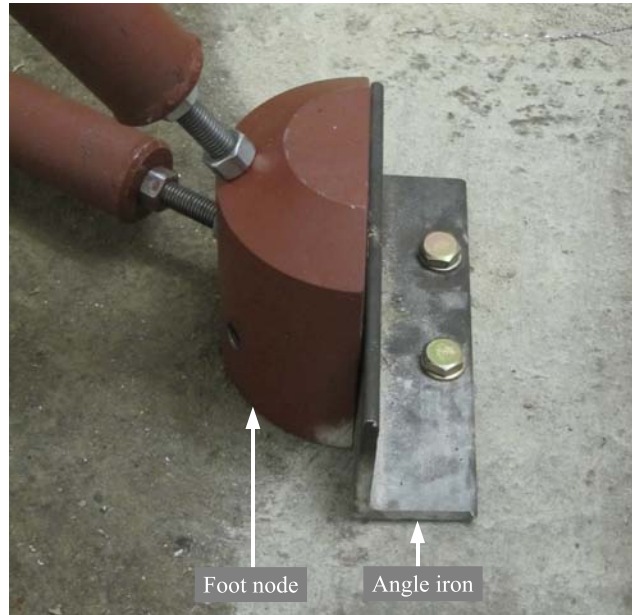


Figure 3.5: Example of one of the solid steel nodes of the laboratory model

**A-strut** Any one of the three struts that are connected between *foot nodes* only

**B-strut** Any one of the three struts that are connected between *a foot node and the top node*

**C-strut** Any one of the three struts that are connected between *a foot node and the central node*

**D-strut** The strut that is connected between *the central node and the top node*

## 3.2 Methodology

During this project it was decided to impose a bottom-up approach by first investigating the structure's building blocks, namely the struts. Once the behaviour and modelling difficulties of this basic element are better understood, the possible sources of modelling error when investigating the structure as a whole are easier to understand.

The aim is that, if this strategy succeeds, the numerical model of a larger and more complex structure can be improved by only removing and accurately modelling single struts at a time. This should minimally jeopardise the structure's integrity.

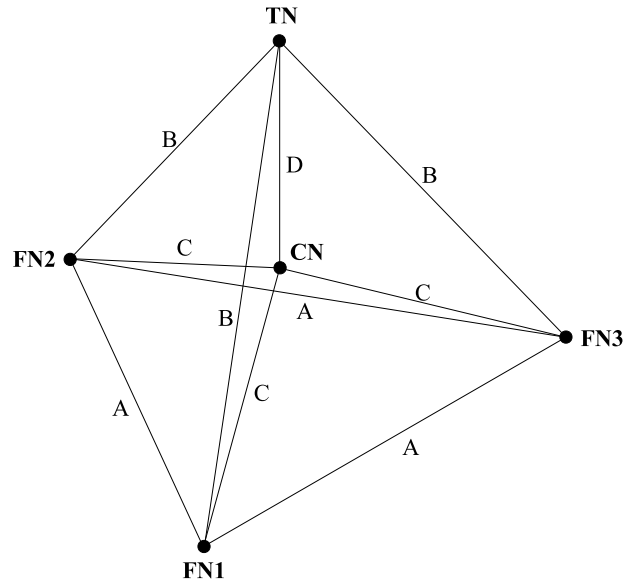


Figure 3.6: Structure component labels

Howell (2004) proposed an updating process consisting of three successive steps, namely coarse tuning, automatic tuning and model validation. These steps were used as a baseline and were then redefined for the specific outcomes of this project with the following:

**Coarse updating** In this step, initial test data is obtained and then changes are made to the FE model by using engineering judgement. This usually involves methods such as adding more modelling detail, checking that correct element formulations are used, investigating the validity of initial modelling assumptions and reconsidering the applied boundary conditions. Ideally, this process runs parallel with the redesign of the testing procedures, since both processes have significant effects on each other. This step is also an important first step to getting a better understanding of the structure's behaviour and can highlight critical areas in modelling sensitivity. By its nature, this is a trial-and-error process and the results are dependent on the skills and experience of the numerical modeller, as well as the person obtaining the test data ((Chen and Wang, 1991)).

**Automatic updating** For this step, the best model obtained during the coarse updating is used as a starting point. For this project the coarse model is used to set up the optimisation problem. Although the accuracy in terms of exact property parameters of the coarse model is not crucial, it should be noted that a flawed initial model for use by the optimiser can

constrain the optimiser. Since a global optimum is usually not clearly identifiable, especially if a Pareto-optimal solution exists, there is a great risk that, although the results are feasible, they may be in a subspace that includes only the current problem's solution. This would result in unstable results if minor changes in the model wants to be investigated. It is during this step that the critical decisions of parameter selection and objective function definition are made.

**Model validation** The final accuracy and robustness of the optimal model are tested. This can be done either by using the model to try to predict outputs other than those used in the automatic updating process, or by making physical changes to the test structure and, using the new modelling methods, build a new FE model and determine its predictive accuracy.

This baseline, combined with the bottom-up approach, provided for a problem-specific methodology outline. However, it lacked detail of the procedures to be followed during the model updating steps of each stage in the bottom-up approach. To address this, the flowchart in Figure 3.7 on page 21 was generated to systematically lay out the steps to be taken during each of the three model updating phases.



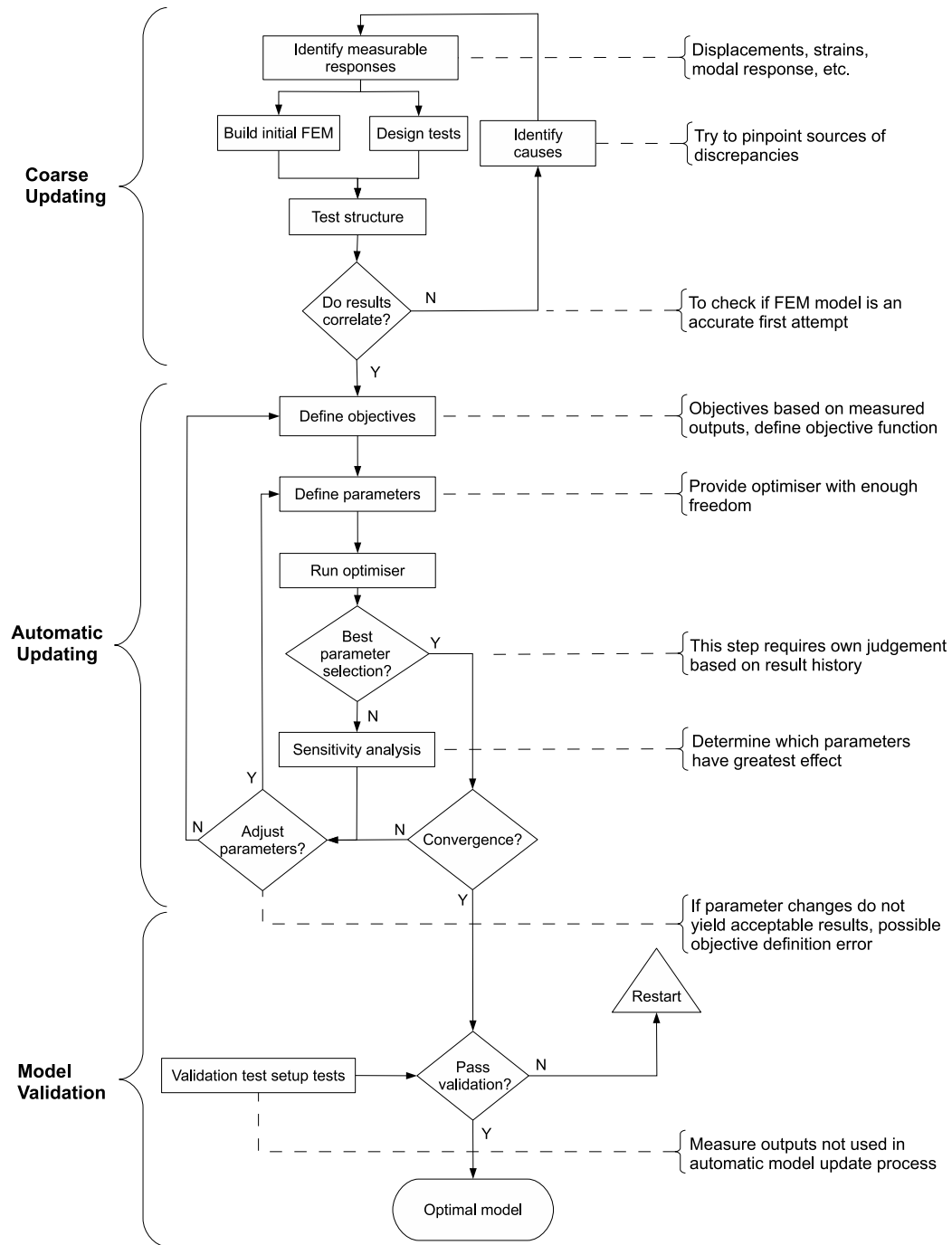


Figure 3.7: Flowchart of proposed methodology

## Chapter 4

# Individual Strut Testing

Due to the significant impact that the accuracy of the individual strut models could have on the model of the assembled structure, the quality of the work done during this stage could be far-reaching. During both the testing and the modelling phases, much was learnt about how to avoid possible pitfalls and which areas of testing and modelling require more attention. More insight was also obtained on how the test setups and modelling methods influence each other, for example the application of boundary conditions.

This dependence between modelling and testing procedures was what guided most of the steps taken during this phase of the project. The result was an iterative process that required various testing setups to be implemented because of complications found when the test results were applied to the modelling steps. In this chapter the detail of the various test setups is discussed and the motivation for each setup is explained briefly. Some of the motivations are because of modelling difficulties, but the details of these difficulties are only discussed in the next chapter.

### 4.1 Selection of Load Cases

As per the first step of the methodology flowchart, the measurable responses had to be identified. These had to be selected whilst bearing in mind how they would be extracted from the numerical model, as well as how they could be defined as objectives in the optimisation model. During this step, it was important to bear in mind that several different load cases would be applied to the same FE model for analysis and optimisation. The different load cases are specified as different boundary conditions and/or loads on the same FE model. This means that the FE model must be the same for all the load cases and, if changes are made to the model, these changes should not affect the boundary conditions of other load cases. For example, one such case was that the optimiser could not perturb node points on which boundary conditions for other load cases were applied during shape optimisation.

Three types of responses were chosen for this study. The first is the strut's response to axial loading. This was chosen since it is relatively simple to obtain this information physically and, because of the nature of the laboratory model, a great deal of the loads will be in the axial direction. For this test the displacement between the outside edges of the node-side locking nuts were to be measured, since this would represent the strut's behaviour when the laboratory model was assembled.

The second is the strut's response to bending loads. Also because of the laboratory model's nature, the struts would be subjected to bending and thus this information would be useful. These responses are also relatively simple to obtain during testing by means of three-point bending tests, and they provide additional information to the axial behaviour. Because of the simplicity of three-point bending tests, multiple bending subtypes could be obtained merely by moving the supports. Three subtypes were chosen, each providing different information on the struts:

**Bending on hollow bar (BHB):** The supports are placed to the inside of the end caps, thus only the behaviour of the hollow bar is measured (BHB in Figure 4.1)

**Bending on end caps (BEC):** The supports are placed 15 mm to the inside of the central bar so as to incorporate the effects of the end caps (BEC in Figure 4.1)

**Bending on rods (BR):** The supports are placed on the threaded rods of the struts, thus capturing the bending behaviour of the entire strut (BR in Figure 4.1)

For the last subtype, the supports are placed to the inside of the node-side locking nuts for practical testing reasons. Firstly, if the supports were to be placed to the outside of the node-side locking nuts, coinciding with the axial test boundary conditions, the numerical model would include the bending stiffness of these nuts. However, in practice this is not the case, since these nuts are not tightened against anything during the bending tests and, because of the geometry of the supports, the nuts would interfere in their positioning. Therefore it was decided to remove the nuts during testing and to position the supports towards what would be the inside edge of the node-side locking nuts, as shown in Figure 4.1.

The third response type is the dynamic behaviour of the struts. Although static behaviour is of more interest for the purposes of this project, the dynamic behaviour would aid the modelling. Because updating this model is an inverse problem with a multitude of possible solutions, providing more information to the optimiser aids the process of finding better suited, more realistic solutions. As this information can also be extracted easily and accurately from

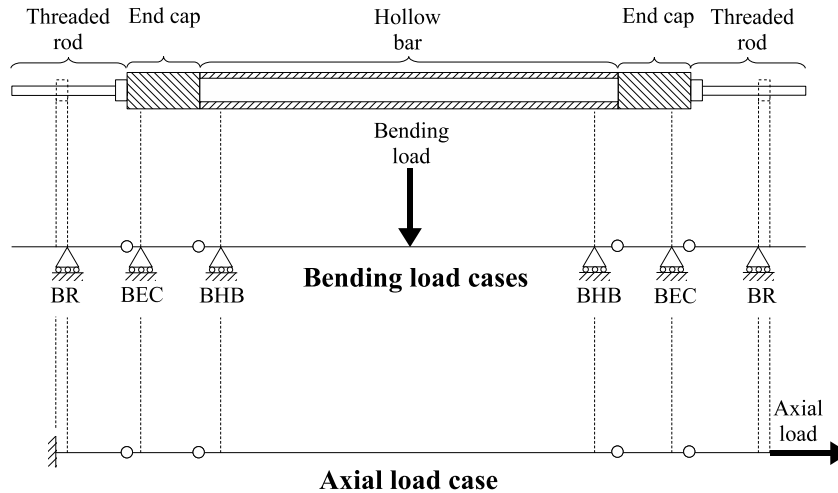


Figure 4.1: Boundary conditions for selected load cases

the struts during testing, this load case would be of great benefit, for little cost in resources.

## 4.2 Axial Load Case Tests

To do the axial tests, an MTS Model 312.31 load frame, fitted with a solenoid-controlled four-way valve was used, as shown in Figure 4.2. The load frame is constructed by two steel blocks clamping two round solid steel bars. The bottom clamping block is used as the fixing point for the hydraulic cylinder, which protrudes through the block. The top clamping block serves as a stationary fixing point for the test sample, and this block can be fixed at any height along the solid steel bars.

An MTS 407 controller was used to control the cylinder and received feedback from an internal displacement controller in the cylinder. This could be used to apply cycles of tensile and compressive loads and, by having a load range covering both tension and compression, a possible non-linear response could be identified easily.

### 4.2.1 First axial test setup

The test setup shown in Figure 4.3 is the initial test setup. An HBM S9 10 kN load cell was installed in-line with a thread adapter to convert the left-hand thread of the strut to fit into the load frame's right-hand thread. A metal tab was welded to this adapter to serve as a measuring point for the HBM WI/10 mm -T linear variable differential transformer (LVDT) displacement

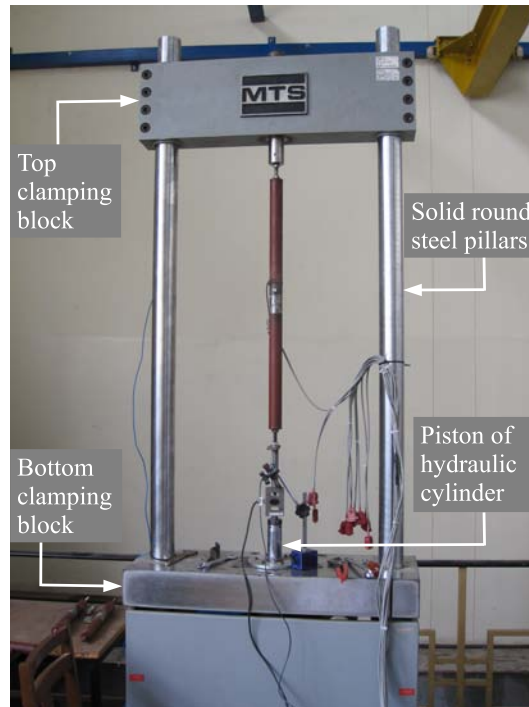


Figure 4.2: Axial test load frame

transducer. The load frame's bottom clamping block was used as a datum, whilst the hydraulic cylinder moved during testing.

The results of this setup were repeatable in the sense that the load vs. displacement plot showed little deviation during cycles. However, as shown in Figure 4.4, the measured response curve represented behaviour similar to hysteresis which is far from the linear behaviour expected such as the linear fit shown by the green line. To obtain the compliance value, a linear fit was made through the measured data using least squares linear regression, and the gradient of this fit then is the compliance.

#### 4.2.2 Second axial test setup

At this point it was believed that the load cell, in combination with the thread adapter, could be a source of the hysteresis type of behaviour. Because the thread adapter was essential for testing, and since the struts were at that point already fitted with strain gages in such a manner that they could measure load in the strut, the S9 load cell was used to calibrate the output of the strain gages. With this calibrated output, the S9 load cell was removed from the setup and the load was measured using only the strain gages.

This second iteration of the setup yielded improved results, and an example of the typical response that was measured is shown in Figure 4.5. As shown,

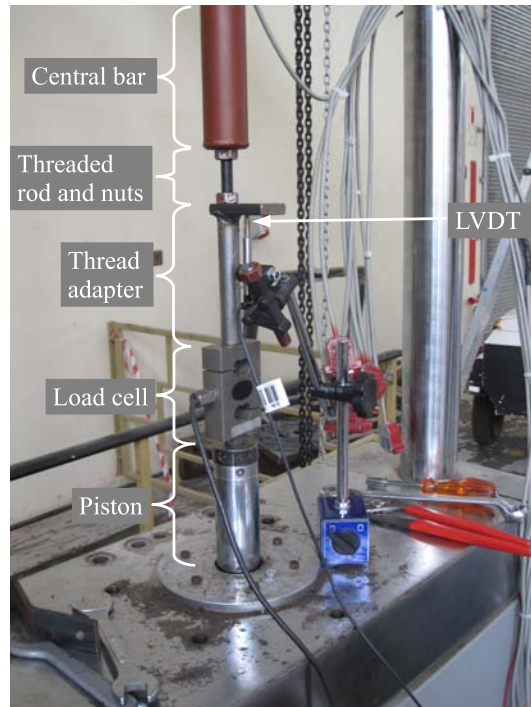


Figure 4.3: Bottom components of first axial test setup

the results are again repeatable, but the norm of the residuals of the linear regression improved from 0.718 for the previous test setup to 0.147 for this setup. The norm of residuals is the square root of the residual sum of squares of the linear regression, and therefore a lower value indicates a better fit.

At this point, these results were deemed adequate and work on the modelling was continued. However, after multiple attempts and changes in the modelling to try to match the measured axial compliance along with the data from the other load cases, the optimiser could not match this response objective of  $13.2 \mu\text{m}/\text{kN}$ .

According to the modelling results, the axial displacement of the best numerical model obtained was in the order of  $11.1 \mu\text{m}/\text{kN}$  when all the other load case objectives were sufficiently met. These results from the optimiser indicated that there was an error in the measured axial compliance and it was decided to reinvestigate the axial test setup and the measured results.

### 4.2.3 Third axial test setup

Since the LVDT's datum is on the bottom clamping block of the load frame, the flexure and extension of the load frame were suspected to influence the measured compliance more than expected. Tests were done on the load frame, where the total extension between the bottom and top clamping blocks were

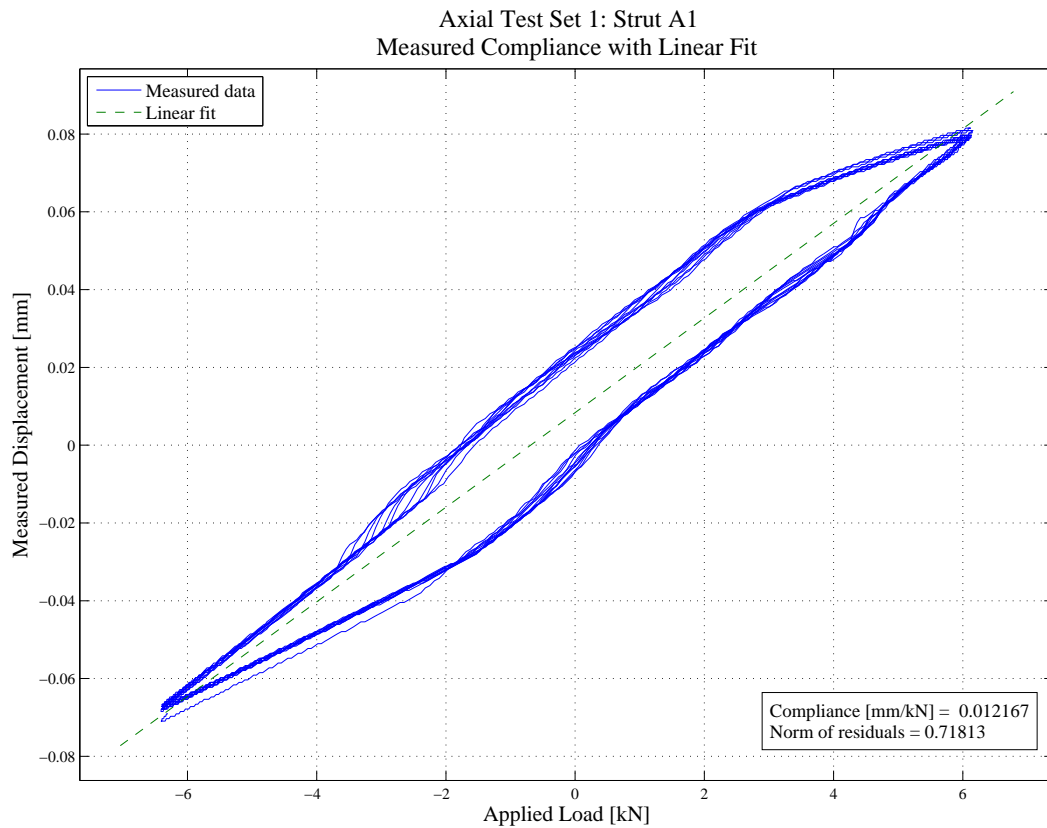


Figure 4.4: Typical results of first axial test setup

measured, thus effectively obtaining the compliance of the load frame. These tests confirmed the suspicion, and later investigation showed that the top clamping block of the load frame was made out of aluminium, and not steel as initially assumed.

Since the compliance of the load frame was now known, the axial results could be corrected by taking this into consideration. It was decided, however, to rather redesign the test setup and to repeat the tests so that confidence in the measured data could be restored.

The third iteration's setup required that only the extension of the strut was to be measured, isolated from external displacements. To do this a second metal tab was welded to the top fixing point of the load frame and, like the bottom fixing point, the top node-side locking nut locked against this tab. A rod was then fixed to the top tab, extending downwards, parallel to the strut, almost to the bottom metal tab. The LVDT was then fixed to this rod and positioned in such a manner that the extension between the two metal tabs, which is also the extension of the strut, could be measured. This isolated the

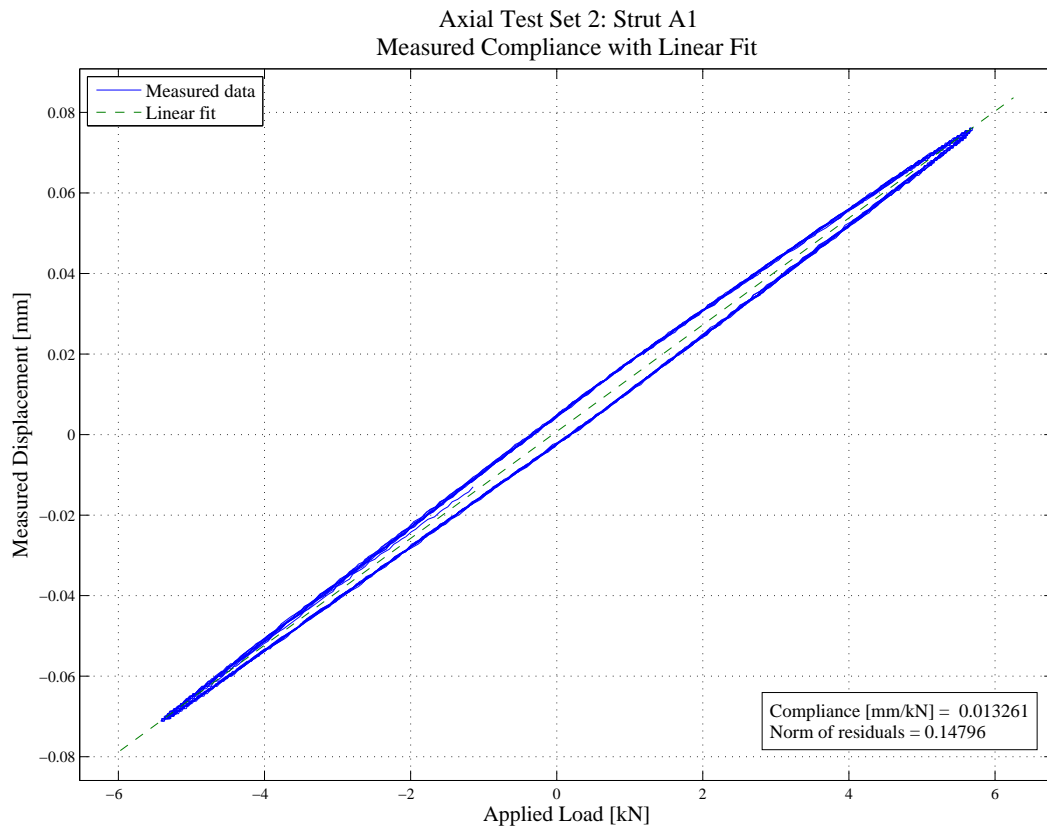


Figure 4.5: Typical results of second axial test setup

external deflections of the load frame, measuring only the strut's extension. The difference between setups 1 and 2 and setup 3 is shown in Figure 4.6.

The results of this setup compared better with those that the numerical model predicted at the time than with those of the previous setup, with the measured compliance of the A-strut being  $10.35 \mu\text{m}/\text{kN}$ . Although this is still lower than predicted by the current numerical models, these results were deemed to be the actual behaviour of the strut and were then used as the new axial objective for the optimisation model.

Once an acceptable numerical model for the A-strut was obtained, the modelling of the other struts started. Only during this phase did it become apparent that the measured compliances for the struts had no linear relationship to the length of the struts. In Table 4.1 the measured compliances of the struts are shown in the first column and the lengths of the struts normalised by the length of the A-strut are shown in the second column. Here one can see that, although the length of the struts becomes shorter, the measured compliances stay relatively unchanged.



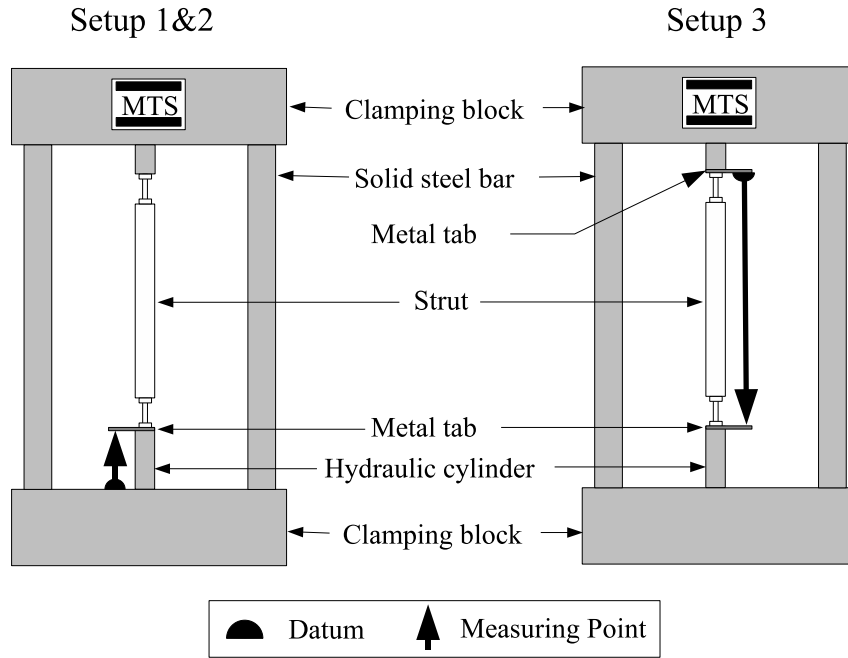


Figure 4.6: Difference in datum between setups

Table 4.1: Results of third axial test setup

Strut type	Average compliance [ $\mu\text{m}/\text{kN}$ ]	Relative length
A	10.4	1
B	10.8	0.93
C	9.7	0.53
D	10.8	0.39

A possible explanation for these results was thought to be that most of the measured compliance was in the threaded rods only, since the lengths of these are the same for all the struts. Although the numerical model of the A-struts showed that most of the strain was in the threaded rods, it also showed that a significant amount of strain was contributed by the central bar. This led to doubt in the measured data and therefore also in the numerical model.

In an attempt to reduce the uncertainty as to why the different struts' compliances were so similar, another set of tests was performed. In these tests the same setup was used, but only the central bars without the threaded rods were tested to try to get an indication of the scale of their compliances. Be-

cause the measurement resolution of these tests was not high enough —some extensions were below  $2 \mu\text{m}/kN$ — they could not be used to accurately determine the exact compliances of the central bars. They did, however, provide a rough indication of the scale of the compliances and also showed a linear relationship with the strut lengths. This meant that there should be a significant difference in the measured compliance of the entire strut for the different strut lengths. Thus the proposed current explanation that the threaded rods were the main contributors to the measured compliance was disproved and further investigation was necessary.

#### 4.2.4 Final axial test setup

To obtain more accurate results it was decided to design a new test setup that could provide more insight into the compliances of each of the different parts of the strut. The parts of interest were the left-hand threaded rod and nuts, the right-hand threaded rod and nuts, and the central bar. The expected extensions to be measured were too small for the resolution of any of LVDTs available at that time. An HBM DD1 clamp-type extensometer was available and had a small enough resolution. This extensometer was modified by removing its clamps and a probe with a  $90^\circ$  angle was made and fitted to the transducer. The transducer was then bolted to an extension so that it could be fixed at various heights. Figure 4.7a shows the extensometer and its extension fixed in the top-most measurement position, while Figure 4.7b shows a closer view of the extensometer and its probe.

In order to be able to use this modified extensometer, it had to be held in place in such a manner that the probe could be placed on various surfaces of the strut. As observed with the previous setups, the datum of the measurement had to be isolated from external deflections. For this purpose a bracket was made that provided a surface parallel to the length of the strut for the extensometer to be clamped onto. This is shown in Figure 4.7a. The bracket was then welded to the hydraulic cylinder insert. This insert screws into the hydraulic cylinder and has the correct size thread for the strut.

To provide suitable contact surfaces for the extensometer's probe, two aluminium angle profiles were fixed to the strut, as also shown in Figure 4.7b. One angle profile was fixed into position by the top-most locking nut and the other was glued to the top face of the central bar. It was decided to use glue rather than to also have the angle profile fixed by the strut-side nut because the latter could introduce new uncertainties into the assembly of the strut. The bottom face of the central bar was a suitable contact surface and did not need to be adapted. This then provided three points that provide information on each of the three interested parts of the strut.

Furthermore, since the strut's extension is measured in isolation of external effects, a load cell was reintroduced to the test setup. This load cell provided a

constant reference of applied loads between all the struts, as opposed to having each strut providing its own load readings.

With the previous test setups, the applied load had to be tuned by adjusting the stroke amplitude of the hydraulic cylinder on the MTS controller, since only displacement feedback was available. This proved cumbersome and, in some cases, especially when switching from a longer strut to a shorter strut, the strut could be overloaded if care was not taken to adjust the stroke length.

For this reason, and also in an attempt to improve the quality of the measured data in terms of repeatability, it was decided to change the controller's feedback from displacement to force feedback by using the load cell. This was done by using the load cell's output as the feedback for the controller. Because the load cell was connected to the controller unit, the measured load output had to be obtained from an output of the controller. To ensure that the correct load was being recorded, the controller's load output was first calibrated by inserting a calibrated load cell in line with the setup and measuring its output directly. The controller's output could be calibrated using this calibrated output. This procedure was done again after all the testing to check that the controller's output was still accurate. The maximum absolute error in both cases was below 0.3 N, and therefore was sufficiently accurate.

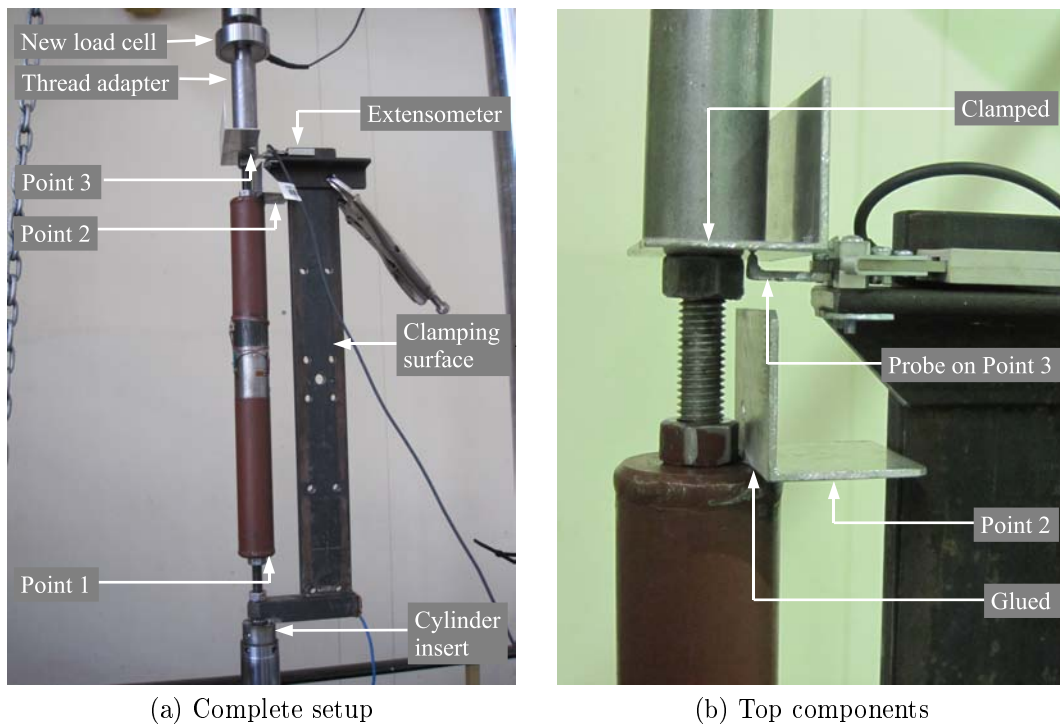


Figure 4.7: Final axial test setup

During testing, measurements of each strut were taken individually at the three points shown in Figure 4.7 by moving and fixing the modified extensometer and its extension to each point's location on the clamping surface bracket. Each of these points provides information about each of the three sections of interest on the strut. To check for setup repeatability, each strut was measured at its three points, the nuts were loosened and then re-tightened, and then tested again. With this setup, sixty usable sets of measured compliances were obtained. An example of the test results is shown in Figure 4.8, and one can clearly see the improvement in the quality of the data, with the norm of the residuals of the linear regression being in the order of only 0.01.

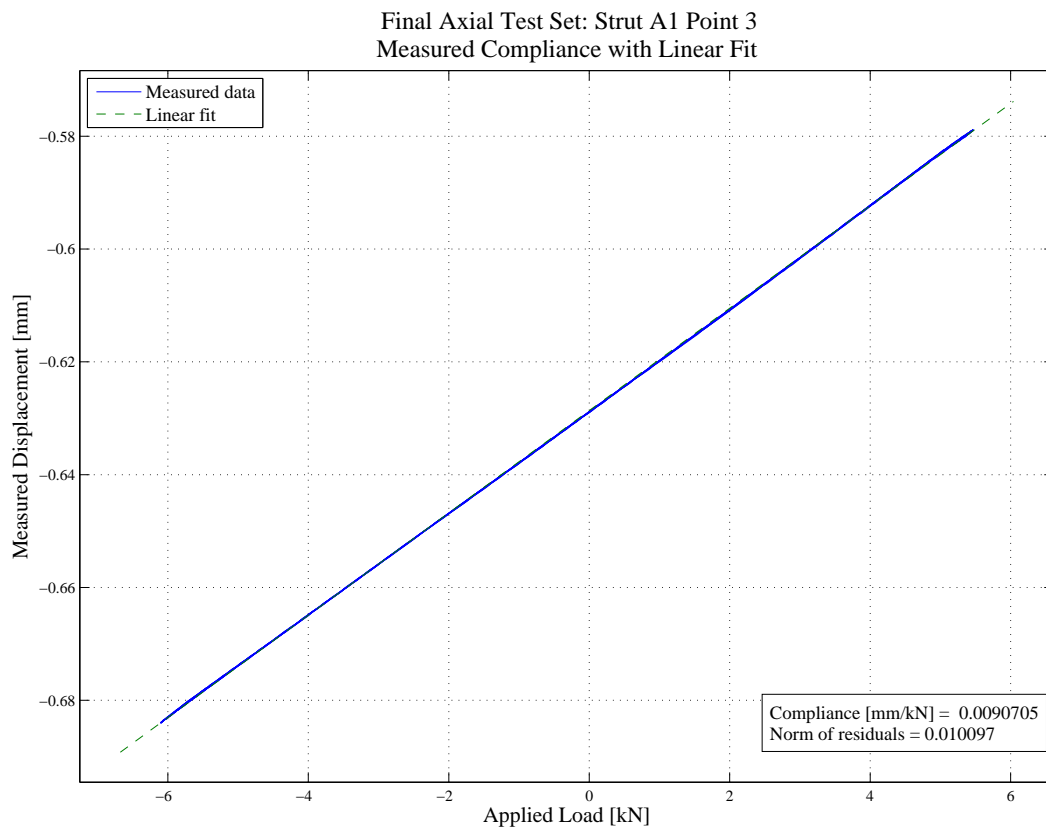


Figure 4.8: Typical results of the final axial test setup

Note that all three points share the same datum and thus the compliance for each individual part was calculated in post-processing. The individual compliances were calculated from the measured compliances taken at the various points, as follows with reference to figure 4.7:

**Left-hand threaded rod and nuts:** Point 1

**Central bar:** Point 2 minus Point 1

**Right-hand threaded rod and nuts:** Point 3 minus Point 2

During testing, the length of the left-hand threaded rod and nuts could be controlled and was fixed at 50 mm. Due to the nature of the setup, the length of the right-hand threaded rod and nuts varied between 49.5 mm and 52 mm. This meant that the measured compliance of these had to be normalised first. The normalisation was done using the 30 mm of exposed thread between nuts, and not the 50 mm that includes the nuts, since the exposed thread was the only part of which the length varied.

From the normalised data the mean of the compliances was  $3.27 \mu\text{m}/kN$  and  $2.71 \mu\text{m}/kN$  for the left- and right-hand threaded rods respectively. Since this would provide unnecessary complexity in the modelling, the mean of all the threaded rod compliances, namely  $2.99 \mu\text{m}/kN$ , was taken as the compliance per threaded rod. Thus, in each strut the compliance due to the threaded rod and nuts on both sides would be  $5.98 \mu\text{m}/kN$ .

For the central bars, the mean of the six measured compliances per strut was taken as the compliance value for that strut, the results of which are plotted in Figure 4.9. From these results it is clear that there is a wide error band of the scatter between measured results. It is suggested that the testing of more struts could provide a higher confidence in the fitted data, but for the purpose of this project these results provided a sufficient indication of a linear relationship between the length and compliance of the central bars of the different struts. For data-matching it was decided to use the mean value of the measured data of each strut and not that of the linear fit, because the mean values of each strut type were deemed more accurate than those of the linear fit.

These results were then the final sets of data that would be used in the optimisation process as objectives to match. For each strut, its total compliance then is the sum of the compliances of the central bar and the threaded rod and nuts on both sides. Table 4.2 summarises the values for each strut.

### 4.3 Bending Load Case Tests

The bending load case tests were done on an Amsler Type 30 SZBD 56 load frame because its test bed is wide enough to accommodate the length of the struts. It also has adjustable supports to vary the length, making this machine more suitable for the three bending load case variants as described earlier in the load case selection in Section 4.1.

The WI/10 mm-T LVDT was used for the measurement of displacement. It was positioned below the strut, directly beneath where the load was applied,

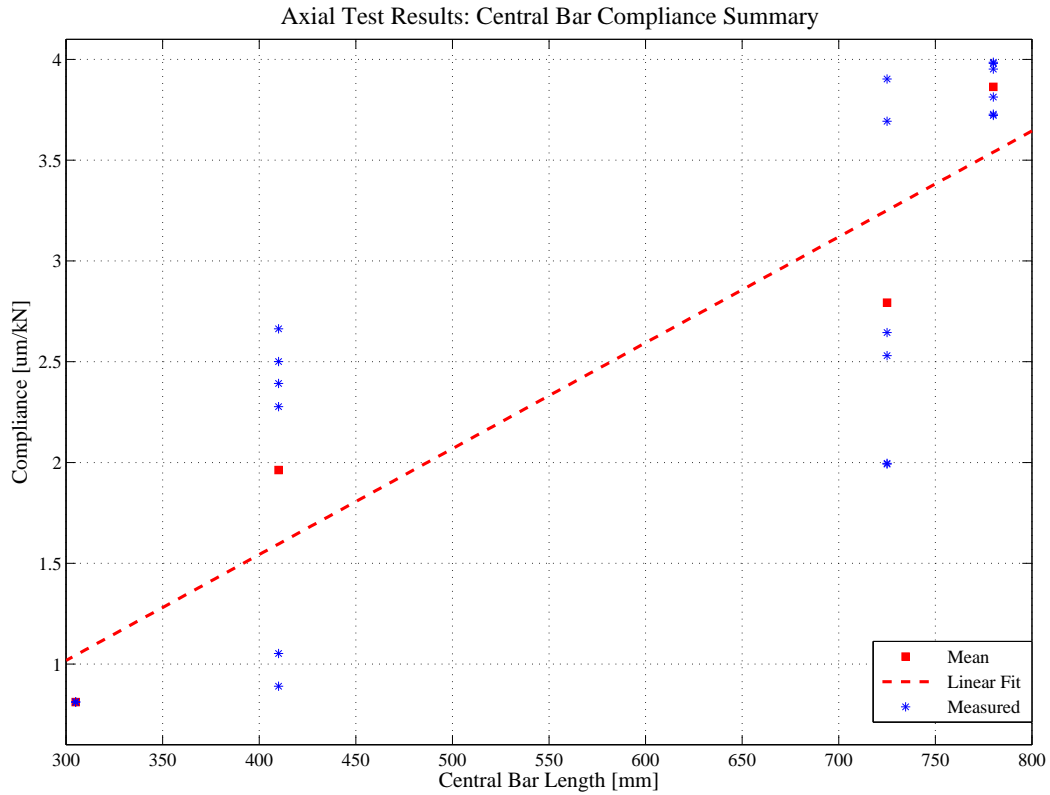


Figure 4.9: Final results for the central bar compliances

as seen in Figure 4.10. Magnets were used to position the struts and to keep them from rolling and shifting on the supports.

The hydraulic controls of the Amsler machine are manual and provided some difficulty in trying to obtain load cycles with repeatable amplitude. However, once the struts were seated under load, no drift was measured and the response to the applied load cycles was repeatable, as shown in Figure 4.11. Note that the strut had to remain under compressive load once applied so that reseating could not occur, and therefore the graph in the figure only shows the recorded measurements of the load cycles after seating.

Each of the struts was tested for each of the three bending load variants. Each of the tests was performed twice to check that shifting on the supports did not occur during testing. Thus, for each bending load case variant there are six measured values. The bending over the hollow bar tests could not be performed on the shorter C and D type struts. This was because the supports used for these tests, were too wide and could not be moved as close to each other to provide the small distance required whilst allowing enough space for

Table 4.2: Final compliances for different struts

Strut type	Central bar compliance [ $\mu\text{m}/\text{kN}$ ]	Total compliance [ $\mu\text{m}/\text{kN}$ ]
A	3.86	9.84
B	2.79	8.77
C	1.96	7.94
D	0.81	6.79

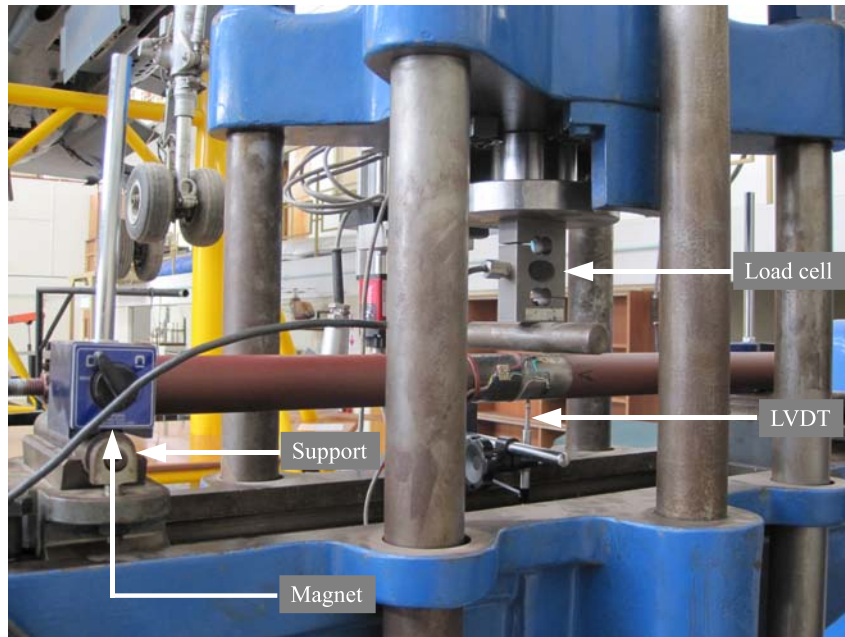


Figure 4.10: Bending load case setup

positioning the LVDT as well.

With respect to what was observed during the axial load testing, a check had to be done to make sure that there was a linear relationship between the measured displacements and the strut lengths to ensure that there were no major problems with the test setup.

As opposed to the axial tests, the nature of the three-point loading on the struts did not necessarily mean that there was a linear relationship between strut length, support width and central displacement. Since the support width has a significant effect on the magnitude of the moments applied to the different sections of the strut, a direct relationship between strut length and central

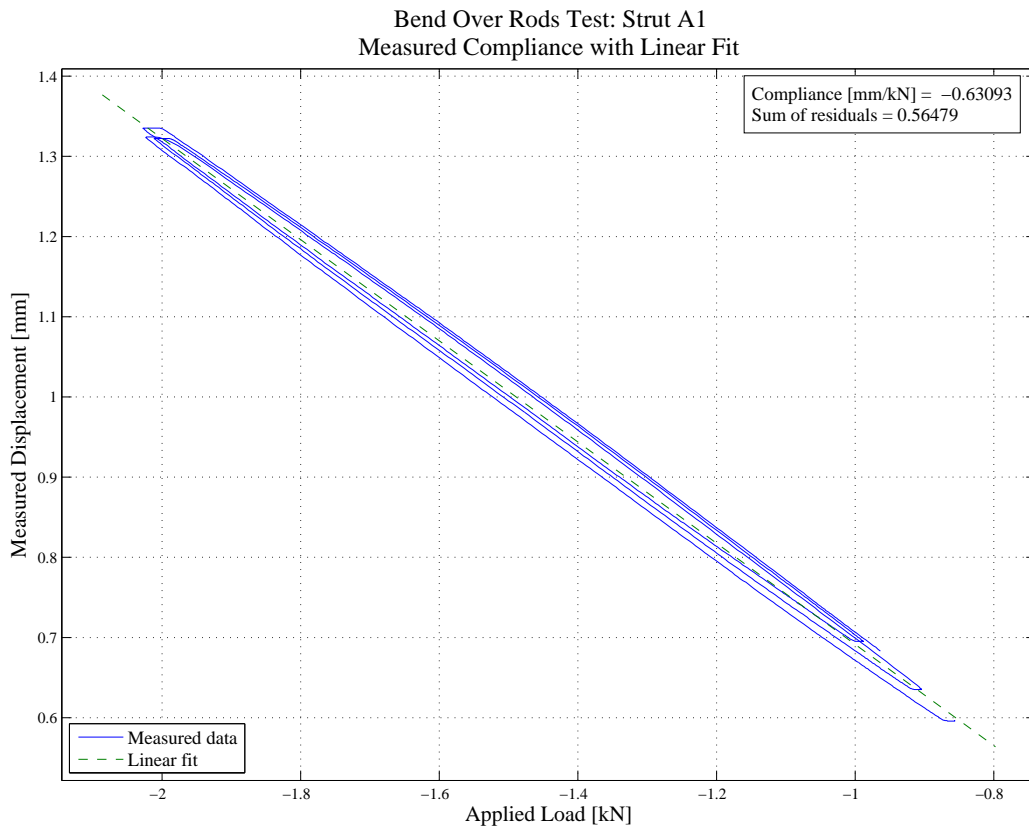


Figure 4.11: Result of bending over rods test

displacement cannot be expected. Therefore it was decided to find a means to normalise the measured data so that a reasonable comparison could be made between the strut types and their measured displacements.

Since only a reasonably accurate normalisation factor would be sufficient, it was decided to build preliminary FE models of each of the struts that contained the detail of the hollow bar, end cap section, nuts and threaded rods. The dimensions of these interim models were those specified in the design of the laboratory structure. Note also that the end caps were modelled simply as solid sections.

By using the central displacements of these numerical models under three-point loading, and dividing them by the central displacement of the A-strut's numerical model, normalisation factors were obtained for each of the three bending load cases of each of the four strut types. The numerical displacement results are shown in Table 4.3, along with the calculated scaling factors.

The measured displacements were then normalised by multiplying them by these factors and the results are shown in the graph in Figure 4.12.



Table 4.3: Numerical displacements for bending load cases and subsequent bending normalisation factors

	Over rods		Over end caps		Over hollow bar	
	Disp. [ $\mu m$ ]	Factor	Disp. [ $\mu m$ ]	Factor	Disp. [ $\mu m$ ]	Factor
<b>A</b>	700	1.00	418	1.00	195	1.00
<b>B</b>	588	1.19	333	1.26	146	1.34
<b>C</b>	190	3.68	56	7.46	11	18.22
<b>D</b>	130	5.38	22	19.00	2	100.00

Table 4.4: Measured displacements for bending load cases

	Over threaded rods		Over end caps		Over hollow bar	
	Mean	Std. dev.	Mean	Std. dev.	Mean	Std. dev.
<b>A</b>	627.8	8.59	348.8	3.82	163.3	2.36
<b>B</b>	517.3	3.72	282.2	4.40	122.0	0.89
<b>C</b>	173.5	2.59	46.6	0.44	-	-
<b>D</b>	141.5	0.71	21.0	0.64	-	-

From this graph it can be observed that all the scaled measurements, except for those of the short D-strut, have the same values given some error bounds. Only the short D-strut seems to have a notably higher compliance, and the suspected reason for this is that, in relation to the other struts, the edge effects are more prominent during testing. Despite this, these results were deemed to be sufficient evidence that there is indeed a predictable linear relationship between the strut lengths and the measured displacements, thus proving that there are no major problems with the test setup. The measured displacements therefore are suitable to be used as targets for the optimisation phase. The final displacement values used for each load case of each strut is the mean of the six measurements taken, and these values are shown in Table 4.4.

## 4.4 Dynamic Load Case Tests

The objective of the dynamic load case tests was to obtain the values of the first three unconstrained natural frequencies of each strut. To determine these natural frequencies, their frequency response functions (FRFs) had to be obtained. To obtain these, the structure had to be excited using some force input,

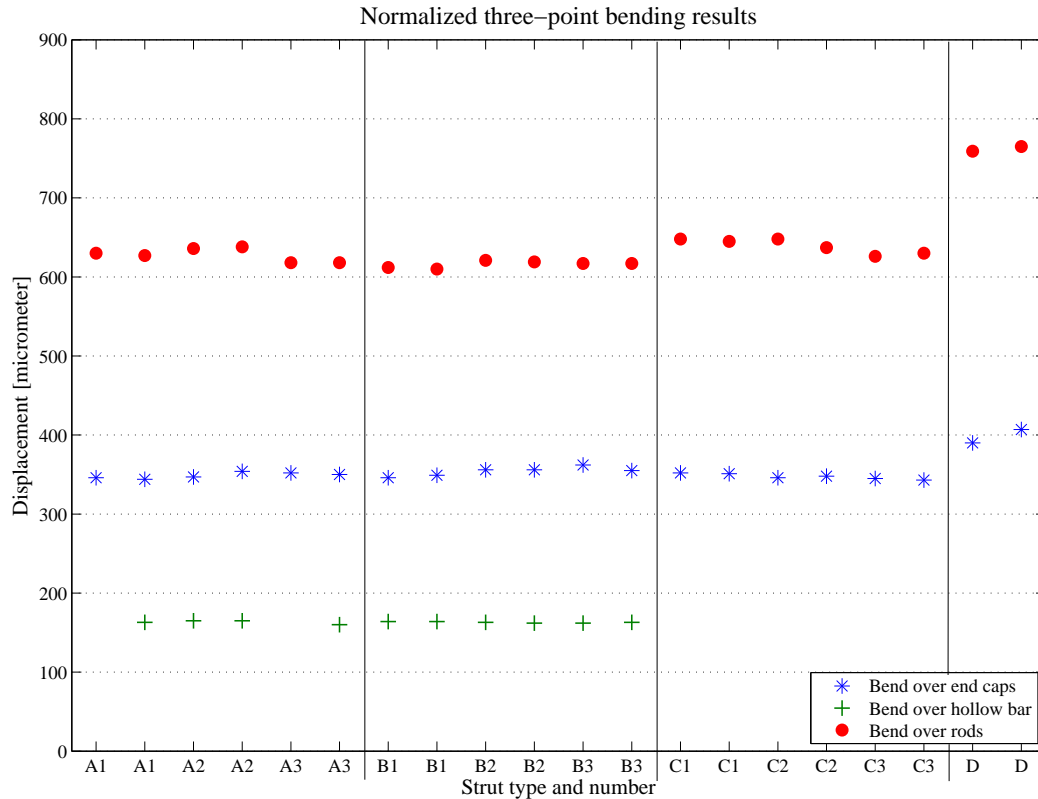


Figure 4.12: Normalised bending results

and the resulting response of the structure was measured using accelerometers.

To do so the strut was fitted with four accelerometers at the positions shown in Figure 4.13, based on mode shapes obtained from a preliminary FE model. By studying these mode shapes, the positions could be selected to ensure that all the modes would be captured. This is done by ensuring that there is at least one accelerometer at each natural frequency that will be subjected to accelerations that are great enough to be measured.

The strut was excited with a shaker, since it provides more energy than a modal hammer, resulting in clearer FRFs. The stinger of the exciter was fitted with a load cell that in turn was fitted with a magnet, which would be fixed to the strut at the position shown in Figure 4.13. Finally, the struts and the shaker were suspended by elastic cords to provide what are effectively unconstrained boundary conditions.

It has to be borne in mind that, for modelling, a single geometry will be used for all the load cases and that, for the axial load case, the node-side locking nuts have to be modelled as well. Therefore the natural frequencies

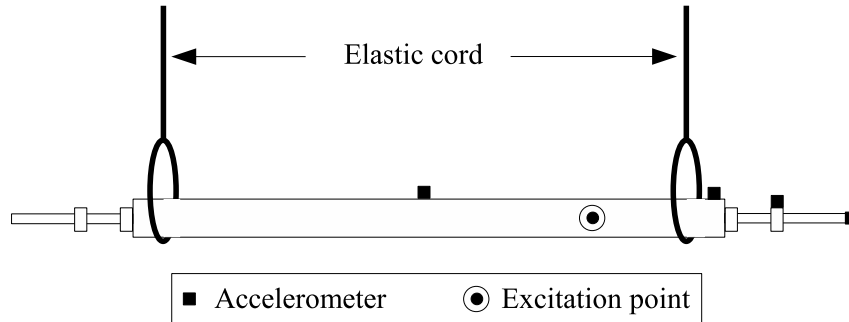


Figure 4.13: Test setup for obtaining the frequency response functions

Table 4.5: Measured natural frequencies

Mode number	A-strut	B-strut	C-strut	D-strut
Mode 1 [ $Hz$ ]	290.9	328.9	640.1	720.9
Mode 2 [ $Hz$ ]	530.9	697.8	714.8	851.9
Mode 3 [ $Hz$ ]	701.6	848.3	1123.4	1812.4

also had to be measured with these nuts in their positions on the threaded rods. To comply with this requirement, these nuts were glued into the position they were in when the struts were subjected to the axial loading tests.

The software used was LMS testLab v10A, which includes the natural frequency extraction algorithm, polyMAX. This algorithm identifies possible frequency nodes and poles and also determines which of these are stable. Stability is determined by the recurrence of the pole within all the samples measured. However, it is still dependent on the user to identify which of the poles are applicable and which are a result of measured noise or are repeated modes. Repeated modes often result because, in certain cases, a structure will have mode shapes that are symmetric about a certain axis and these should theoretically occur at the same frequency. However, these symmetric modes often appear as two distinct frequencies lying close to each other. Here it depends on the user's insight to determine whether a frequency identified by the algorithm is an independent natural frequency, or whether it is an echo of a symmetric mode.

Table 4.5 shows the measured results of the tests. These became the dynamic load case objectives to guide the optimiser in finding a solution.

This concludes this chapter on the detail of the tests done on the individual struts. The results of the tests in this chapter will be used in the next chapter, which covers the numerical modelling of the individual struts.

## Chapter 5

# Numerical Modelling of Individual Struts

The purpose of this phase of the project is two-fold. The first and foremost purpose is to find an acceptable numerical modelling technique for modelling the individual struts. The second is to investigate the amount of modelling detail required to produce such a model. To achieve the latter, the modelling process started on a simplified model of the strut. From this model, each incremental improvement will be documented and the results thereof will be investigated.

As discussed in the methodology in Chapter 3, the modelling process would start by adding modelling detail to the FE model. This step, the coarse updating step, does not make use of any optimisation methods. Additions are made by using engineering intuition based on the results obtained.

The second step, the automatic updating step, makes use of optimisation methods to make improvements to the model. Although the optimisation methods are useful and effective, they are still dependent on sound engineering judgement to make additional changes. The optimisation does, however, serve to guide the types of changes that could be made and, in that regard, also is an effective tool.

The process of finding the correct modelling technique is first done on the A-strut only. Once the techniques have been refined they will be applied to the remaining struts, so that customised models of each strut type — not each individual strut — are obtained.

### 5.1 General Modelling Details

As discussed in the previous chapter also, the load cases for the numerical model had to be defined in such a way that all the individual load cases could be defined on the same model geometry without having one load case imposing unwanted boundary conditions on another load case. With this requirement,

and with the physical limitations experienced during the testing phase, the load cases were set up in the numerical modelling as described below with reference to Figure 5.1:

**Axial** Point **A** is fixed for all six degrees of freedom and a tensile force (positive x-direction) is applied at node point **I**

**Bending on rods** Points **B** and **H** are fixed in the z-direction only and a load in the negative z-direction is applied at point **E**

**Bending on end caps** Points **C** and **G** are fixed in the z-direction only and a load in the negative z-direction is applied at point **E**

**Bending on hollow bar** Points **D** and **F** are fixed in the z-direction only and a load in the negative z-direction is applied at point **E**

**Dynamic** No boundary conditions are imposed, since the unconstrained natural frequencies are required

With these boundary conditions the bending load cases are still not constrained in the x- and y-translational and the x- and z-rotational degrees of freedom. For numerical purposes, these degrees of freedom were fixed at point **E**.

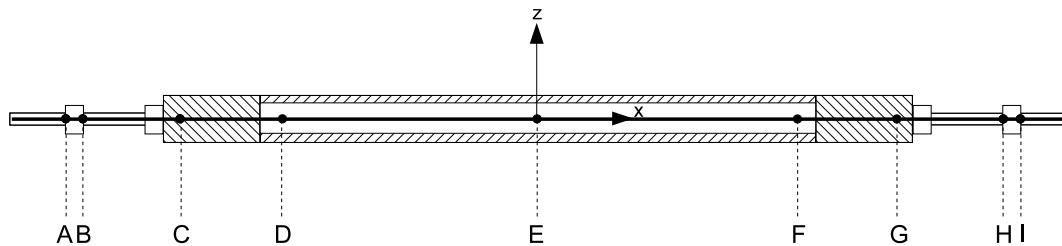


Figure 5.1: Boundary condition application points

Thus the responses for the various load cases are obtained from the numerical model by requesting the following response values:

- Total x-displacement of node I for the axial load case
- Total y-displacement of node E for the bending on rods
- Total y-displacement of node E for the bending on end caps
- Total y-displacement of node E for the bending on hollow bar
- First natural frequency of structure (corresponds to mode 7)

- Second natural frequency of structure (corresponds to mode 9)
- Third natural frequency of structure (corresponds to mode 11)

Note that, since natural frequencies are calculated with no boundary conditions imposed (free-free boundary conditions), the first six calculated modes are the rigid body modes, and thus mode 7 corresponds to the first non-rigid body mode natural frequency. Due to the symmetry of the structure, symmetric modes exist at certain frequencies and therefore the 2<sup>nd</sup> and 3<sup>rd</sup> natural frequencies correspond to the 9<sup>th</sup> and 11<sup>th</sup> modes respectively.

Only one material was defined for the model: mild steel. The properties were set to be those prescribed in the handbook of the Southern African Institute of Steel Construction ((SAISC, 2005)), which are as follows:

**Young's modulus ( $E$ ):** 200 GPa

**Material density ( $\rho$ ):** 7850 kg/m<sup>3</sup>

**Poisson's ratio ( $\nu$ ):** 0.3

For the dynamic responses, the mass of the accelerometers used during the modal tests was modelled by using concentrated mass elements. These elements add mass to a node without adding any structural stiffness.

## 5.2 Coarse Updating

By investigating the original FE model of the mirror support truss obtained from the designers, the method in which the struts were modelled could be identified. Since the objective of this study was to improve the modelling accuracy and modelling techniques for the support truss, and because the original design model is already a simplified model of the struts, this initial model was used as the baseline model for the model updating process.

### 5.2.1 First strut model

The first model is shown in Figure 5.2. In this model there are only two property sets, representing the central bar and threaded rods respectively.

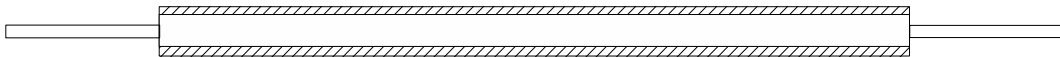


Figure 5.2: First strut model effective cross-sections

The central bar is modelled by applying the properties of the hollow bar to the entire section. Here, beam elements are used with an annulus cross-sectional area with the dimensions of the hollow bar used in the test structure. The outer diameter is 40 mm and the inner diameter is 25 mm .

The threaded rods are also modelled as beams with a circular cross-sectional area. There was uncertainty about what diameter should be used for the section. The common assumption of using the minor diameter of the thread was validated by performing a simple axial loading test on a sample of the M12 threaded rod used in the test structure. The minor diameter of a standard M12 thread is 9.601 mm and, from the test, the effective diameter was calculated to be 9.603 mm . Thus the diameter for this property was set to 9.6 mm .

The axial, the three bending and the dynamic load cases were then added to have five load cases in total. For the FE analysis, each load case with its specific boundary conditions was evaluated individually and the results of the relevant displacements were then recorded.

The results of this model, which is shown in Table 5.3, indicated that the model lacks structural stiffness for both the axial and the bending load cases when compared to the measured data. It was also noted that, although the dynamic responses were accurate to within 7%, the error in the static responses was as much as 22.1%.

Table 5.1: Summary of the results of the first strut model

Objective response	Target	Current	Error [%]
Axial	$[\mu m]$ 9.83	12.00	-22.08
Bend: Rods	$[\mu m]$ 627.00	759.40	-21.12
Bend: Hollow bar	$[\mu m]$ 163.00	195.10	-19.69
Bend: End caps	$[\mu m]$ 349.00	418.20	-19.83
Frequency 1	$[Hz]$ 290.9	310.5	-6.74
Frequency 2	$[Hz]$ 530.9	561.0	-5.67
Frequency 3	$[Hz]$ 701.6	679.3	3.18

## 5.2.2 Second strut model

The second model, as shown in Figure 5.3, addresses the lack of stiffness of the first model by replacing the hollow bar cross-section with a circular cross-section property in the areas where the end caps are inserted. The end caps are simplified to have a solid circular cross-section by assuming that, with the end caps fitted into the ends of the hollow bar, their cross-sectional areas

effectively becomes circular. Thus the diameter of the cross-section is taken to be the same as the outer diameter of the hollow bar, which is 40 mm .

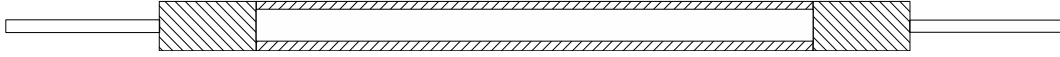


Figure 5.3: Effective cross-sections of the second strut model

As shown in table 5.2 this change caused an improvement to both of the errors mentioned previously by reducing the axial error from 22.1% to 7.8% and the bending over the rods error from 21.1% to 14.5%. However, the error for the bending over the end caps was increased from 19.8% to 20.2%, while the error for the bending of the hollow bar remained unchanged. The maximum error for the frequency load case was increased from 6.7% to 16.9%. Overall, the maximum error was thus decreased from 22.8% to 20.2%, which was for the bending over the end caps load case. Although improvements have been made, the model still lacks stiffness and the dynamic responses have worsened.

Table 5.2: Summary of the results of the second strut model

Objective response	Target	Current	Error [%]
Axial $[\mu m]$	9.83	10.60	-7.83
Bend: Rods $[\mu m]$	627.00	718.10	-14.53
Bend: Hollow bar $[\mu m]$	163.00	195.10	-19.69
Bend: End caps $[\mu m]$	349.00	419.70	-20.26
Frequency 1 $[Hz]$	290.9	322.3	-10.79
Frequency 2 $[Hz]$	530.9	620.8	-16.93
Frequency 3 $[Hz]$	701.6	773.4	-10.23

### 5.2.3 Third strut model

For this model there were two possible changes that could be made. The first was to try to find a more accurate model of the end caps. Because the end caps are press-fitted into the hollow bar, there is uncertainty whether they would display the behaviour of a solid cross-section. Given the linear response measured during testing, it was assumed that the shear forces between the two contacting surfaces of the hollow bar and the end caps were greater than the shear forces induced by the applied loads, and therefore that it could be modelled as a solid cross-section. If this was not the case the test data should have revealed noticeable slip-and-stick spikes during loading. Other possible



effects of the end caps could be compensated for by adjusting the parameters of this property set and the effective length of the end caps. Because there was little way of knowing how to make these changes qualitatively, parameter changes of this type are better suited to be set up as an optimisation problem.

The other change was to add the modelling detail of the nuts. Although these would make relatively small changes to the structure, it should be noted that these additions would be placed in the area of the strut that experienced the highest stresses in some of the load cases. Because the threaded rods had a significantly smaller cross-sectional area compared to the central bar, adding elements with greater cross-sectional areas, and at the same time also reducing the length of the exposed threaded rod, was expected to have significant effects.

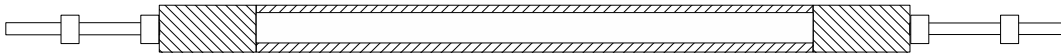


Figure 5.4: Effective cross-sections of the third strut model

Thus, for the third model the nuts were modelled in the positions shown in Figure 5.4. The nuts were also modelled with a simple circular cross-section. The diameter of this cross-section was set to 14 mm, which is the distance between two of the six opposing faces of the hexagon of an M12 nut, as shown in Figure 5.5. The reason is that this is also the outer diameter of the annulus of the effective contact area of the nut, which is also illustrated in the figure. Thus, when the nut was screwed onto its thread, the assumption was made that the area effectively became circular.

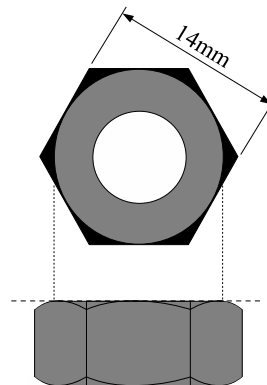


Figure 5.5: Effective contact area of the M12 nut

The results of these additions showed that the axial load case error was reduced further, from 7.8% to 1.4%, but the bending over the end caps error remained the maximum static response error at 19.7%. These results showed

that adding the modelling detail of the nuts significantly improved the axial load case, but did little to improve the bending load case results. Although the first natural frequency error reduced from 10.8% to 1.65%, the second and third natural frequency errors worsened. At this point little, if any, changes could be made to the model that could be justified by engineering judgement, and therefore it was decided to continue to the automatic updating phase.

Table 5.3: Summary of the results of the third strut model

Objective response	Target	Current	Error [%]
Axial $[\mu m]$	9.83	9.97	-1.42
Bend: Rods $[\mu m]$	627.00	693.10	-10.54
Bend: Hollow bar $[\mu m]$	163.00	195.10	-19.69
Bend: End caps $[\mu m]$	349.00	417.80	-19.71
Frequency 1 $[Hz]$	290.9	286.1	1.65
Frequency 2 $[Hz]$	530.9	636.2	-19.83
Frequency 3 $[Hz]$	701.6	778.6	-10.97

### 5.3 Automatic Updating

For the automatic updating, the third strut model setup was used and the necessary changes and additions were made to set up the objectives for the optimiser. As discussed in the literature survey, the objectives were defined by setting the optimiser to minimise the error between the model's response and a target value for a given response type. For this problem there were four displacement responses and three dynamic responses, and these add up to seven individual objectives. The target values of these objectives were set to be the measured values of the respective responses. These seven individual objectives had to be combined to form a single objective function. For data-matching problems, the objective function for multiple objectives is by default defined by the optimiser as (GENESIS, 2008):

$$F = \sum_{i=1}^{NR} [M_i(R_i - T_i)]^2$$

Here,  $NR$  is the number of responses,  $M_i$  is a user-defined weighting factor,  $R_i$  is the current response and  $T_i$  is the target response.

When the user does not specify the values of the weighting factors they are by default calculated internally as:

$$M_i = \frac{1}{\text{Max}(|T_i|, 0.01)}$$

This means that the error values for each response are scaled by its target value unless the target value is smaller than 0.01, in which case it will be scaled by 0.01. For this problem the targets of the static responses are all in  $1e^{-6}$  order of magnitude and thus smaller than 0.01. Therefore this constant was changed to  $1e^{-6}$  so that the scaling was correct for the target values of this problem.

This means that, should the target values be greater than  $1e^{-6}$ , the objective function will be:

$$F = \sum_{i=1}^{NR} \left( \frac{R_i - T_i}{T_i} \right)^2$$

If the target value is less than  $1e^{-6}$ , the objective function will be scaled by  $1e^{-6}$ .

This formulation is similar to that of compromise programming discussed in the literature survey, except that the scaling is done by using only the target values instead of the error between the worst response and target values, or:

$$M_i = \frac{1}{R_{i(\text{worst})} - T_i}$$

### 5.3.1 Fourth strut model

With the numerical model set up and the objective function defined, the parameters that the optimiser could use as design variables needed to be defined. For a first attempt, only sizing parameters were used. Sizing parameters in structural optimisation are the parameters that describe an element's geometrical properties, such as the dimensions of the cross-sections. Although one can also make changes directly to other property parameters, such as the moments of inertia for example, these changes would be direct method changes, which could result in the physical significance of the element's properties becoming lost. Therefore only the dimensions of the cross-sections were chosen as design variables for this initial attempt. The possible dimensions are listed below, along with their abbreviations, by which they will be known from here on:

- Hollow bar outer diameter (HB\_OD)
- Hollow bar wall thickness (HB\_WT)
- End cap diameter (EC\_D)
- Threaded rod diameter (TR\_D)

- Nut diameter (Nut\_D)

Each of these design variables was set to be changed independently of the others. This means that the diameter of the end cap section is not restricted to being the same as the outer diameter of the hollow bar, for instance. Although this is not accurate of the physical model, it was done to provide the optimiser with more freedom to make changes in this specific area of modelling uncertainty. Since the exact behaviour of the end caps is not completely understood, this design variable selection could aid in understanding what the effective structural contribution of the end cap could be. Similarly, other dimensional design variables were not restricted in any way. Other than providing the optimiser with more freedom, the optimiser's resultant changes could provide more information on which areas of the strut had insufficient or incorrect modelling detail.

The results of this optimisation are shown in Table 5.4. As expected, these results show that the optimiser attempted to reduce all the errors simultaneously because of the objective function definition. Although some errors remained almost unchanged, like the axial response error, the balance of the errors were reduced significantly. Compared to the previous model, the maximum static response error was reduced to -1.4% from almost 20%, and the maximum dynamic error was reduced to -2.62%, also from almost 20%.

Although these results could be deemed acceptable, meaning that these strut models can be used further to model the assembled structure, it is necessary to also investigate what changes the optimiser made to the set of design variables. Although it was expected that the optimiser could make larger changes to the design variables of the element properties of the end caps, there were also large changes in the dimensions of the hollow bar. The largest change, of over 50%, was made to the wall thickness of the hollow bar. This change combined with the fact that the largest response error was that of a dynamic response, led to the reinvestigation of all parameters that influence the model's dynamic behaviour.

### 5.3.2 Fifth strut model

Considering the results of the previous model it was decided to add another design variable to change the mass of the concentrated mass elements used to model the accelerometers. This was labelled *AM*. A change in these mass values was justified by the possibility that the cables connecting to the accelerometers have a significant effect on the effective mass.

It was expected that, by providing the optimiser with this additional design variable, which has no effect on the strut's static behaviour, the optimiser would be able to change the strut's dynamic behaviour independent from the static behaviour.

Table 5.4: Summary of the results of the fourth strut model

Objective response		Target	Current	Error [%]
Axial	$[\mu m]$	9.83	9.97	-1.40
Bend: Rods	$[\mu m]$	627.00	630.47	-0.55
Bend: Hollow bar	$[\mu m]$	163.00	162.10	0.55
Bend: End caps	$[\mu m]$	349.00	348.01	0.28
Frequency 1	$[Hz]$	290.9	289.6	0.46
Frequency 2	$[Hz]$	530.9	544.8	-2.62
Frequency 3	$[Hz]$	701.6	688.3	1.89
Design variable		Initial	Current	Change [%]
HB_ID	$[mm]$	25.00	17.63	29.49
HB_WT	$[mm]$	7.50	11.45	-52.60
EC_D	$[mm]$	40.00	39.11	2.23
Nut_D	$[mm]$	16.00	18.98	-18.63
TR_D	$[mm]$	9.60	8.27	13.91

As shown by the results in Table 5.5, the optimiser was able to make further improvements to the response errors and the objective function value was reduced to  $3.32 \times 10^{-4}$  from  $1.32 \times 10^{-3}$  for the previous model. This model's dynamic behaviour is more accurate than the previous one, but there is little improvement in its static response errors. These results still came with large changes in the design variables, with the largest still being the hollow bar wall thickness at over 46%. Contrary to what was expected, the addition of the extra design variable did not result in significant reductions in the changes made to the other design variables, other than to the effective diameter of the nuts.

Until now only sizing design variables have been used. It was decided to add shape change design variables as a next step, since these are easy to implement and will provide the optimiser with even more freedom.

### 5.3.3 Sixth strut model

Shape changes allow the optimiser to change the size and shape of elements by making changes to the positions of their nodes, as discussed in detail in the literature survey. For this model, the shape change domains were defined as shown in Figure 5.6.

In the figure the different domains are labelled 'D1' to 'D4' and the perturbations are labelled 'L', with the subscripts 'nut' and 'EC' for the strut-side nut and hollow bar lengths respectively:

Table 5.5: Summary of the results of the fifth strut model

Objective response		Target	Current	Error [%]
Axial	$[\mu m]$	9.83	9.94	-1.15
Bend: Rods	$[\mu m]$	627.00	624.26	0.44
Bend: Hollow bar	$[\mu m]$	163.00	162.99	0.00
Bend: End caps	$[\mu m]$	349.00	349.83	-0.24
Frequency 1	$[Hz]$	290.9	291.9	-0.34
Frequency 2	$[Hz]$	530.9	532.0	-0.21
Frequency 3	$[Hz]$	701.6	710.5	-1.26
Design variable		Initial	Current	Change [%]
HB_ID	$[mm]$	25.00	18.58	25.68
HB_WT	$[mm]$	7.50	10.99	-46.51
EC_D	$[mm]$	40.00	38.76	3.10
Nut_D	$[mm]$	16.00	15.95	0.32
TR_D	$[mm]$	9.60	8.58 <td 10.61	
AM	$[g]$	5.00	5.75	-43.78

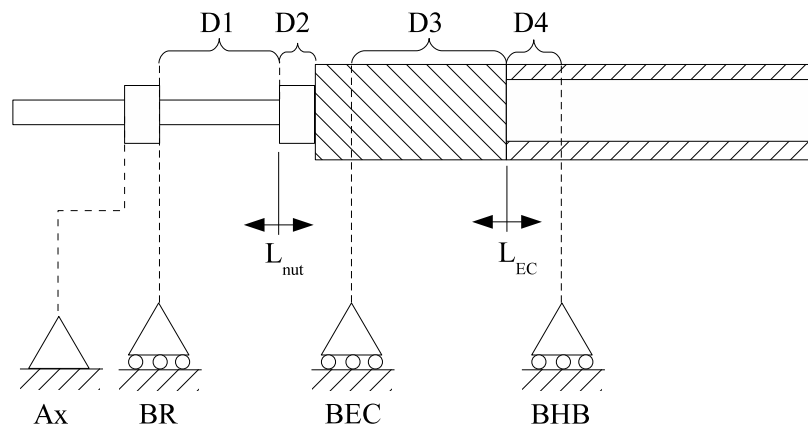


Figure 5.6: Shape change domains and perturbations

- Domains 1 and 2 are both perturbed by  $L_{nut}$ . This allows for the thickness of the nut to be changed. Two domains had to be defined since a change in the length of the nut's elements will have an effect on the lengths of the threaded rod elements adjacent to it.
- Domains 3 and 4 are perturbed by  $L_{EC}$  so that the length of the end

caps can be changed. Two domains were defined for the same reason as mentioned above.

The domains were defined in such a manner that the nodes on which the boundary conditions were applied were not moved, so that the original boundary conditions, for which the target responses had been set, were preserved.

The results in Table 5.6 show that the addition of these design variables allowed the optimiser to match the static behaviour better, with the largest error reduced to only 0.5% from 1.15%. The changes in most of the design variables were also considerably less than in the previous model. However, for the dynamic load cases the maximum error had become worse and the change in the accelerometer mass was over 80%, which is almost double that of the previous model.

This indicates that the addition of shape change design allowed the optimiser to better match the strut's static behaviour, but it still struggled to find an optimum that satisfied the dynamic behaviour as well. Although the static behaviour improved, the relatively large error in the dynamic response resulted in the objective function value worsening from the previous  $3.32 \times 10^{-4}$  to  $1.03 \times 10^{-3}$ . This value is similar to that of the fourth model, which did not have the mass of the accelerometers as a design variable. It also illustrates the fact that there potentially are multiple solutions and that the technique should be used with care taking into account both the accuracy obtained as well as the changes to the design variables. It is important to use engineering judgment to explore the problem further and end up with a realistic solution.

Until this stage care had been taken to try to make the allowable changes possible to the model independent of each other whilst still maintaining the physical significance of the changes. There was, however, one modelling change that could be made to grant the optimiser even more freedom. Again, because of the uncertainty of the behaviour of the end cap, this area was the focus for trying to provide more freedom and the details of this next step are covered in the next subsection.

### 5.3.4 Seventh strut model

The current model has a single property set for the end caps with a circular cross-section. The model is also set up so that a change in length of the end caps, which means a change in stiffness, results in a change in length of the hollow bar. A method to decouple the lengths of the solid bar and those of the end caps was introduced by connecting elements in parallel, thus sharing nodes on their edges, to the elements of the end caps, as shown in Figure 5.7. With this change, one set of the parallel elements can be assigned to the hollow bar property set and the other set of elements can be assigned to the circular cross-section property set of the end caps.

Table 5.6: Summary of the results of the sixth strut model

Objective response		Target	Current	Error [%]
Axial	$[\mu m]$	9.83	9.79	0.44
Bend: Rods	$[\mu m]$	627.00	630.05	-0.49
Bend: Hollow bar	$[\mu m]$	163.00	163.40	-0.24
Bend: End caps	$[\mu m]$	349.00	350.29	-0.37
Frequency 1	$[Hz]$	290.9	299.8	-3.07
Frequency 2	$[Hz]$	530.9	529.4	0.28
Frequency 3	$[Hz]$	701.6	704.1	-0.36
Design variable		Initial	Current	Change [%]
HB_ID	$[mm]$	25.00	22.64	9.42
HB_WT	$[mm]$	7.50	9.22	-22.98
EC_D	$[mm]$	40.00	36.70	8.25
Nut_D	$[mm]$	16.00	16.49	-3.06
TR_D	$[g]$	9.60	9.64	-0.38
AM	$[mm]$	5.00	7.32	-83.06

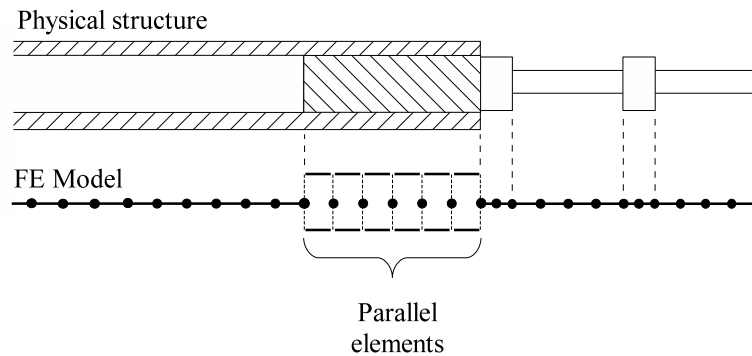


Figure 5.7: Adding parallel elements to the end caps

This meant that the diameter of the end cap cross-section had to be set to the same as the inner diameter of the hollow bar to keep the cross-sectional area the same as before the parallel elements were introduced. However, the optimiser was not constrained to keep the end cap diameter equal to the hollow bar inner diameter. This granted the optimiser the freedom to add more area and inertia to the end cap sections than would have been possible by a single cross-section. Although this is not physically accurate, this method can provide a means to model the effective properties of the end caps.



The results of this model are shown in Table 5.7 and indicate that the optimiser was able to find a solution to address both the static and dynamic errors of the model, reducing all errors, both static and dynamic, to below 0.8%. The objective function value was also reduced to only  $8.34 \times 10^{-8}$ , which is considerably less than the previous minimum of  $3.32 \times 10^{-4}$ . However, these results were achieved by still making big changes to some of the design variables, especially the accelerometer mass. The change in the hollow bar wall thickness is also relatively large, at over 24%.

Table 5.7: Summary of the results of the seventh strut model

Objective response		Target	Current	Error [%]
Axial	$[\mu m]$	9.83	9.84	-0.10
Bend: Rods	$[\mu m]$	627.00	625.03	0.31
Bend: Hollow bar	$[\mu m]$	163.00	162.98	0.01
Bend: End caps	$[\mu m]$	349.00	349.24	-0.07
Frequency 1	$[Hz]$	290.9	288.7	0.76
Frequency 2	$[Hz]$	530.9	531.9	-0.20
Frequency 3	$[Hz]$	701.6	699.4	0.31
Design variable		Initial	Current	Change [%]
HB_ID	$[mm]$	25.00	22.47	10.13
HB_WT	$[mm]$	7.50	9.31	-24.11
EC_D	$[mm]$	40.00	24.81	0.75
Nut_D	$[mm]$	16.00	18.90	-18.09
TR_D	$[mm]$	9.60	8.96	6.71
AM	$[g]$	5.00	6.93	-73.23

It was also noted, that for all the models so far, the changes in the hollow bar's inner diameter and wall thickness still resulted in an outer diameter of between 40.5 mm and 41.1 mm, which is less than a 3% change. By calculating the cross-sectional area and moment of inertia of the hollow bar, these values showed that the resultant change in the moment of inertia remained almost unchanged at roughly 19.5%, as shown in Figure 5.8. Considering that the bending of the hollow bar load case isolates all other effects, it was concluded that the resultant changes in the design variables were necessary to provide an accurate model of the hollow bar section, and thus the large change in the wall thickness was deemed acceptable.

The results show that there was a significant decrease in the change of the cross-sectional area of the resultant model's hollow bar sections, when

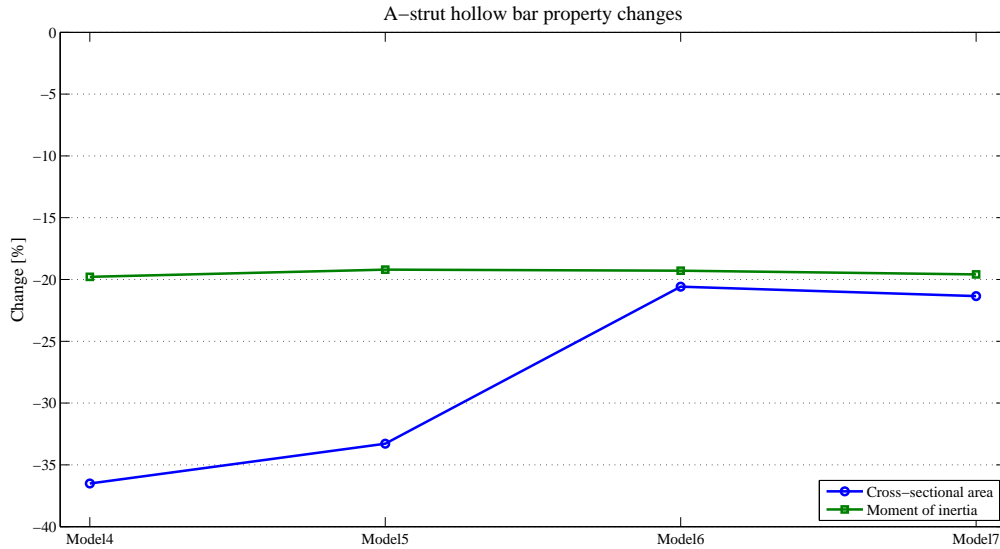


Figure 5.8: Change in hollow bar properties

the shape change design variables were added. Despite this decrease in cross-sectional area, the axial response error improved. This shows that, with the new freedom, the optimiser was able to achieve the correct axial stiffness of the strut by adding stiffness elsewhere, and was not forced to increase the axial stiffness of the hollow bar. The hollow bar cross-sectional area remained unchanged for this model, but the addition of the parallel elements allowed the optimiser to refine the parameters to accurately model the end caps.

Because the static behaviour of the struts is of more importance for this project, no further investigation was done into the large change in the accelerometer mass. However, it was important to add the dynamic data to the objectives and the change in the accelerometer mass allowed the optimiser to improve the overall results. Therefore, although the excessive change in the accelerometer mass cannot be justified physically, it was left as is for the purposes of this problem.

Therefore this modelling setup was accepted as the setup that would be used to continue with the rest of the project.

### 5.3.5 Summary of strut models

The purpose of this subsection is to provide an overview of the results of all the different models, as well as to add some additional observations. For clarity, a summary of the changes made to the different models is shown below:

**Model 1** Simple model with only hollow bar and threaded rods modelled

**Model 2** Model 1 with end cap detail

**Model 3** Model 2 with nuts detail (best FE model)

**Model 4** Model 3 set up with sizing design variables

**Model 5** Model 4 with accelerometer added as design variable

**Model 6** Model 5 with added shape change design variables

**Model 7** Model 6 with parallel elements over end caps (best overall model)

The graph in Figure 5.9 shows the error percentage of all the responses for the different strut models. The values of the responses are available in Appendix A.1. This graph shows the significant improvement from the normal FE Model 3, to the first optimisation Model 4. Although the improvements from model 4 onwards are small, it must be borne in mind that the changes in design variables also had to be considered.

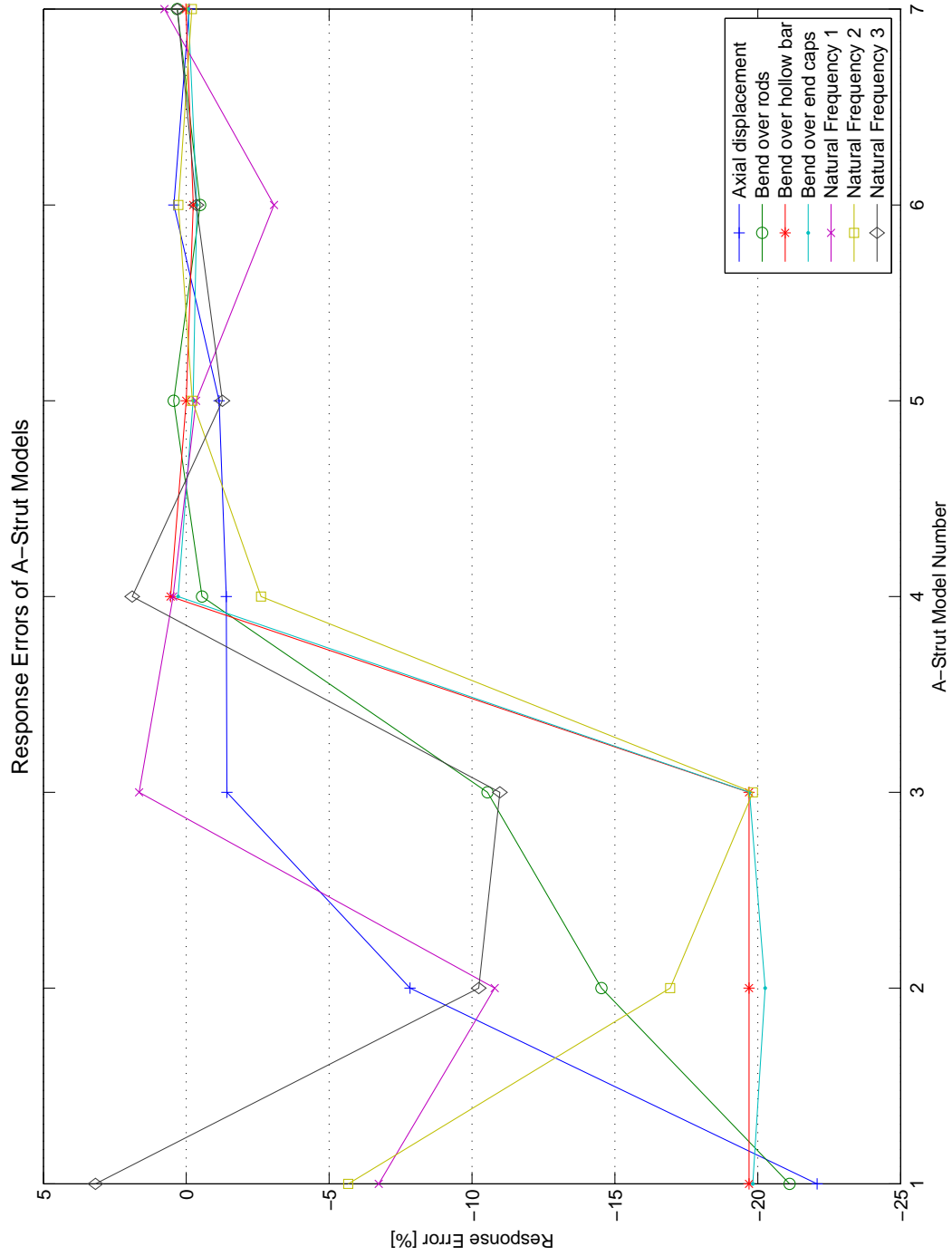


Figure 5.9: Errors for different strut models

The graph in Figure 5.10 shows the percentage changes made to the design variables for the optimisation models. From this graph it is clear that, apart from the accelerometer mass, model 7 required the smallest total changes to the design variables. Although the changes in model 6 are similar to those of model 7, except for the change in the nut length, the former model's first natural frequency error is much larger than that of model 7.

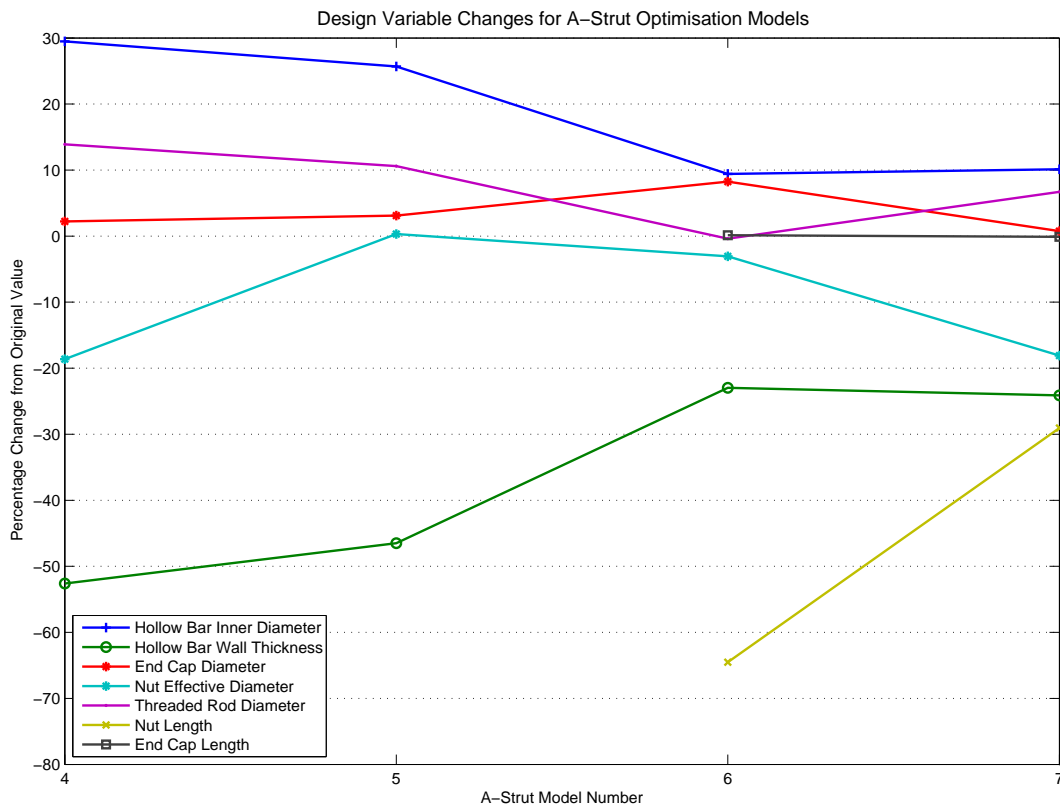


Figure 5.10: Design variable changes for different strut models

### 5.3.6 Additional observations

It should be noted that the initial models during the project did not include the modelling of the accelerometer masses. Without this detail the optimiser was unable to find results that were acceptable, since the second natural frequency error remained large. Because of this big error, the optimiser was forced to make changes to try to reduce this dynamic error and, consequently, all the other errors become worse.

As mentioned in the previous chapter, the modelling phase revealed that there was an error in the first set of axial objective values obtained during

testing. As with the accelerometer mass, this incorrect axial objective also led to a big error that the optimiser had difficulty reducing. After multiple attempts and modelling changes, it was noticed that, although most of the other objective errors were reduced with each new modelling setup, the axial error remained large. When the axial objective's weight in the objective function was set to zero, thus removing this response objective, it was found that all the other responses' errors were reduced and the resulting axial response was  $11.1 \mu m$  for the axial load case. This is what led to the reinvestigation of the test results for the axial load case that yielded the correct axial objective of  $9.83 \mu m$ . This shows that, if optimisation is used correctly, one can identify possible errors by first criticising the results.

For this phase the values of the objectives used for each strut type were the mean of the measured values of all the measured struts of that type. However, as shown in the previous chapter, there still was a significant scatter in the measured data of each strut type. Ideally, more specimens should be used to get a better indication of the general behaviour of a strut-type group so that the variability in these struts can be addressed more accurately.

## 5.4 Data-matching Results for the Remaining Strut Types

Until this point attention was only given to the modelling of the A-struts in order to first finalise the methods. This section covers the results of the data matching of the remaining struts.

For comparative purposes, two variants of each strut will be investigated. The first is the setup used for model 3, the best model before any optimisation. The second variant is the result of the optimised setup used in model 7, but with the parallel elements removed. When these new strut models are used to build the model for the assembled laboratory structure, these parallel elements will be replaced by single, theoretically equivalent elements. This was deemed necessary after it was noted that the use of parallel elements in numerical modelling is cumbersome and that errors are likely to occur. The reason for this is that it is visually difficult to distinguish between the elements that share the same nodes, which can result in incorrect properties being assigned to some elements. Models with parallel elements were also found to be prone to element connectivity errors.

The modelling process for each strut type starts by creating the first modelling variant. These detailed FE models are then labelled  $x$  Model3, where  $x$  is the strut type A, B, C or D. The number corresponds to the number of the setup used in the previous section.

The second variant for each type is then created using the optimisation problem setup of model 7 and applying it to the models for each strut type.

Each strut type is then individually optimised with its own set of response objectives. With the optimised parameters, the new dimensions of the cross-sections of the parallel elements are available. These are used to determine the properties of the elements that will replace the parallel elements. The properties include the moments of inertia about axis one and two, the polar moment of inertia, the cross-sectional area and the area factors for shear. Since the elements share the same neutral axis, the moments and polar moments of inertia, as well as the cross-sectional areas of each of the two parallel element properties can simply be added to obtain their effective values for the single element properties. The parallel elements are then replaced and these models are labelled *x* Model7 to indicate that they are the final strut models that will be used.

Figure 5.11 on page 60 shows the results of each of the two variants of models for each of the four strut types. The results are provided as the absolute error percentages, and the values of the responses are available in Appendix A.2. This graph shows that, after the optimisation had been applied to the different strut types, all errors for all the struts were reduced to below 5%. Note that the same optimisation setup was used on all the strut types, but that the models were changed to the lengths of the respective struts.

The results proved to be satisfactory for all the strut types and therefore these strut models with the parallel elements replaced by single, equivalent elements were ready to be implemented into the modelling of the complete structure. The project could therefore continue to the next phase, which was to test and model the two variants of the complete structure.

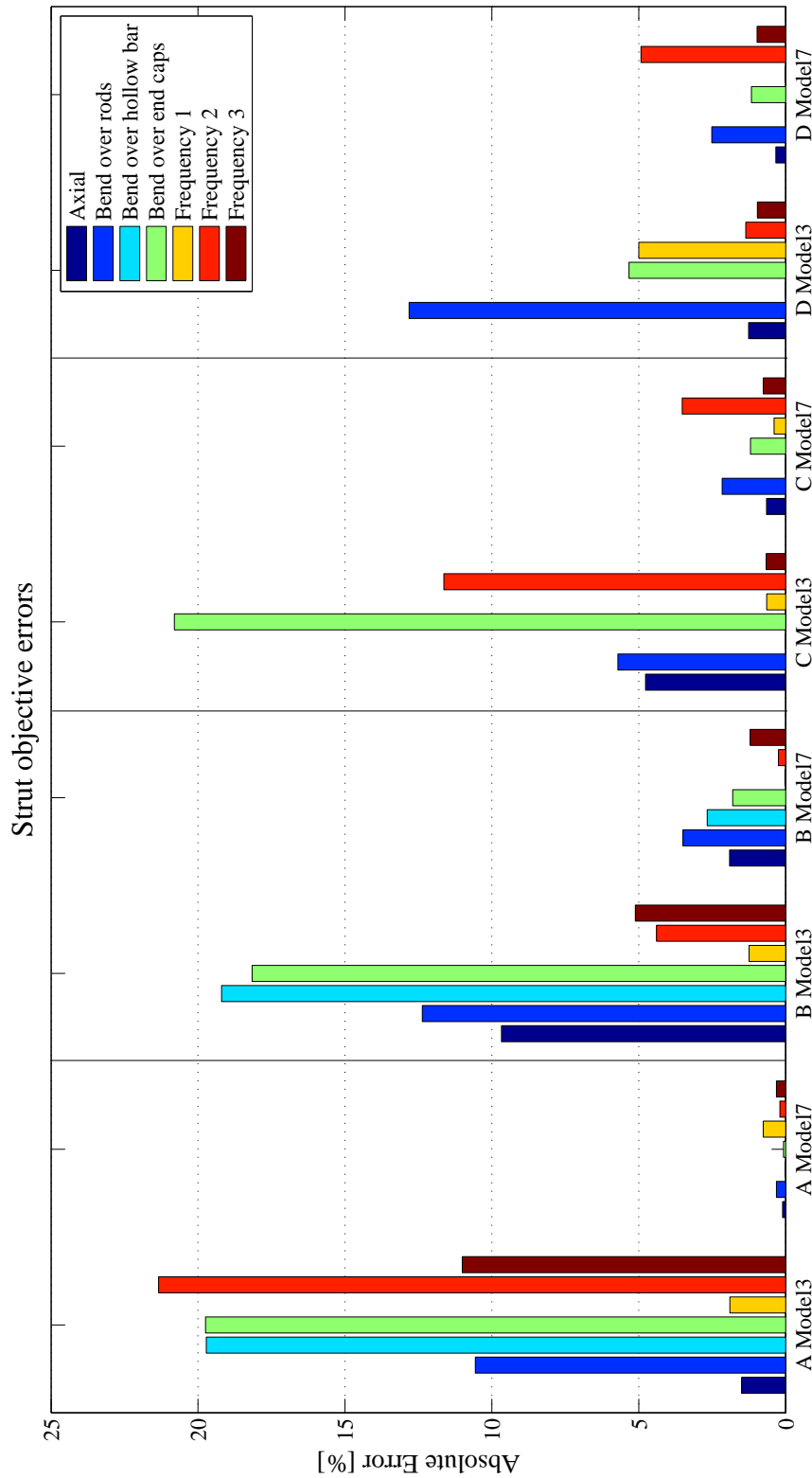


Figure 5.11: Objective errors for all final strut models



## Chapter 6

# Testing and Modelling of the Assembled Structure

This chapter covers the testing procedures and modelling steps of both the four- and five-node assembled laboratory structure variants. Testing and modelling started on the simpler four-node structure so that possible testing difficulties, such as the application of the boundary conditions, could be identified easier. Once there was confidence in the test procedures, the process moved on to the five-node structure. With the test results available, the modelling phase was carried out in order to compare the results, which is done at the end of this chapter.

### 6.1 Structure Testing

Returning to the first step of the flowchart in figure 3.7 on page 21, it was necessary to identify the measurable responses. For the purposes of SALT's mirror support truss, the displacements are the most important measurable outcome, particularly the displacements of the top layer of nodes to which the mirrors are attached. By this reasoning, the displacement of the top node was a crucial response to measure. Other responses could also be measured and in the case of the five-node structure, the displacement of the centre node could also be used. Other measurable responses used were the displacements of the foot nodes. Preliminary numerical models indicated that the maximum expected displacement would be in the order of 20 to 50  $\mu m$  for a 10 kN load. Therefore the LVDT used until this point would be sufficient in terms of its resolution. Unfortunately only one such LVDT with a small enough resolution was available and the testing required measuring up to five points. The solution to this problem was to move the LVDT from point to point during testing once a repeatable testing setup had been obtained.

Figure 6.1 shows the final setup that provided the best results. Shown in the picture is the four-node variant of the structure, the load frame, the

measurement pedestal and the power pack that was used to actuate the jack. However, before this setup could be finalised, some complications needed to be addressed, the details of which will now be discussed.

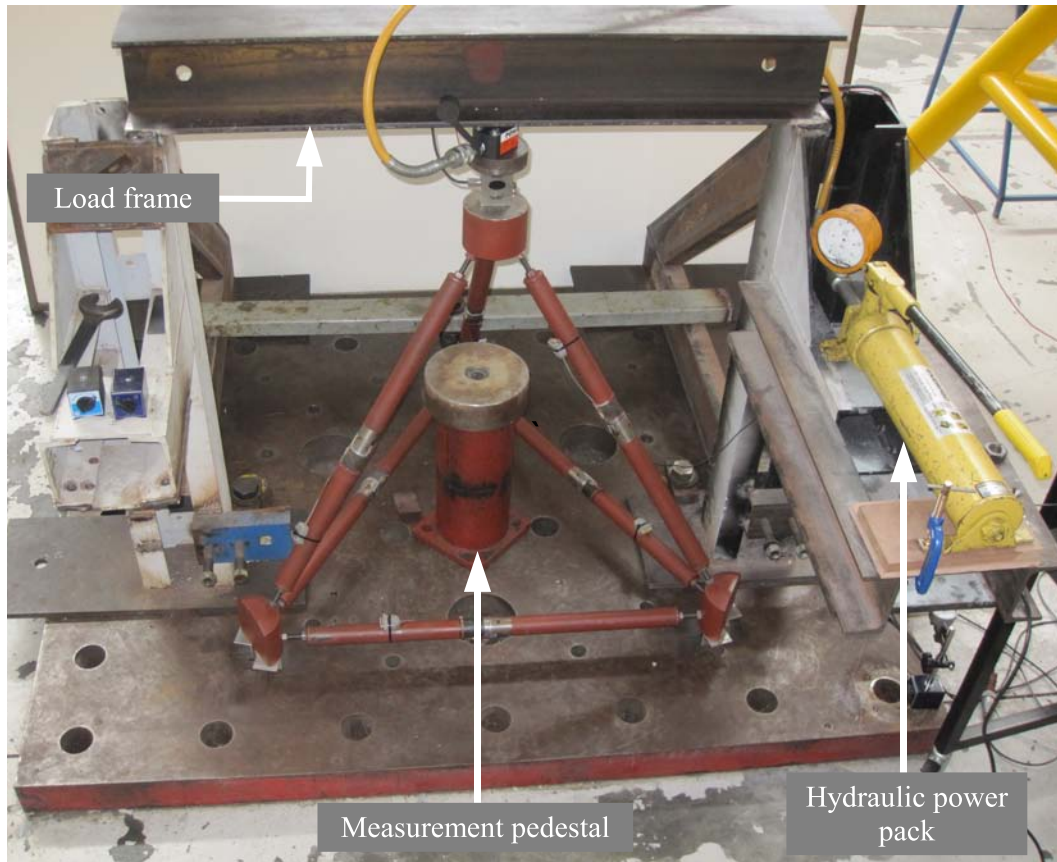


Figure 6.1: Final test setup of the assembled structure

### 6.1.1 Supporting boundary conditions

The two simplest choices for supporting a structure are to either completely fix the foot nodes or to fix only certain degrees of freedom. Fixed boundary conditions effectively remove the need for the A-struts, simplifying the four-node, six-strut structure to a three-strut structure. Modelling fixed boundary conditions is also simple and therefore fixed boundary conditions were a good point to start from.

In the initial setup, a concrete floor allowed for angle irons to be bolted down securely to try to provide the fixed boundary conditions, as shown in Figure 6.2a. However, during the first set of tests, measurements on the foot nodes showed that there was still movement on the foot nodes. After careful

consideration it was concluded that it would in fact be more difficult to obtain completely rigid physical boundary conditions. It was thus decided to abandon trying to obtain fixed boundary conditions and rather to pursue conditions that were both easy to model and to mimic for the tests.

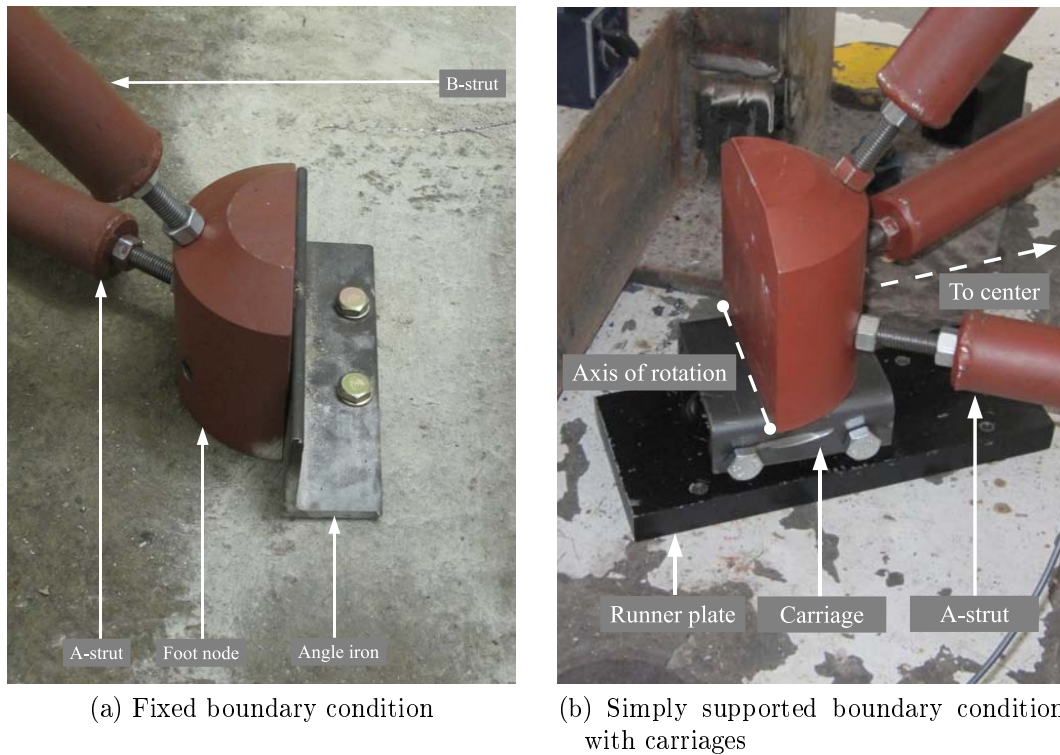


Figure 6.2: Failed physical boundary conditions

An initial FE model showed that the foot nodes would translate outward from the centre. To allow this, carriages were designed and manufactured for the foot nodes to rest on, as shown in Figure 6.2b. The carriages each had four bearings that acted as wheels and that were chosen so that the maximum load they would experience was less than 10% of their maximum acceptable static load. This was to ensure that as little friction as possible would result. The carriages were placed on 20 mm thick steel "runner plates". These plates provided a smooth, flat surface for the carriages to run on and each plate was supported on three points to eliminate wobbling. Tests run during this setup yielded unexplainable non-linear results for the displacement of the top node. On finer inspection it was observed that the foot nodes rotated outwards around the axis of rotation, as shown in Figure 6.2b. This was not predicted by the initial FE model, since this model only modelled the struts and where they connected at the nodes. In reality, the point where the strut centre lines pass

through is 35 mm above the foot node's bottom surface. Because of this offset in the supporting boundary condition, a moment was applied that resulted in the rotation of the foot nodes. Since the carriages were designed to allow only for translation, placing the foot nodes on the flat surface of the carriage caused a non-linear boundary condition to be imposed as soon as the foot nodes rotated. In an initial attempt to address the rotational degrees of freedom on the foot nodes, a disc with a diameter of 10 mm and a thickness of 10 mm was placed underneath the foot nodes on the carriages. Test results from this setup showed an improvement, but the results were still not acceptable.

Realising that the carriages and discs were not ideal boundary conditions and thus the most probable cause of the poor results, other methods of applying the boundary conditions were investigated. One of the proposed methods was to place the foot nodes on hardened steel balls. This means that the foot nodes are free to move and rotate in all degrees of freedom other than vertical displacement.

By using one 100 mm thick steel plate big enough to support the whole structure, instead of the three runner plates, one 44.45 mm (1.75 inch) diameter steel bearing ball was placed underneath each foot node, as shown in Figure 6.3a. To accurately control the position of the bearings under the foot nodes, aluminium angle profile sections of 40 x 40 x 1.6 mm were bolted to the foot nodes as shown in Figure 6.3b. The sections were fitted at a 90 degree angle so that the bearings could be cornered into them, locating their position. A thin aluminium profile was chosen because it provides little additional stiffness in the event that it should restrict movement.

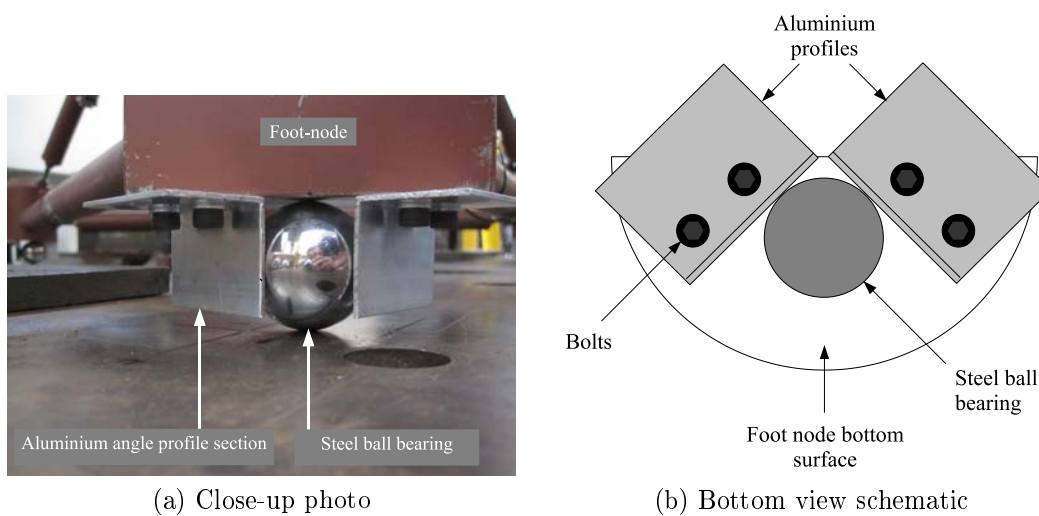


Figure 6.3: Final supporting boundary condition setup

### 6.1.2 Loading boundary condition

To load the structure without transferring unwanted moments, it was important to align the point where the structure was loaded on the top node and the point where the reaction force was applied. A 400 mm hydraulic cylinder was used with an initial setup, but it proved to be difficult to align. Tolerance in the connections between the hydraulic cylinder and where it was fitted to the top node also resulted in poor data because of misalignment and buckling. Taking these problems into account, a low-profile hydraulic jack was an ideal solution to address the alignment problem. Because of the low 45 mm profile height of the jack, the point where the reaction force was applied could be kept close to the top node, thus making alignment easier but also reducing the effect if there was a misalignment. It is with the use of this jack that the load frame shown in Figure 6.1 was built. The load frame was built from I-beams that were welded together and could be bolted down over the test structure to the 100 mm thick steel plate. The stiffness of the load frame was not a critical issue because the surface on which the structure was placed would serve as the datum for measurements. The load frame only had to be stiff enough not to deflect enough to cause misalignment.

With the load frame in place, the setup shown in Figure 6.4a was used. First the load cell was bolted to the center of the top node. Then an adapter was made to ensure that the load cell centre line was in line with the centre line of the jack's cylinder. By bolting these three components to each other, tolerance was eliminated and alignment was ensured. The solid steel spacer shown at the top of Figure 6.4a was clamped to the load frame. As shown in Figure 6.4, the jack's cylinder had a rounded tip as opposed to a flat tip. This proved to be ideal to avoid unwanted moments being induced because of contact surfaces possibly not being parallel.

### 6.1.3 Testing

An FE model that was updated with the new boundary condition showed that the rotations of the foot nodes were more severe than initially expected. This meant that the translation of the foot nodes could not be measured without measuring effects due to rotation. Because of this it was decided to rather find a means to reliably measure both effects simultaneously. To amplify the effects of rotation, the LVDT would have to be placed as far away from the foot node's point of rotation as practically possible so that the rotation could be measured more accurately. With the point of rotation being the point of contact with the steel ball, the LVDT was placed close to the top surface of the foot node. The LVDT was placed horizontally, with its axis pointing to the structure's centre. This meant that, during loading, the foot node's translation would be measured, along with the translational effects due to rotation, in the horizontal plane only. This could be modelled accurately by

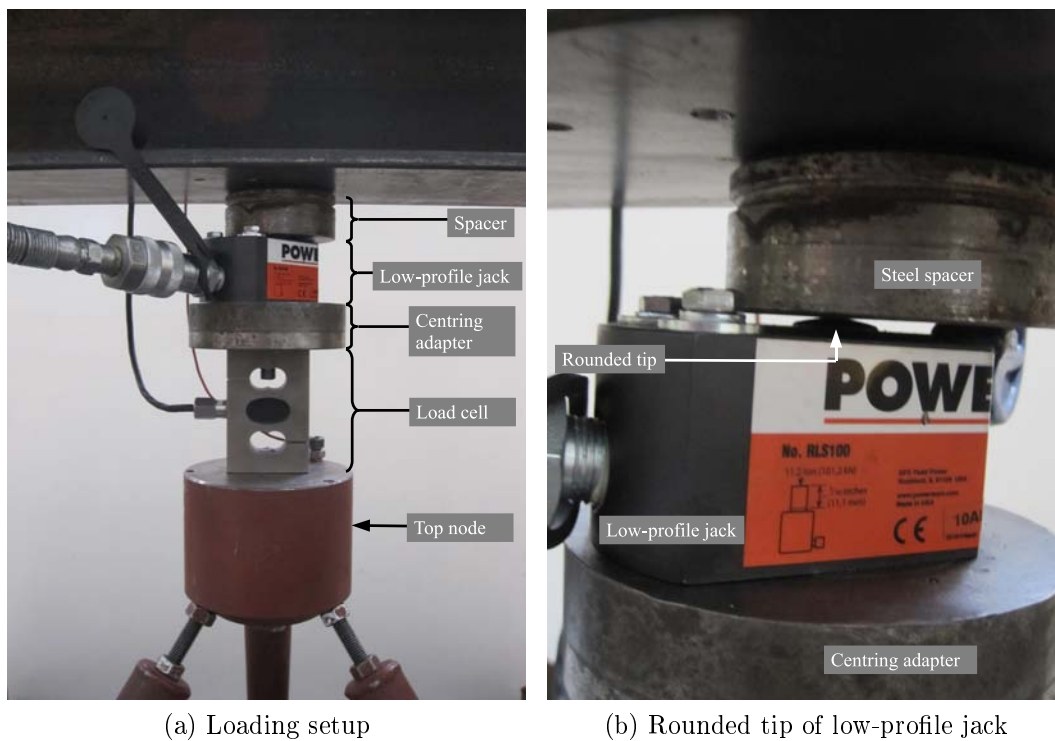


Figure 6.4: Detail of loading boundary condition

creating local coordinate systems that also have their x-axis pointing to the structure's centre and have a horizontal x-y plane. More detail about these coordinate systems will be discussed in the next subsection, on the modelling.

To compensate for possible misalignment of the LVDT during testing, the LVDT was calibrated before each test by taking a zero reading whilst the tip touched the surface, then inserting a 5 mm calibration block between the tip and the surface, as shown in Figure 6.5, and then taking a reading again. With these two readings and knowing that they represent 5 mm, the LVDT was calibrated for each specific point of measurement. This was necessary since only one LVDT with a resolution high enough for these tests was available, and it thus had to be moved from point to point during testing.

The vertical displacement of the top node was measured from below the node. A pedestal as shown in Figure 6.1 was used to get a stable platform to which to fix the LVDT as close to the top node as practically possible. This was found to be important because otherwise there was too much lateral movement of the LVDT and the results consequently were poor.

Before testing commenced, care was taken to calibrate the structure's geometry to the dimensions it was designed to be. Once the node-to-node and threaded rod lengths were correct, the locking nuts were tightened and the geometry was set.



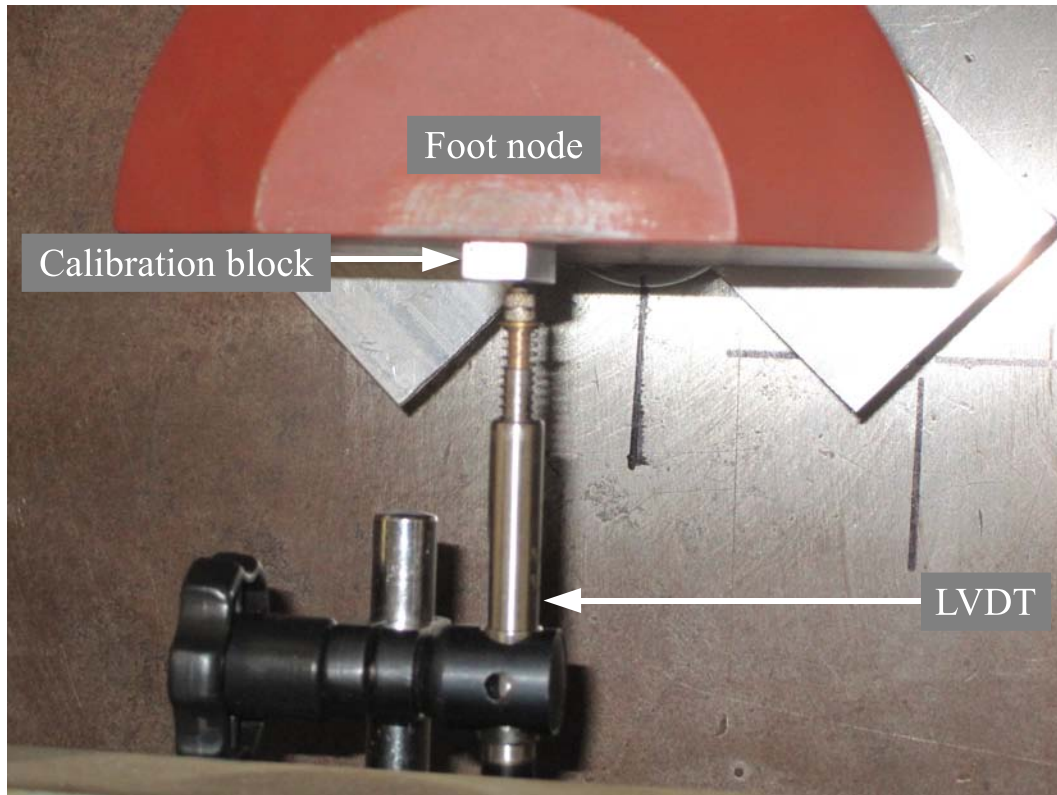


Figure 6.5: Method of calibrating the LVDT on a foot node

Similar to the bending tests in the previous chapter, seating complications were avoided by keeping the structure loaded once testing started. The maximum load was always kept below the yielding load, which was determined using the preliminary FE model. The hydraulic jack was connected to a manual hydraulic power pack. It was found important to apply a load cycle with one continuous stroke of the power pack's lever so that small, interim hysteresis loops would not be measured.

Having gone through multiple iterations of test setups, it became apparent that the testing of this structure was a daunting task. However, with the boundary conditions applied as described and making sure that there was as little tolerance in the system as possible, reasonable results could be obtained. These results were deemed accurate enough for a linear fit to be made, thus concluding the testing of the four-node structure.

The structure was then removed from the setup so that the central node could be fitted and the struts lengths calibrated, after which the structure was returned to the test setup. As discussed earlier, it was decided to measure the displacement of the central node for this structure variant as well. This was done in a similar fashion as for the top node by using a pedestal fixed to the base steel plate and by placing the tip of the LVDT on the bottom face of the

central node, thus measuring the downward displacement of the node.

Note that the final results of these tests are discussed later in this chapter when they are compared to the numerical results.

## 6.2 Structure Modelling

In this section, the points where the struts connect are called "nodes", and the name "node points" is used to refer to the nodes of elements in FE models.

The modelling of the four- and five-node structures started with placing the node points where the struts intersect, as per the structure's design, which points are indicated by **TN**, **CN** and **FN1/2/3** in Figure 6.6a. The nodes were modelled to be completely rigid, and therefore rigid body elements (RBEs) were used to model the offsets from the node points to where the struts connected to the node. As mentioned before, the actual supporting point of the steel ball was on the bottom surface of the foot node, which was also offset from the nodepoint. The point where the LVDT was placed was also offset from the nodepoint. These offsets were modelled with RBEs and were set up in such a manner that no relative motions were possible between these RBEs. Figure 6.6b shows how all these RBEs are orientated and also shows the outline of the physical parts with dotted lines. Note that, although only one line is shown for the A-strut connections, there actually were two RBEs in the same plane for the two A-strut connections.

As discussed in the previous section, a local coordinate system was defined at each foot node. The origin of the coordinate system was placed at the strut intersection node point. The x-axis of the coordinate system points to the structure's centre along the radial lines shown in Figure 6.6a, and the z-axis is parallel to the z-axis of the global coordinate system, as also shown in Figure 6.6a. The node points of the foot nodes were all defined in the global coordinate system, but the output of the intersection and measurement node points was set to be in their respective local coordinate systems. This allowed for total translation, as would be measured by the LVDT, to be obtained from the FE model by taking the value of the translation of the measurement node point in the x-direction of the local coordinate systems of the foot nodes.

For the boundary conditions the vertical translation ( $T_z$ ) was fixed for the three supporting node points. The remaining degrees of freedom ( $T_x$ ,  $T_y$  and  $R_z$ ) were fixed at the top node to prohibit free-body modes.

With this setup the strut models could be inserted between the RBE node points of the different nodes. This made it possible to use the same model to compare the structure's response for the different strut models by simply replacing the struts in the model. Also, for the four-node structure model the central node and connecting struts were simply removed.



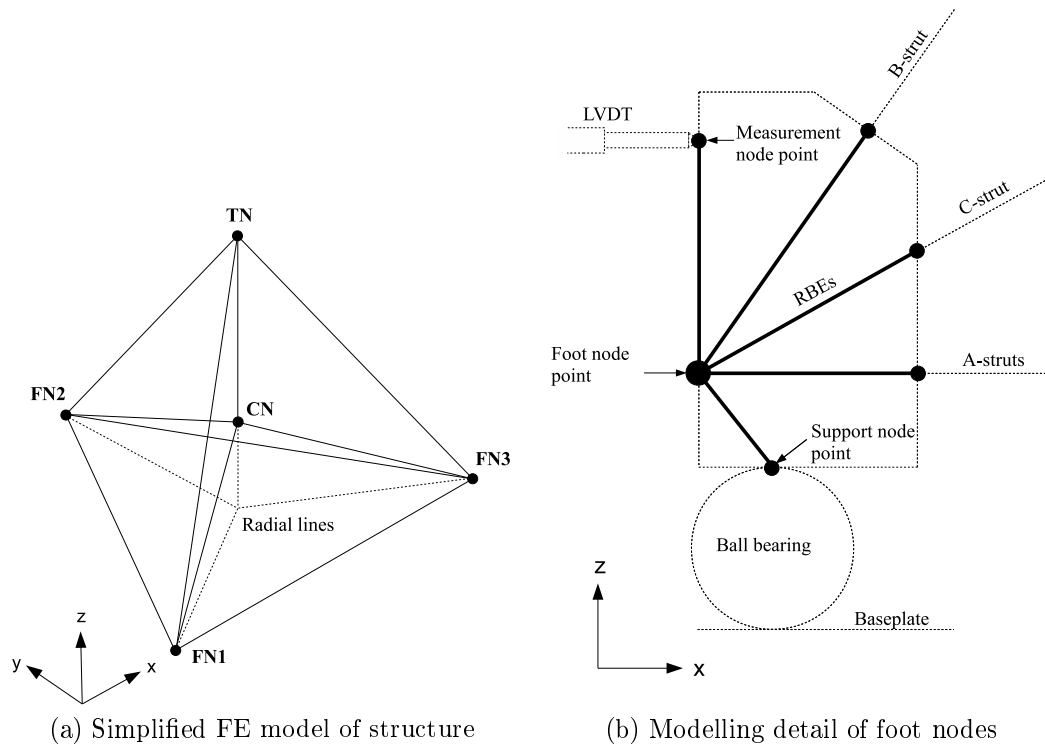


Figure 6.6: Modelling of the complete structure

### 6.3 Comparison of Results

With the various strut models available, three were selected from which the structure models would be modelled. The first structure model, **Structure 1**, was modelled using the initial strut models, like those used during the development of the mirror support truss model. These strut models were labelled Model 1 in the previous chapter and had only two property groups; one for the hollow bar and one for the threaded rods.

The second structure model, **Structure 3**, was modelled with the more detailed, pre-optimisation strut models labelled Model 3 in the previous chapter. This strut model included the detail of the end caps and the nuts.

The third structure model, **Structure 7**, was modelled with the optimised strut models previously labelled Model 7. These were deemed the best struts models obtainable.

These assembled models did not undergo any optimisation. They were modelled with the respective struts and their responses were recorded. Therefore these three models served as validation of the accuracy of the respective types of strut models. Shown in Table 6.1 are the measured compliances obtained during testing, and the compliances predicted by the respective nu-

Table 6.1: Modelling and testing results and errors

	TN	CN	FN1	FN2	FN3
	$[\mu m/kN]$	$[\mu m/kN]$	$[\mu m/kN]$	$[\mu m/kN]$	$[\mu m/kN]$
<b>Four-node</b>					
Measured	25.1	-	48.5	60.5	71.3
Structure 1	37.6	-	123.2	83.0	119.2
Error	-49.6%	-	-154.0%	-37.1%	-67.2%
Structure 3	29.5	-	96.6	65.1	93.4
Error	-17.5%	-	-99.1%	-7.5%	-31.1%
Structure 7	22.9	-	72.3	48.7	69.9
Error	9.0%	-	-49.0%	19.5%	1.9%
<b>Five-node</b>					
Measured	17.5	18.8	45.5	28.8	30.8
Structure 1	28.7	27.4	76.9	76.9	76.9
Error	-63.7%	-45.6%	-69.1%	-167.2%	-149.7%
Structure 3	20.5	19.6	15.8	15.8	15.8
Error	-17.0%	-3.9%	65.3%	45.1%	48.7%
Structure 7	17.8	17.0	40.6	40.6	40.6
Error	-1.4%	9.8%	10.8%	-41.0%	-31.8%

merical models. The percentage errors between the measured results and the respective numerical models are also provided in this table. The graphs of the measured data from which the compliances were obtained can be found in Appendix B.

For the top and central nodes, a positive value indicates a downward displacement. For the foot nodes it indicates a displacement that is radially outward from the structure's center. A negative error value indicates that the numerical model is less stiff than the physical structure because the numerical model displaces more than the physical structure under a similar load.

From these results the following observations were made:

**Top node errors:** For the top node errors, it is apparent that the numerical model built during the design of the structure is inadequate to accurately predict the displacements of these nodes, as shown by the errors of the "Structure 1" models. Even if the FE models are improved to include more modelling detail, like the "Structure 3" model, the absolute errors are still above 15%. Although this is an improvement over the "Structure 1" results, these results are still poor.

With the addition of the modelling and optimisation techniques that were used to obtain the strut models used for "Structure 7", the numerical model's predictive accuracy shows further improvement. For the five-node structure the absolute error is reduced to under 1.5%, which is a significant improvement. But for the simpler four-node structure the error was still large at 9%, although it was expected that the simpler model would have a smaller error.

**Central-node errors:** Judging by the top node errors of both structures, the first two models are under-stiff. But where the third model for the four-node structure is over-stiff, the third model of the five-node structure is still under-stiff.

A similar inconsistency was found in the errors of the five-node structure's central node displacements. For "Structure 1" and "Structure 3" the numerical model predicted displacements greater than those measured, whereas "Structure 7" predicted a smaller displacement.

Furthermore, inspection of the measured displacements of the top and central nodes of the five-node structure showed that the central node displaces more than the top node, which is contrary to what was predicted by the numerical model.

**Foot node errors:** It was expected that, because of the structure's symmetry and the symmetrical loading, these displacements should be of similar magnitude. The unsymmetrical results for the foot node displacements of the four-node structure is attributed to the fact that the LVDT was placed at different heights on the different foot nodes because of physical constraints in the test setup. This issue was noticed at the time of testing, but since the points at which the LVDTs were placed could be modelled accurately, this did not pose a significant problem and thus different displacement magnitudes were expected.

However, when testing the five-node structure care was taken to place the LVDT at the same height on each foot node, and it thus was expected that these results should be of similar magnitude. As shown by the measured data for the five-node structure, this was not the case because only two foot node displacements had magnitudes that were within 10% of each other, while the third was nearly 50% larger.

At this stage the greatest cause for concern was the fact that the measured data suggested that the central node displaces downward more than the top node. If the central node was to have a greater displacement than the top node, this would imply that the D-strut that connects the two nodes is in tension. For this to happen, the C-struts would have to be pulling the central node downwards.

Figure 6.7a shows the deformed FE model of "Structure 7". From this figure one can see that the outward rotations of the foot nodes cause severe deflections of the struts. However, if the foot nodes were to rotate to the inside of the structure, as opposed to the current situation where they are rotating to the outside, it might be possible that the induced moments would result in the C-struts deflecting in such a manner that they could pull the central node downwards. Such a moment would be as a result of the point where each foot node is supported, and consequently rotates, being in a different position than originally assumed. The first assumption which was suspected to be incorrect, was that the foot nodes did not rotate around the top of the steel bearing balls, but rather that the rotation happened at the point where the ball contacts the 100 mm steel plate.

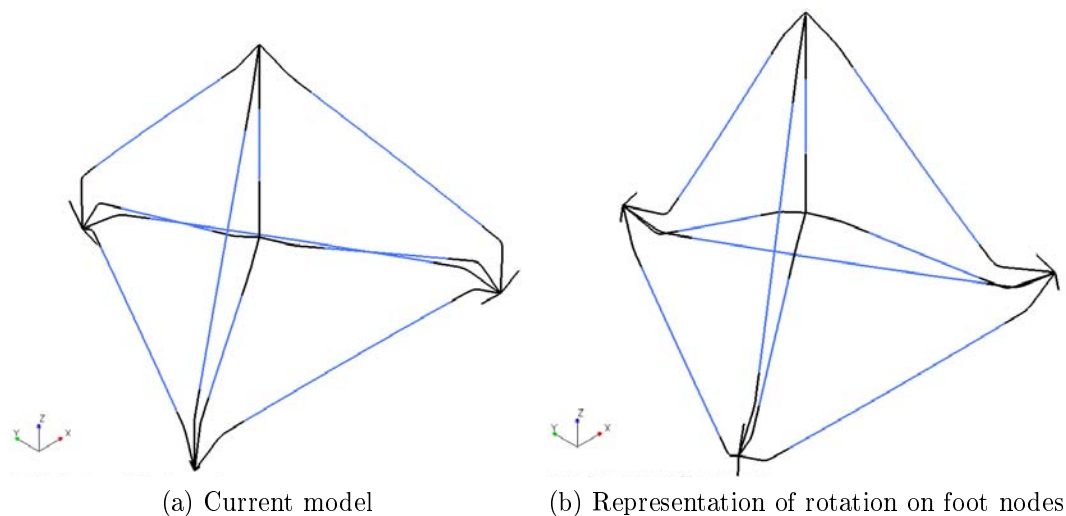


Figure 6.7: FE models of deformed five-node structure

This change in the boundary conditions was made to the model, but the results remained relatively unchanged. This numerical model still contradicted the test data because the top node still displaced almost  $1 \mu\text{m}/\text{kN}$  more than the central node. As a further test, a numerical model was built where moments were applied directly to the foot nodes that would result in them rotating inwards to the centre of the structure, as shown in Figure 6.7b. It was eventually found that no degree of foot node rotation would result in the central node displacing more than the top node. This was because of the geometry of the structure, since if the foot node is rotated, the B-struts experience a greater loading to pull the top node downwards than the C-struts, and therefore the top node will always displace more than the central node.

Further investigation suggested that, if the foot node displacements were taken into account as well, it could be possible that the physical structure was undergoing unsymmetrical deformation. An example of such a deformation is shown in Figure 6.8. The figure shows the side view of such a state and, if it is compared to the dashed line of symmetry next to the D-strut, one can see that there is both lateral movement of the central node, and rotation. If this is the case, it is possible that the centre node will undergo certain rotations because some foot nodes displace more than others, whilst the top node remains stationary, thus causing an internal moment. Such rotations on the central node would imply that both translational and rotational effects were being measured. Because the central node's point of rotation is unknown, it is impossible to compensate for the rotational effects in order to isolate the translational effects. This would imply that the measurements taken on the central node are misleading and therefore they cannot be used as validation criteria.

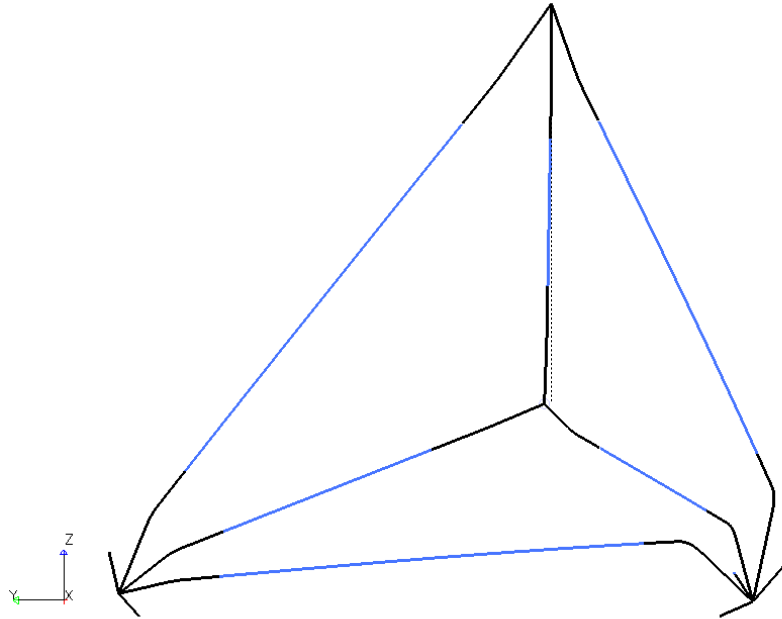


Figure 6.8: FE representation of unsymmetrical deformation

To try to determine the severity of the unsymmetrical deformation required to result in the measured foot node displacements, it was decided to treat the problem theoretically by assuming that the triangle consisting of the three foot nodes undergoes rigid body movements. Although this is not necessarily the case, this assumption was used as an approximation only. Because there were three parameters, two displacements and one rotation, that would have an

effect on the three effective measured foot node displacements, it was decided to formulate this into an optimisation problem.

The objective of this problem was to apply the three rigid body movement parameters to the numerical results of the foot node displacements so that they would match the measured foot node displacements. Because the measurements were taken in different coordinate systems to that in which the rigid body movements would occur, as shown in Figure 6.9, it first was necessary to formulate functions that describe the effects these movements would have in the measured coordinate systems. The details of how these functions were formulated can be found in Appendix C.

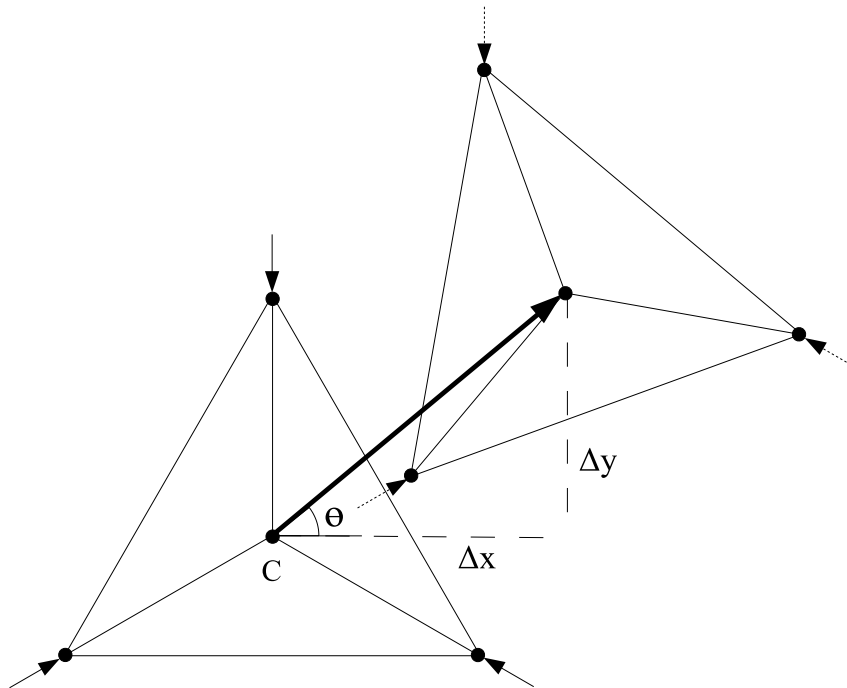


Figure 6.9: Rigid body mode compensation parameters and LVDT measurement directions (top view).

With these functions explicitly defined, an objective function was defined by using the same principles of compromise programming that were used during the individual strut modelling to combine and scale the three displacements objectives:

$$G = \sum_{n=1}^3 \left( \frac{(\Delta M_n)_R - (\Delta M_n)_T}{(\Delta M_n)_M - (\Delta M_n)_T} \right)^2 \quad (6.3.1)$$

Here,  $\Delta M_n$  is the displacement in the measurement coordinate system of foot node  $n$ . Subscript  $T$  denotes the target values, subscript  $M$  denotes

Table 6.2: Rigid body movement parameters

Parameters	Four Node			Five Node		
	$\Delta x$ [ $\mu m$ ]	$\Delta y$ [ $\mu m$ ]	$\Delta \theta$ [radians]	$\Delta x$ [ $\mu m$ ]	$\Delta y$ [ $\mu m$ ]	$\Delta \theta$ [radians]
Model 1	15.4	55.8	$10.8 \times 10^{-3}$	-8.5	57.9	$5.8 \times 10^{-3}$
Model 3	14.9	26.4	$8.7 \times 10^{-3}$	-8.4	-23.5	$-6.0 \times 10^{-3}$
Model 9	14.4	-0.497	$6.3 \times 10^{-3}$	-8.5	9.5	$-2.8 \times 10^{-3}$

the initial FE model values and subscript  $R$  denotes the current response values. The current response values are calculated with the functions defined in Appendix C.

Shown in Table 6.2 are the results of the rigid body movement compensation analysis. With these values, the errors of the foot node displacements were reduced to below  $1 \mu m$ . These results showed that the measured displacement errors of all the foot nodes can be accounted for, if such rigid body movements should occur. Also, the magnitude of these rigid body movements was small enough so that it was deemed possible that they could have happened during testing. Note again that these movements are only an approximation and can therefore not be applied directly to the results, although they provide an indication of the scale of the possible unsymmetrical deformation.

With the results of the central and foot nodes accounted for, the only remaining issue was that the simpler four-node model is less accurate than the more complex five-node model. If, however, one takes into consideration that there is evidence to suggest that the structure is undergoing unsymmetrical deformation, it must be assumed that the measured displacements of the top node will also include some degree of error. Although the four-node model has an error of 9.0%, this error equals to roughly  $2 \mu m/kN$ . Since the maximum load applied to the structure was roughly 10kN, this results in a mere  $20 \mu m$  error in total. Given the size of the structure and the aforementioned suspected deformations, it must be assumed that a measurement error of the size could be expected.

## 6.4 Validation Conclusion

Given all the aforementioned theories, the final validation results can be justified. Although these findings cannot be proven explicitly unless further testing with higher accuracy is done, there is evidence to suggest that the structure deforms unsymmetrically. But one of the most important realisations is that the method of obtaining the structure's responses is insufficient. Although the

equipment used has high enough resolution, the test setup is not sufficient to accurately capture the structure's behaviour unless it is perfectly symmetrical. Even if the structure was to deform symmetrically, it was realised that, because of the scale of the measurements, it would be very difficult to obtain measurements that were completely isolated from external or unforeseen effects. Had the scale of displacements been larger, the results would possibly have been less sensitive to the suspected errors, such as misalignment, tolerances in the connections, geometrical tolerances and material deformation in the nodes. Despite these suspected problems, there is enough confidence in the measured displacements of the top node to use these as validation criteria.



# Chapter 7

## Conclusion

Because SALT mirror support truss is currently deforming unsymmetrically, a proposed solution to implement a control system to compensate for this requires a high-accuracy numerical model of the truss. The objective of this project was to undertake a study of how such a model of an existing structure, based on the mirror support truss, could be obtained.

### 7.1 Overview

The study was done by designing and building a smaller, simpler laboratory model with features similar to the building blocks of the support truss on which testing could be done. To obtain a high-accuracy numerical model of a specific structure, measurements of this structure's responses were made so that the predicted responses of the numerical model could match these measurements.

The literature survey revealed that this process of data matching is an inverse problem, and if care is not taken, the task can be difficult and the results could be misleading. In setting up such a problem, suitable parameter selection and objective formulation must be complemented by a compatible transformation process for the specific problem at hand so that the solution converges to a single, acceptable result. Numerical design optimisation methods were used for the transformation process in this project and the parameter selection was made so that if changes were made to these parameters, their physical significance would be retained.

Due to the accuracy required and the complexity of the structure, a step-by-step methodology for this project was developed using suggestions from the literature. The proposed method was to start by examining the individual struts with which the laboratory model was built. The methodology developed suggested that the physical testing and numerical modelling steps of each phase should be done in parallel. One of the most important outcomes of this is that problems in the test data could be identified earlier when attempting to impose the measured data on the numerical design optimisation models.

Tests were performed on each of the struts in order to obtain a set of data of both static and dynamic responses. From the static load tests it was found that, because of the scale of the displacements measured, external effects such as deflections of the test setup load frame should be considered carefully. The best results were obtained by attempting to isolate external effects by choosing measuring datums on the test specimen itself, and not on the load frame.

The data-matching exercise performed on the struts yielded models for each strut type. The final modelling setup included sizing and shape-change design variables, and in certain regions elements were put in parallel to provide the optimiser with enough freedom to compensate for the uncertain behaviour of these regions. The maximum error of all the responses for all four strut types was reduced from over 20% to below 5%, and the average error for all the final models was reduced to below 1.3%. On the success of these modelling improvements, the validation of the methods could continue.

Validation was done by using these strut models to build numerical models of the laboratory test structure. This was accompanied by obtaining responses from the laboratory test structure. During testing it was realised that the measured results were extremely sensitive to the boundary conditions applied to the structure. Multiple attempts were made on the application of both the supporting and loading boundary condition setups before a combination was found that yielded acceptable results from which a linear fit could be made. Upon comparing these results with those of the numerical models, certain inconsistencies were found that could not be explained or compensated for by trying to improve the numerical models. Further theories were developed to explain each of the individual inconsistencies, and the combination of these theories led to the conclusion that the test structure undergoes deformations that cannot accurately be captured by the test setup and the available resources. For better results, a completely different method of testing the structure, and even a redesign of the structure itself, would be necessary.

However, concerning the displacements of the most important point of the structure, the top node, the methodology and techniques used in this project yielded numerical models of the laboratory structure that were significantly more accurate than the techniques used in the FE model built during the development of the mirror support truss. The absolute error in predicting the top node displacement for the more complex, five-node laboratory structure was reduced from over 60% to below 1.5%. For the four-node structure the final error was still large at, 9%, but it is an improvement on the initial error of almost 50%.

These results confirm that better numerical models of the struts can be obtained by using numerical design optimisation. Furthermore, the results also show that if these strut models are improved, the accuracy of the numerical model of the assembled structure is improved, without explicitly performing optimisation on the assembled model.

Therefore, if a high-accuracy numerical model of the mirror support truss

of SALT is to be obtained, the findings of this project propose that an accurate numerical model of each strut type should be obtained first before the structure as a whole is considered. This method has the advantages that many modelling uncertainties about the building blocks of the structure can be eliminated before the complications associated with the behaviour of the structure are addressed. This project also shows that the use of numerical design optimisation methods provides effective tools for obtaining better models and for locating modelling errors or shortcomings.

## 7.2 Future Work

The biggest obstacle that was faced during the course of this project was to obtain accurate measurements of the responses of the assembled structure. Although the equipment available was sensitive enough for the magnitude of the displacements that were measured, the scale in which these displacements occurred made it difficult to isolate them from external effects. These effects are the results of unforeseen deformation of the structure due to difficulties such as the exact placement of the supporting and loading boundary conditions, tolerances in the construction of the structure, the behaviour of the threaded connections and the deformation of the solid steel nodes. These effects are likely to induce displacement errors as small as  $1 \mu m$ . Given the size of the structure, these small displacement errors seem insignificant. But, in the case of the displacements of the top and central nodes of the five-node structure, a  $1 \mu m$  error is enough to translate to severe errors. It is therefore advised that future testing should include a means to capture the rotations of the nodes, as well as the relative displacements between the nodes. If the rotations and relative displacements are known, a better approximation can be made of the behaviour of the structure during testing. If the actual behaviour of the structure is known, better points of measurement can be selected so that there is more certainty about exactly what types of translations and rotations are being measured. For the modelling of the structure, it is suggested that the connection of the struts to the nodes be further investigated. As with the end caps of the struts, the threaded rods screw into the nodes and this could also be a source of modelling inaccuracy. A suggestion would be to model these connections using springs and then to tune the stiffness of these springs. This would require performing additional model updating to be done on the assembled structure since it would not be possible to do this on single strut level only. To validate these results it is further suggested that a bigger, more complex structure with for example 10-15 nodes to be investigated.

# Appendices

## Appendix A

# Modelling Data of Individual Struts

### A.1 Response Data of the A-Strut

Table A.1: Summary of the responses of the various models of the A-strut

Objective function	Bend over:			Frequency number:			
	Axial [ $\mu m/kN$ ]	Rods [ $\mu m/kN$ ]	Hollow bar [ $\mu m/kN$ ]	End caps [ $\mu m/kN$ ]	One [Hz]	Two [Hz]	Three [Hz]
<b>Target</b>	-	627	163	349	290.9	530.9	701.6
Model1	-	759.4	195.1	418.2	310.5	561	679.3
Model2	-	718.1	195.1	419.7	322.3	620.8	773.4
Model3	-	693.1	195.1	417.8	286.1	636.2	778.6
Model4	$1.323 \times 10^{-3}$	630.4	162.1	348.0	289.5	544.7	688.3
Model5	$3.32 \times 10^{-4}$	624.2	162.9	349.8	291.8	532.0	710.4
Model6	$1.025 \times 10^{-3}$	630.0	163.3	350.2	299.8	529.4	704.0
Model7	$8.34 \times 10^{-8}$	625.0	162.9	349.2	288.6	531.9	699.3

## **A.2 Responses of All Final Strut Models**

Table A.2: Summary of the all the responses from all the strut types

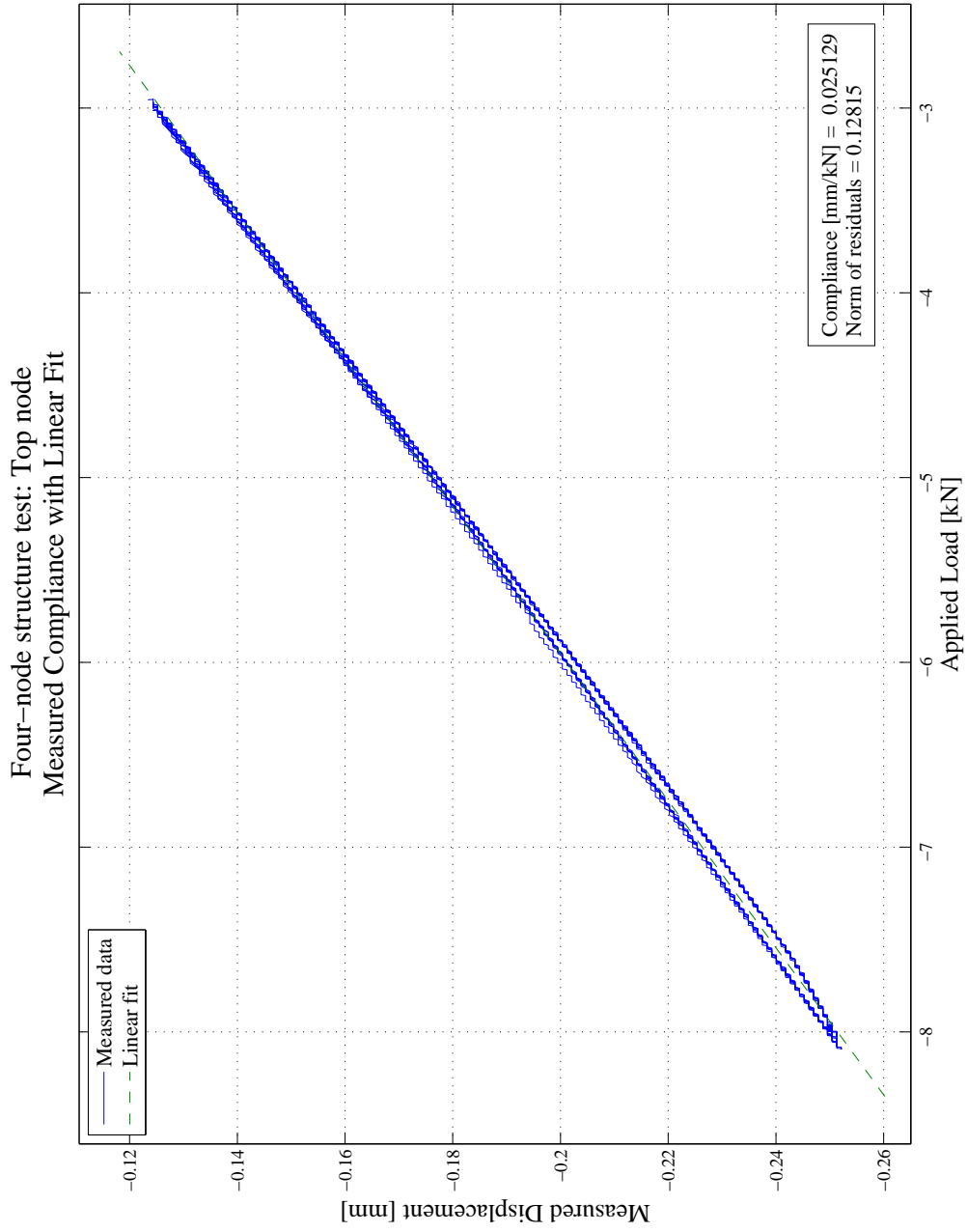
	Bend over:			Frequency number:			
	Axial	Rods	Hollow bar	End caps	One	Two	Three
<b>Target</b>	9.83	627.0	163.0	349.0	290.9	530.9	701.6
AModel3	9.98	693.2	195.1	417.9	285.4	644.2	778.8
AModel7	9.84	625.0	163.0	349.2	288.7	531.9	699.4
<b>Target</b>	8.77	517.0	122.0	282.0	328.9	697.8	848.3
BModel3	9.62	580.9	145.4	333.2	324.8	667.2	804.9
BModel7	8.60	498.9	125.3	287.1	329.0	699.5	838.0
<b>Target</b>	7.94	173.5	-	46.5	640.1	714.8	1123.4
CModel3	7.56	183.4	-	56.2	644.2	798.0	1130.9
CModel7	7.89	177.2	-	45.9	637.6	740.0	1114.9
<b>Target</b>	6.79	141.5	-	21.0	720.9	851.9	1812.4
DModel3	6.88	123.4	-	22.1	684.9	840.3	1795.0
DModel7	6.81	137.9	-	21.2	721.0	809.9	1830.0

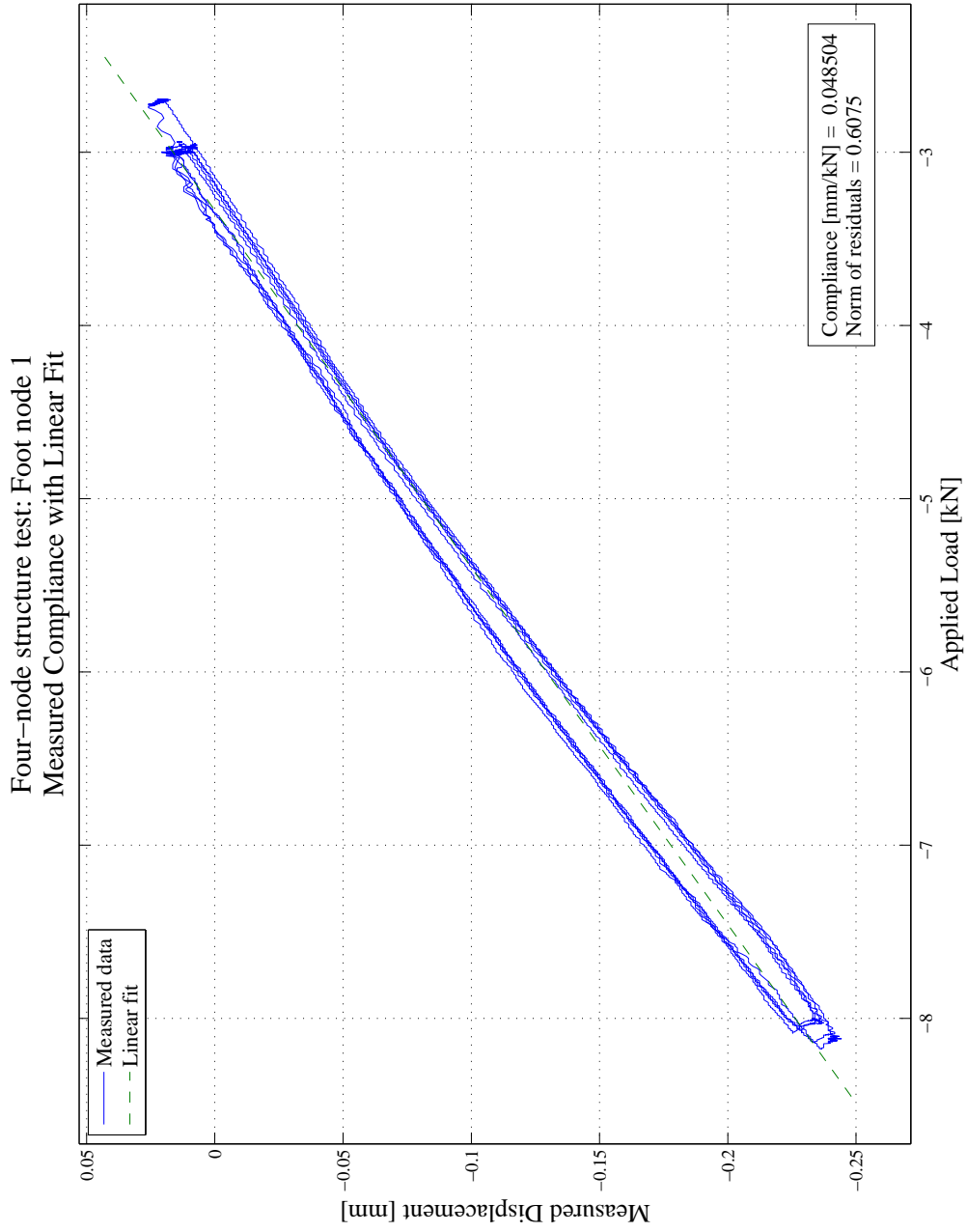


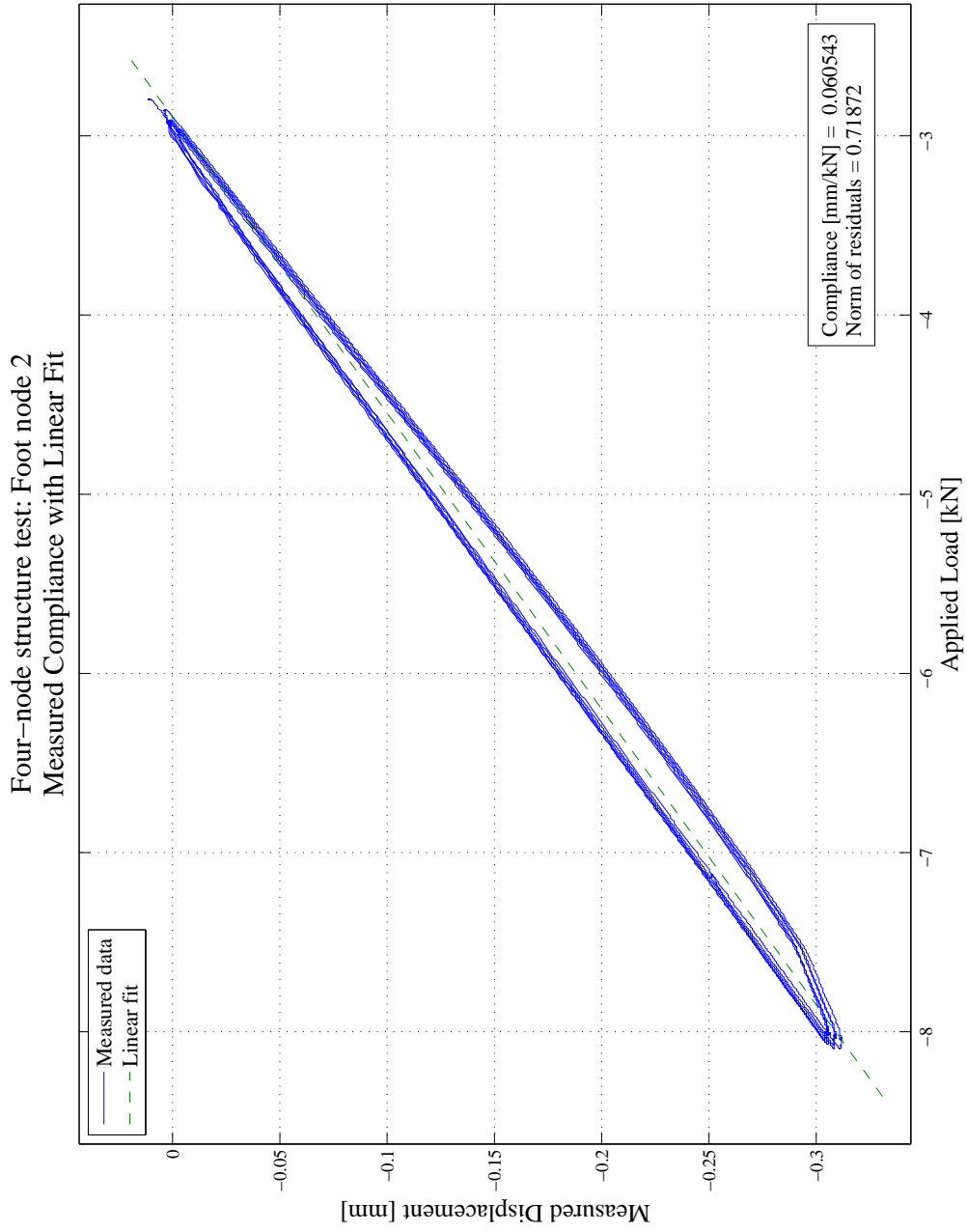
## Appendix B

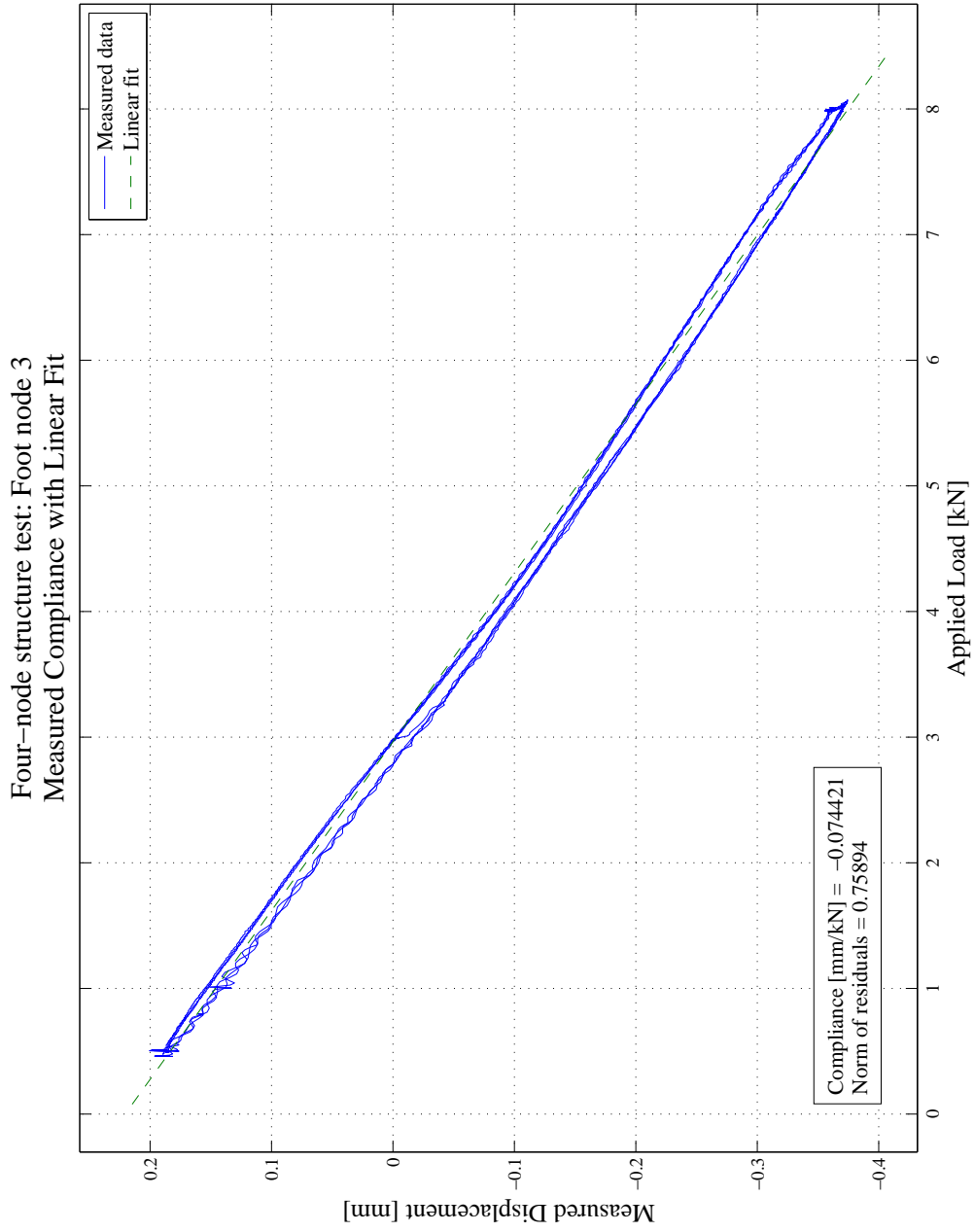
### Test Data of Final Structure

#### B.1 Data of Four-node Structure

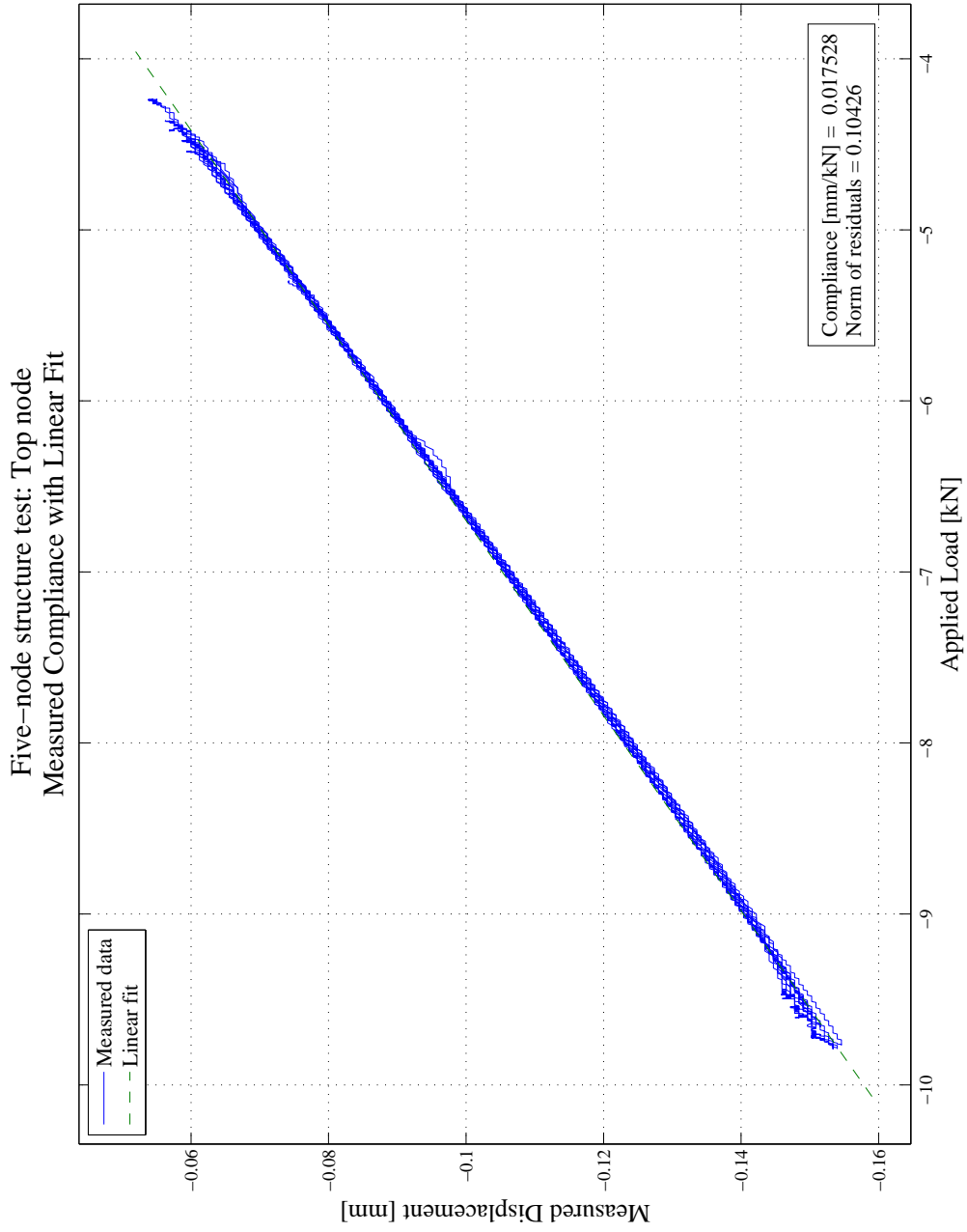


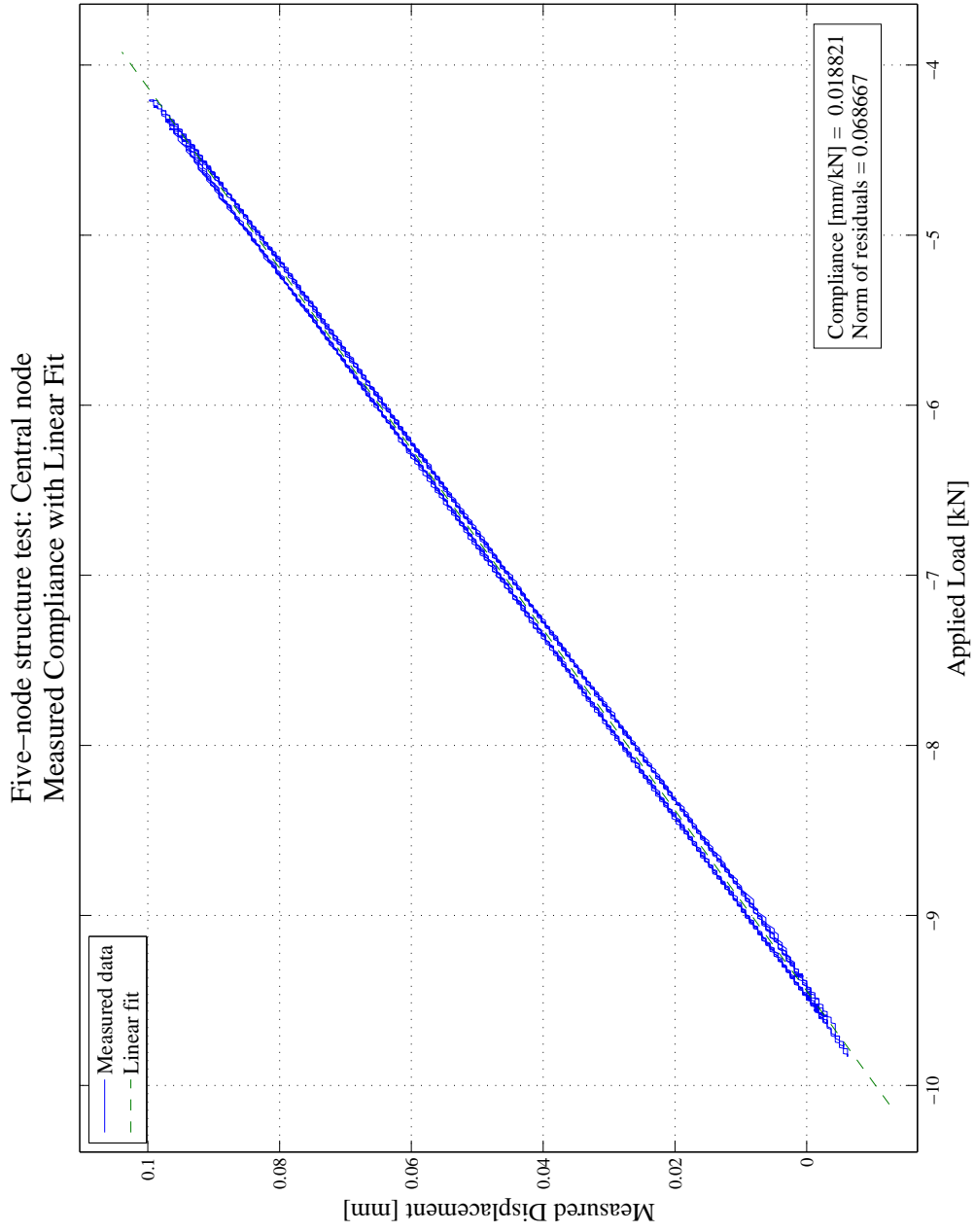




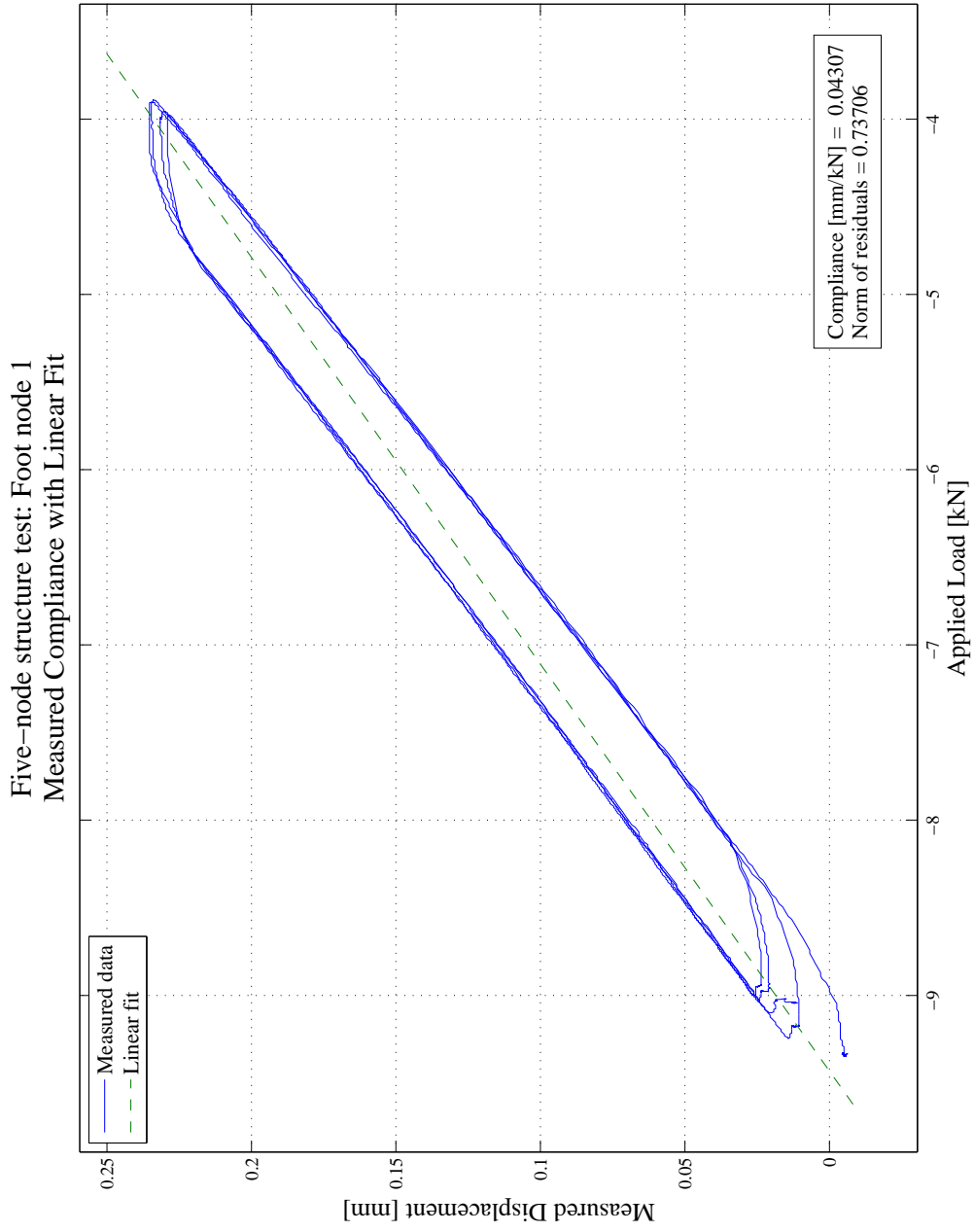


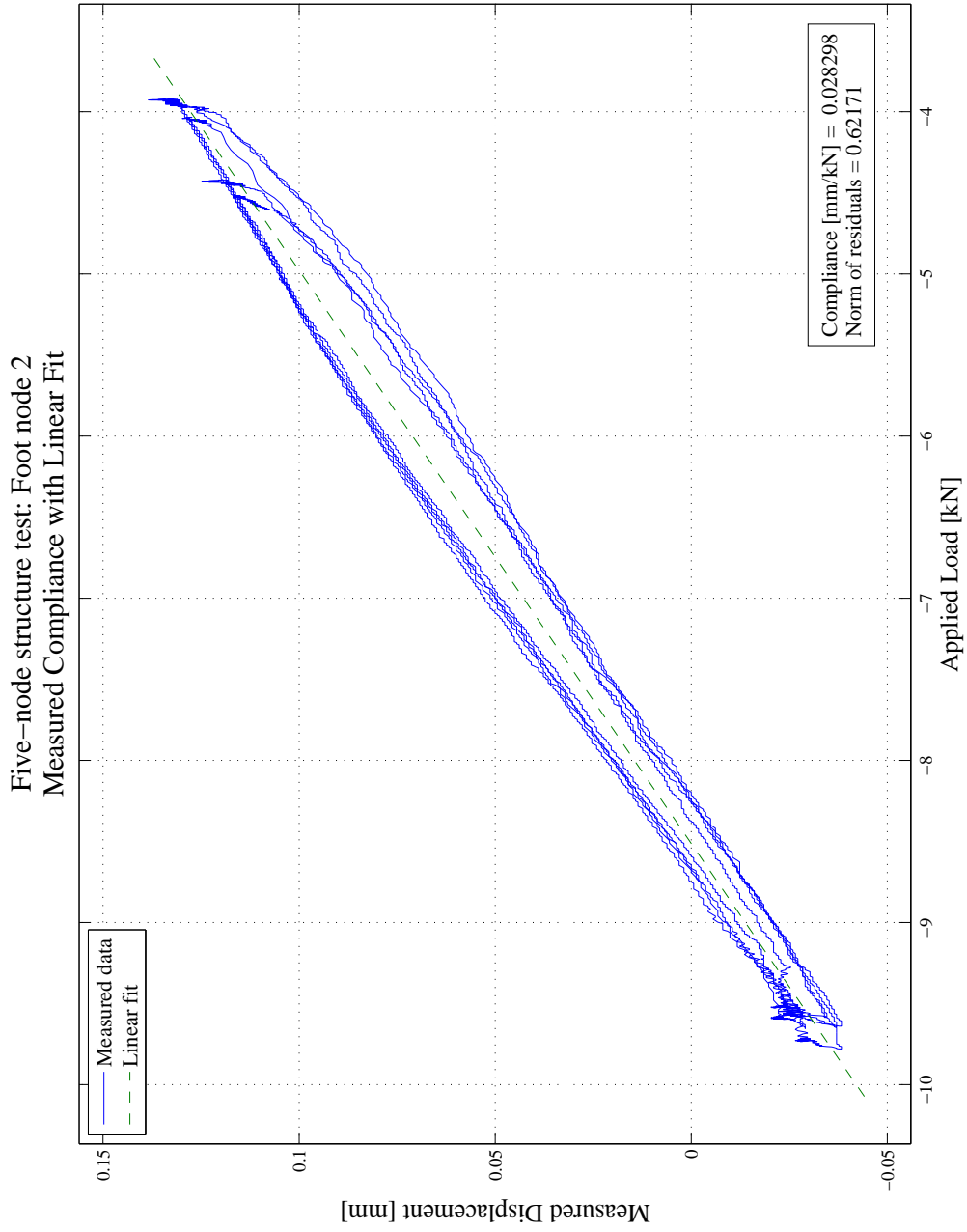
## **B.2 Data of Five-node Structure**



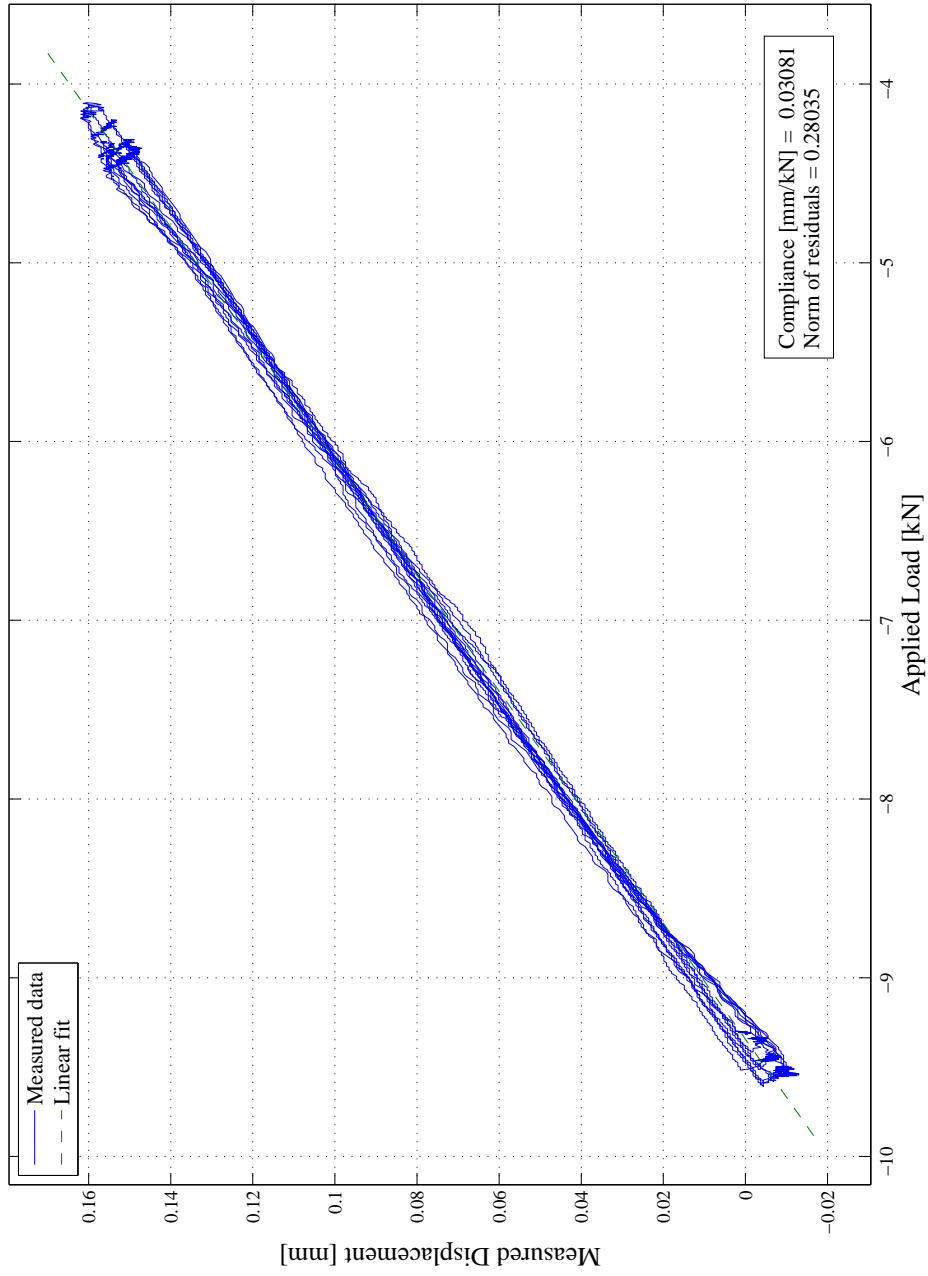








Five-node structure test: Foot node 3  
Measured Compliance with Linear Fit



## Appendix C

# Rigid Body Mode Compensation Formulation

Because the LVDT remains stationary during loading, the change in the compensation parameters had to be translated to what the LVDT would effectively measure at each foot node. This was done by first breaking the contributing effects into two parts: the effects due to the rotation and to translation of the structure. By first translating the rotational effects to x- and y-displacements at each node, the x- and y-translations of the structure could be added to these and the total x- and y-displacements at each node are then defined by the equations below:

$$\Delta x_n = \Delta x_{rn} + \Delta x \quad (\text{C.0.1})$$

$$\Delta y_n = \Delta y_{rn} + \Delta y \quad (\text{C.0.2})$$

Here,  $\Delta \mathbf{x}_n$  is the total x-displacement of node  $n$ ,  $\Delta \mathbf{x}_{rn}$  is the x-displacement due to rotation, and  $\Delta \mathbf{x}$  is the x-displacement of the entire structure. This is the same for the y-displacements. Note that  $\Delta \mathbf{x}$  and  $\Delta \mathbf{y}$  are two of the three compensation parameters that can be changed by the optimiser.

Once the x- and y-displacements at each node are known, the displacement in the fixed direction of measurement of the LVDT at each node could be calculated. To obtain these displacements it was necessary to do certain transformations by using simple geometry. The transformation of changing the rotation of the structure to x- and y-displacements will be explained first. This will be followed by a discussion of the transformation of the total displacements at the foot nodes as would be measured by the LVDT.

### C.1 Global Coordinate System Translations

The geometry in Figure C.1 is used for the displacements due to rotation . This figure is the simplified geometry of the translation of a point on a foot

node as the structure rotates around its centre. The centre of the structure is point  $C$  in the figure, and the original position and the new position of the foot node are designated by points  $FN$  and  $FN'$  respectively.

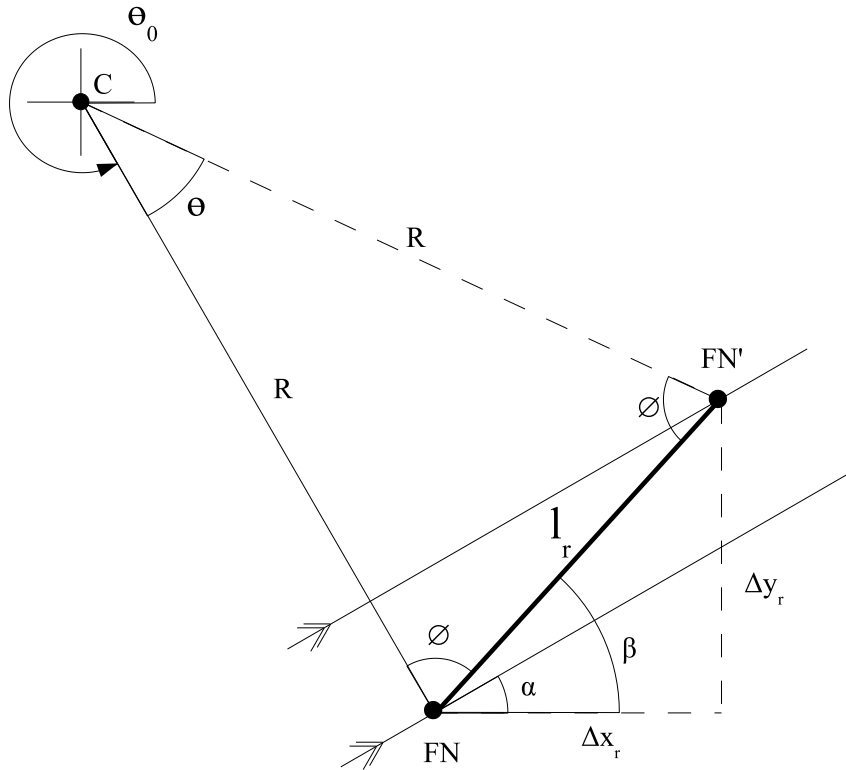


Figure C.1: Geometry for calculation of rotational effects

The other parameters in the figure are defined as listed here:

- $R$  Radius from the rotational center of the structure to the foot nodes
- $\theta$  Angle of rotation of the structure (compensation parameter)
- $\theta_0$  Angle from x-axis to foot node
- $\alpha$  Angle from x-axis to line perpendicular to the axial direction of the LVDT
- $l_r$  Total displacement due to rotation
- $\beta$  Angle from x-axis to  $l_r$  vector
- $\Delta x_r$  x-displacement due to rotation
- $\Delta y_r$  y-displacement due to rotation

The length of the displacement is calculated using the rule of cosines on the triangle made up by the initial radius line (solid line), the rotated radius line (dashed line) and the angle of rotation  $\theta$ :

$$l_r^2 = R^2 + R^2 - 2RR\cos(\theta)$$

Since both radius lines are equal, this reduces to

$$l_r = \sqrt{2R^2(1 - \cos(\theta))} \quad (\text{C.1.1})$$

The x- and y-displacements are then calculated as

$$\begin{aligned} \Delta x_{rn} &= l_r \cos(\beta) \\ \Delta y_{rn} &= l_r \sin(\beta) \end{aligned}$$

with

$$\beta = \alpha + (90^\circ - \phi) \quad (\text{C.1.2})$$

Remembering that  $\alpha$  is the angle between the x-axis and the line perpendicular to the original radial line  $\mathbf{R}$ ,  $\alpha$  is calculated as

$$\begin{aligned} \alpha &= 90^\circ - (-\theta_0) \\ &= 90^\circ + \theta_0 \end{aligned}$$

The angles marked by  $\phi$  are equal because the triangle is an isosceles triangle. They can be expressed in terms of the structure's angle of rotation  $\theta$ :

$$\begin{aligned} \phi &= \frac{180^\circ - \theta}{2} \\ &= 90^\circ - \frac{\theta}{2} \end{aligned}$$

This allows  $\beta$  in equation (C.1.2) to be expressed as

$$\beta = \alpha + \frac{\theta}{2}$$

## C.2 Local Coordinate System Translations

With the total displacements at each foot node now available, these displacements can be transformed to the direction of measurement of the LVDT. The geometry in Figure C.2 is used for this transformation. This figure is similar to the previous one, but for clarity only the geometry involved in this transformation is shown. It is important to note that translation between the points

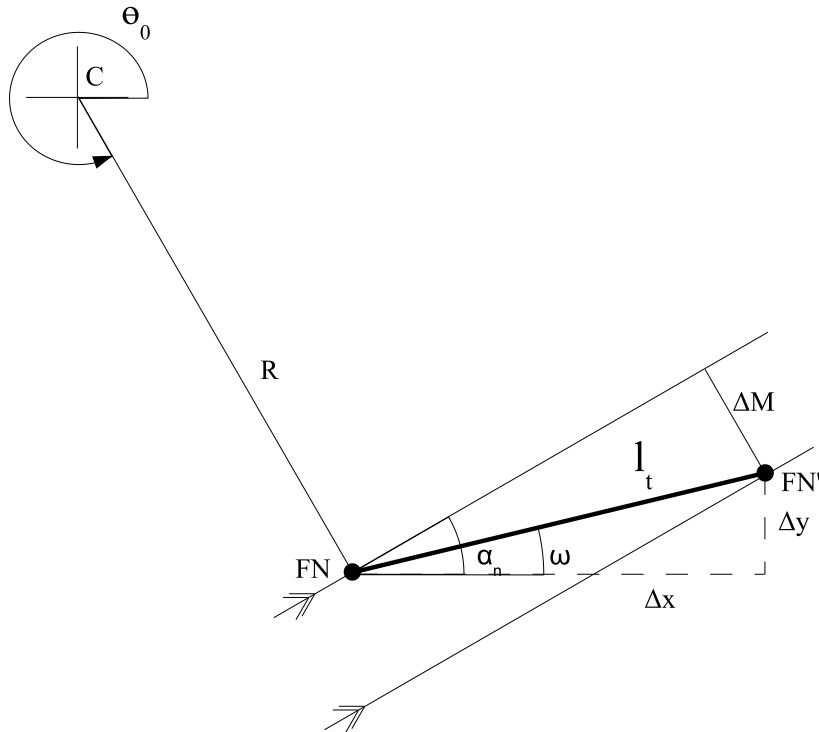


Figure C.2: Geometry for transformation to direction of measurement of the LVDT

$\mathbf{FN}$  and  $\mathbf{FN}'$  is the sum of both the rigid body translations as well as the translations due to the rigid body rotation. It is also important to remember that the direction of measurement of the LVDT remains unchanged, and therefore the measured translation is the distance between the parallel lines perpendicular to the radial line  $\mathbf{R}$ .

Here,  $\Delta x_n$  and  $\Delta y_n$  are the total displacements as described in equations (C.0.1) and (C.0.2) respectively. From these displacements, the total length of displacement  $l_t$  and the angle  $\omega$  between the x-axis and the total displacement vector can be determined. Finally, the displacement in the direction of measurement of the LVDT is then calculated as:

$$\Delta M = l_t \sin(\alpha - \omega) \quad (\text{C.2.1})$$

## List of References

- Buckley, D., Lombard, M., Lomborg, M., Meiring, K. and Theron, R. (2005). *Africa's Giant Eye : Building the Southern African Large Telescope*. The SALT Foundation (Pty) Ltd.
- Chen, T.Y. and Wang, B.P. (1991). An exploration of structural refinement using structural matrices of local elements as design variables. *Computers & Structures*, vol. 39, no. 6, pp. 705–713.
- Forbes, G. (2008). *History of Astronomy*. Plain Label Books.
- GENESIS (2008 December). *Genesis Design Manual Version 10.1*. Vanderplaats Research & Development, Inc., Colorado Springs.
- Howell, D.J. (2004). *Multi-Configuration Model Tuning for Precision Opto-Mechanical Systems*. Master's thesis, Departement of Aeronautics and Astronautics, Massachusetts Institute of Technology.
- Kanev, S., Weber, F. and Verhaegen, M. (2007). Experimental validation of a finite-element model updating procedure. *Journal of Sound and Vibration*, vol. 300, no. 1-2, pp. 394 – 413. ISSN 0022-460X.
- Kim, G.-H. and Park, Y.-S. (2004). An improved updating parameter selection method and finite element model update using multiobjective optimisation technique. *Mechanical Systems and Signal Processing*, vol. 18, no. 1, pp. 59 – 78. ISSN 0888-3270.
- Kozak, M.T., Öztürk, M. and Özgüven, H.N. (2009). A method in model updating using miscorrelation index sensitivity. *Mechanical Systems and Signal Processing*, vol. 23, no. 6, pp. 1747 – 1758. ISSN 0888-3270.
- Leiva, J.P. and Watson, B.C. (1999). Shape optimization in the genesis program. *Optimization in Industry*, vol. 2.
- Lung, S. and Pak, C. (2008 Oktober). Structural model tuning capability in an object-orientated multidisciplinary design, analysis and optimization tool. Tech. Rep. NASA/TM-2008-214640, National Aeronautics and Space Administration.
- Marler, R.T. and Arora, J.S. (2004). Survey of multi-objective optimization methods for engineering. *Structural and Multidiscipline Optimization*, vol. 26, pp. 369–395.



- MathWorks (2011). Optimisation Toolbox Product Overview. [Online].  
Available at: <http://www.mathworks.com/products/optimization/description1.html> [2011, February 25]
- Maxwell, J.C. (1864). On the calculation of the equilibrium and stiffness of frames. *Philosophy Magazine*, vol. 27, p. 294.
- Mottershead, J.E., Link, M. and Friswell, M.I. (2010). The sensitivity method in finite element model updating: A tutorial. *Mechanical Systems and Signal Processing*, vol. (In Press, Corrected Proof). ISSN 0888-3270.
- Mottershead, J.E., Mares, C., Friswell, M.I. and James, S. (2000). Selection and updating of parameters for an aluminium space-frame model. *Mechanical Systems and Signal Processing*, vol. 14, no. 6, pp. 923 – 944. ISSN 0888-3270.
- Ratcliffe, H. (2011). Wanderer at the Frontier. [Online].  
Available at: <http://www.hiltonratcliffe.com/pictures.htm> [2011, May 10]
- Rutgers (2011). Southern African Large Telescope (SALT). [Online].  
Available at: <http://www.physics.rutgers.edu/ast/ast-salt.html> [2011, February 28]
- SAISC (2005). *Southern African Steel Costruction Handbook*. 5th edn. Compiled and Published by Southern African Institute of Steel Construction.
- SALT Foundation (2011). Southern African Large Telescope. [Online].  
Available at: <http://www.salt.ac.za/public-info/picture-gallery/salt-images/primary-mirror-images/> [2011, February 10]
- Shan, P.S., Kawaguchi, M. and Abe, M. (1994). An application of inverse problem techniques to spatial structures. In: *Spatial, Lattice and Tension Structures*, pp. 113–122.
- Vanderplaats, G.N. (2007). *Multidiscipline Design Optimization*. Vanderplaats Research & Development, Inc.
- Ziaei-Rad, S. and Imregun, M. (1996). On the accuracy required of experimental data for finite element model updating. *Journal of Sound and Vibration*, vol. 196, no. 3, pp. 323 – 336. ISSN 0022-460X.